POLITECNICO DI TORINO

Master of science in Electrical Engineering

MASTER'S DEGREE THESIS

ELECTROMAGNETIC DESIGN AND FEM ANALYSIS OF PERMANENT MAGNET MACHINES FOR HIGH SPEED APPLICATIONS

Supervisors:

Ing. Silvio Vaschetto

Prof. Andrea Cavagnino

Candidate:

Iannella Carmen

A.Y. 2019/2020

Contents

Abstract

This thesis has been performed thanks to work project collaboration between Politecnico di Torino (Turin, Italy) and Agilent.

Calculations are done in FLUX. The thesis can be divided in different topics.

In the first chapter, focus is on different application of high-speed machine, advantages and problems.

At the chapter 2, it is presented the reverse engineering of an existing machine for FEM model calculation. First is introduced the Surface Permanent Magnet motor, are reported the materials and the input date. After it is presented a sizing procedure for the design of high-speed machine. In the second part of the chapter, is presented the model implemented on FLUX, the definition of the Br for the calibration of the E0 at the test temperature. Then, there is the evaluation of the cogging torque in no load-conditions and computation of the electromagnetic torque and the comparison with the available data. After there is the computation of the synchronous inductance and the comparison with the results obtained by the measurements on the motor. At the end of the chapter, all the measurements are reported.

Chapter 3 is reserved to the iron loss computation. At the start of the chapter there is a small introduction about the different methods to compute the iron losses. Then, there is the investigation of the losses in the stator, in the sleeve and in the permanent magnets with sinusoidal supply at the rated speed in no load and load conditions. For the iron computation in FLUX are used two different methods: Bertotti and Loss Surface.

In the chapter 4 is presented a new motor design. Using an existing stator of an induction motor, a new rotor is adapted, modifying its airgap diameter and then changing the material of the magnets (from NdFe to ferrite) and the thickness of the permanent magnets to obtain the same performance of the start motor. Then, it is studied the existing machine but with slotless execution.

Conclusion and future works resulting from this study are discussed in chapter 5.

List of Figure

List of Tables

Nomenclature

α Half pole in electrical degrees

α Thermal coefficient of the copper at 20°C

α_1 Exponent of the classical losses

α_2 Exponent of the eddy current losses

α_3 Exponent of the excess losses

α_i ratio between the average flux density and the peak value of the flux density

α_m Thermal conductivity of the NdFe magnets

α_{pm} Magnet circumferential coverage

δ Shrinkage

δ_0 Effective airgap met by the current linkage

ϑ_s Linkage current

λ Aspect ratio

λ_u Permeance factor

μ_0 Vacuum magnetic permeability

μ_r Relative permeability

υ Poisson's coefficient

ρ Resistivity

p_{Fe} Iron losses

σ Mechanical stress of the material

σ Electrical conductivity

τ_w Winding pitch

τ_p Polar pitch

τ_{sb} Bottom slot pitch

ω_{cr} Critical speed

ϕ_p Magnetic flux per pole

ϕ_{p_fund} Magnetic fundamental flux per pole

ψ_m Flux of a single phase

A Cross section of the shaft, Linear current density

a Number of parallel paths

a Steinmetz coefficient

a_{ts} Total slot area

a_{Cu} Conductive material area in the stator slots

a_{us} Useful area

a_{ts} Total slot area

$B_{@20}$ Residual induction at 20°C

B_d Value of the d component of the magnetic flux density

$B_{fundamental}$ Fundamental magnetic flux density

B_{gap} Maximum value of the airgap flux density

B_m Magnetic flux density in the airgap

B_q Value of the q component of the magnetic flux density

B_r Magnet residual flux density

b Steinmetz coefficient

b_{gap_fund} Fundamental airgap flux density

b_{yr} Effective rotor yoke flux density

C_{exc} Excess loss factor

c_n Viscous equivalent of the rotor external damping

c_r Viscous equivalent of the rotor internal dumping

D_a Average diameter

D_{er} External rotor diameter

D_{gap} Diameter at the middle of the airgap

D_{ir} Internal rotor diameter

D_{is} Stator inner diameter

D_{pm} Diameter of the external surface of the permanent magnets

d_{min} Inner diameter imposed by the designer

d_{wire} Diameter of the wire

E Young's modulus

EMF Electromotive force

FEM Finite Element Modelling

FFT Fast Fourier Analysis

f Frequency

G Dimensionless coefficient of the eddy current dumping

h'_{pm} Real airgap length

h_{gap} Airgap thickness

h_{pm} Permanent magnet thickness

h_{ys} Stator yoke thickness

h_{us} Slot useful height

h_{tooth} Tooth height

h_{ts} Slot height

I_d Value of the d component of the current

I_q Value of the q component of the current

I_y Surface moment of inertia

I_{slot} Slot current

$i_{a,b,c}$ Instantaneous values of the currents in the three phases

$i_{\alpha,\beta}$ Instantaneous values of the current in the α,β frame

$i_{d,q}$ Instantaneous values of the current in the d,q frame

$k*$ Non dimensional stifness

k_1 Hysteresis losses coefficient

k_2 Eddy current losses coefficient

k_3 Coefficient of losses in excess

k Stifness of the bearings

k Steinmetz coefficient

k_{avv} Fundamental harmonic winding factor

k_{Carter} Carter coefficient

k_{fe} Stacking factor

k_{fill} Fill Factor

k_{header} Coefficient of the header

k_{skew} Skew factor

$k_{w,1}$ Fundamental winding factor

L Active length of the machine

L_{at} Axial length

$L_{average}$ Average length of the wire

L_d Inductance in the d axis

L_{eq} Equivalent inductance

L_{header} Length of the header

$L_{leakage}$ Leakage inductance

L_m Magnetization inductance

L_p Equivalent length

L_q Inductance in the q axis

L_s Synchronous inductance

L_u Leakage slot inductance

$L_{leakage}$ Leakage inductance

l Shaft length

m Number of phases

N Number of turns

P Active power

P Power loss

PF Power Factor

PMs Permanent Magnets

$PMSM$ Permanent Magnet Synchronous Motor

PWM Pulse width modulation

p Pole pair

p_{Fe} Iron losses

Q Reactive power

q Number of slots per pole per phase

R Resistance

$R_{@20}$ Value of the phase resistance at 20°C

R_{phase} Phase resistance

$R_{ph\text{-}ph}$ Phase to phase resistance

r_i Inner radius of the rotor

r_o Outer radius of the rotor

$S_{Cu,slot}$ Copper area in the slot

S_{slot} Slot area

SPMM Surface Permanent Magnet Motor

S Cross sectional area of the lamination sample

so Slot opening

T Torque

V_0 Statistical distribution of the local coercive field

VSI Voltage Supply Inverter

V_{ph_ph} Phase to phase voltage

$V_{ph,rms}$ RMS value of the phase voltage

$V_{ph,max}$ Peak value of the phase voltage

w_{pm} Length of the magnets

w_{st} Top stator slot

w_{sb} Slot bottom width

w_{tt} Top tooth

w_{tb} Tooth bottom width

X Phase reactance

Z Number of conductors in series per phase

Z Phase impedance

Chapter 1

Introduction

1.1 Brushless Motors

In the traditional synchronous machine, the inductor flow is produced through a special excitation circuit. However, when is not required the regulation of this flow, synchronous machines with a permanent magnets (Permanent Magnet Synchronous Motor, PMSM) can be used. This possibility, which allows to reduce the dimensions of the rotor and to reduce (or almost) Joule losses of excitement, is particularly exploited in the realization of small and medium power synchronous motors (generally <50 kW, but there are some even over 100 kW), intended for a variable frequency power supply.

The system consisting of a synchronous permanent magnet motor, its power supply and from its control system it is usually defined as "brushless motor". The arrangement of the magnets on the rotor can be superficial Figure 1.1 a), or the magnets can be immersed in the rotor iron (internal magnets: Figure 1.1 b) or c).

a) external magnets   *b) internal magnets*   *c) radial magnets*
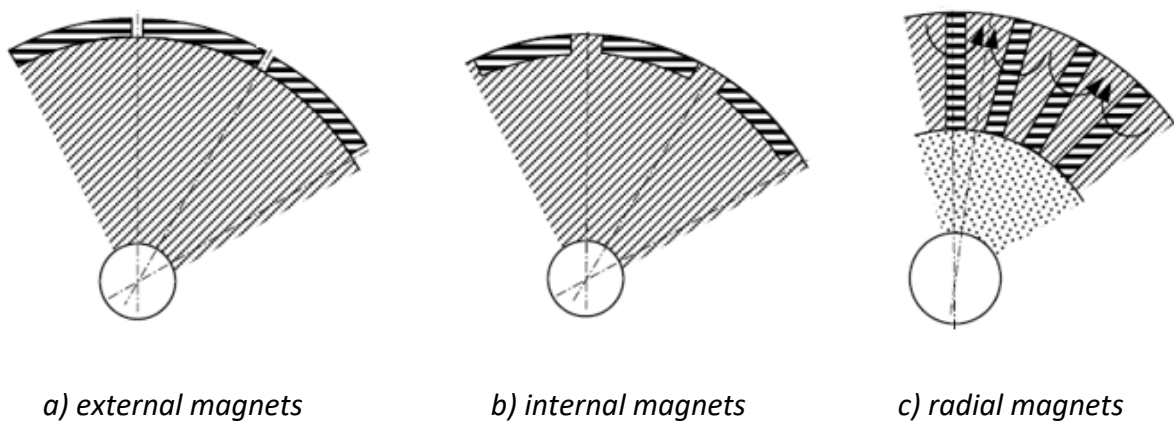
Figure 1.1: Different configuration of the permanent magnets

In cases a and b, the magnets have the magnetized surfaces at the air gap. In case c, the magnets are arranged radially in the rotor, the magnetization takes on transversal course and the flow is conveyed to the air gap through the sectors of soft ferromagnetic material.

In this way, the machines can be made with high number of poles and obtain an air gap concentration with values of induction higher than those available in the individual magnets.

The stator generally maintains its shape typical of synchronous and asynchronous machines, with a three-phase winding distributed in the slot, but the stator may be realized in the version with concentrated windings.

Some brushless motors can be considered as permanent magnet direct current motors with electronic switch: this applies in particular to the brushless motors controlled with the trapezoidal technique, called precisely *brushless DC motor*. In fact, both in direct current motors and in brushless motors, the vectors representative of the stator and rotor fields, are (ideally) 90 ° out of phase electric.
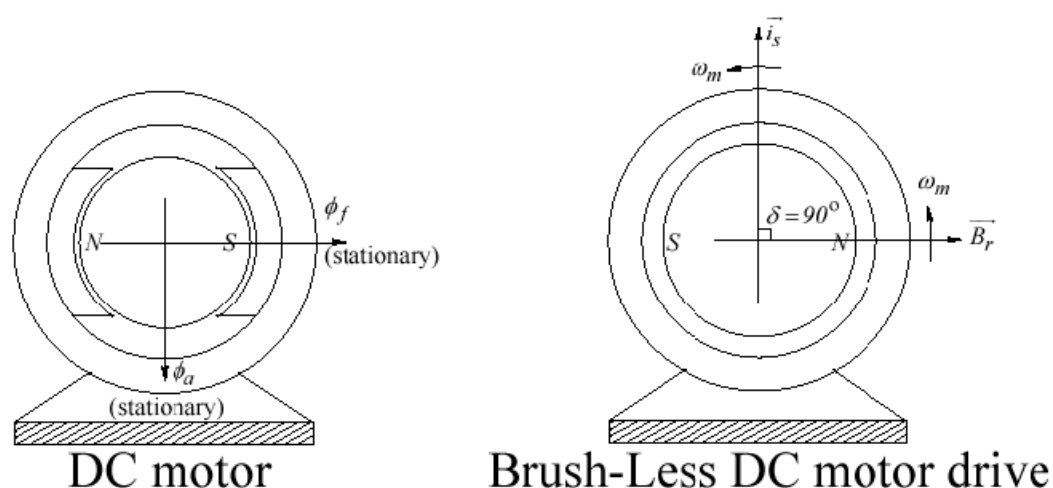
Figure 1.2: Vectors representative of the stator and rotor fields in Brushless motor

In brushless motors the field produced by the rotor permanent magnets is rotating; the rotating field produced by the currents circulating in the three stator windings is maintained on average 90° in advance by the action of the control on the inverter that powers the motor. To achieve this, the stator windings are powered by an inverter, whose static switches are switched by a control system based on the signals logic provided by a position sensor coaxial to the rotor. In this way, the distribution of stator currents changes in synchronism with the position of the rotor and therefore the stator rotating magnetic field results (ideally) in advance of 90 ° electrical compared to the rotor, in any operating condition.

1.1.2 Control of brushless motors

The purpose of the current control is to copy a DC motor, obtaining a torque proportional to the armature current:

$$T = k_a \cdot I_a \tag{1.1}$$

Even in the brushless motor the purpose is the same, but the further problem is to make the torque independent of the angular position. The risk is that the torque varies according to the angular position periodically, therefore the machine tends to accelerate / decelerate to keep the torque constant.

The control structure is reported in Figure 1.3:
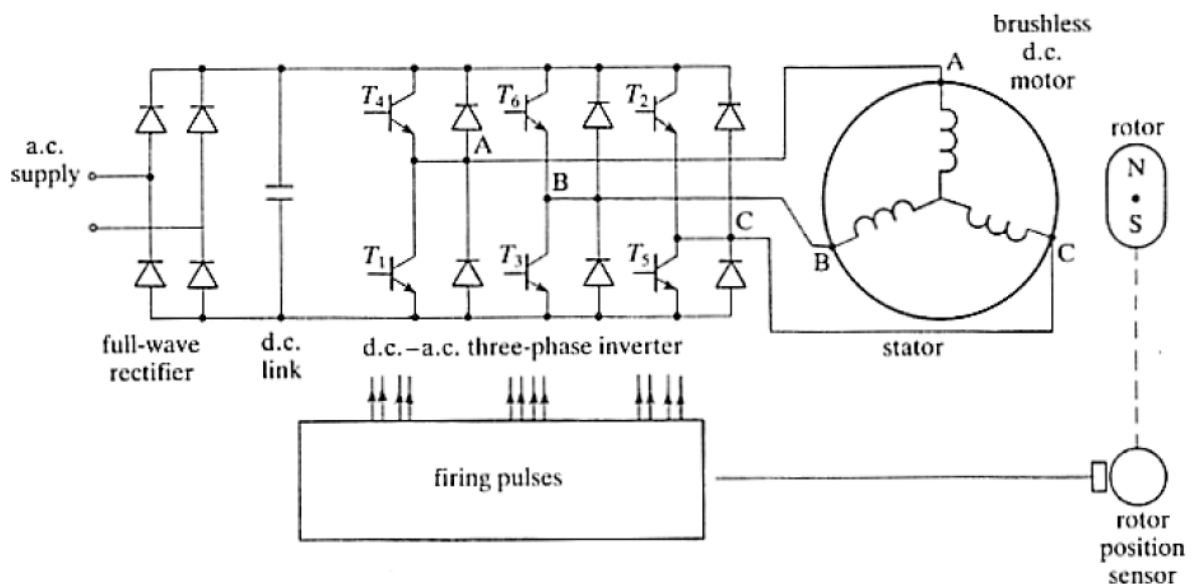
Figure 1.3: Control of brushless motor

The motor is powered by a VSI (Voltage Supply Inverter) and the current control is carried out by appropriately modulating the inverter closings and openings. If the connection is a star without neutral, there are only two independent currents, therefore two are measured and the third is calculated. In the control block the information relating to the angular position, the information of the phase currents of the machine and the reference of the currents are the input values, all is controlled so that the inverter maintains the current reference. The currents are controlled according to the rotor angle and therefore position sensors are required.

3

The control of the brushless motor can be achieved through the trapezoidal technique or sinusoidal technique. These techniques differ from each other in the waveform of the current, set by the converter and in the phase counter-electromotive force, dependent on the arrangement of the stator windings and the arrangement / shape of the rotor magnets. The motor that uses the trapezoidal technique is also called DC brushless (BLDC) because it is equivalent to the dual of a DC switching motor with permanent magnet excitement. In both cases the current in the conductors must reverse polarity each time a permanent magnet pole passes in front of it, in order to maintain the couple unidirectional.

1.2 High-speed electrical machine applications

High speed rotating electric machines are used for many engineering applications for their advantages: for example, in the aerospace industry, in the automotive industry, and in the precision engineering industry for machine tools, equipment, and tooling used in the manufacture of domestic appliances, optics, etc. This type of electric machines has advantages in terms of reduction of system weight, useful in automotive application, where the weight is directly related to emissions and fuel burn. The use of high-speed machine allows the elimination of intermediate gearing and the use of direct drives. High-speed electric machines find employment in different fields.

In automotive field, the use of a high-performance traction machine integrated within hybrid drivetrains is useful to improve fuel efficiency and to reduce emissions. The machine has a dual function: on starting and gear shift, it has the function of motor, to increase the speed up to the required one, while at high engine loads, it has the function of generator to prevent shaft overspeeding. The use of a power turbine and a high-speed motor, can improve the driveline efficiency, recovering energy from the exhaust gases, that can be used to supply the vehicle's electrical loads. In internal combustion engine, the exhaust gas recirculation is used to reduce NO_x emissions, but this can give a negative pressure due to an exhausting backpressure greater than the intake air pressure. To solve this problem an EGR compressor, driven by a high-speed machine, can be inserted at the upstream of the turbine.

Another application is in flywheel energy storage system. Electric energy is converted in mechanical energy using a motor that spins a flywheel. Then, the energy is stored. The mechanical energy can be converted back into electrical energy, using the same motor to slow the flywheel down. Modern flywheels can rotate at higher speeds, to achieve higher power, higher efficiency and longer lifetime than the common NiMH batteries typically used in hybrid vehicles.

The high-speed machines are also used for spindle applications, when a higher rotational speed, low vibration and speed control are required.

Another application of high-speed motors, is for turbomolecular pumps, used to create or maintain the vacuum exploiting the collision of the gas molecules with a moving solid

surface. The rotor blades impact the gas molecules, pushing them towards the subsequent statoric ones. The impact against these, thanks to their orientation, makes the molecules pass to the next rotor, where the process repeats itself. The turbomolecular pumps are composed of many stages of rotor and stator pairs in series and rotating blades at high speed. The rotor runs in vacuum, it causes thermal exchange problems; moreover, the torque ripple must be very low to avoid the risk of resonance in the rotating system.

High-speed machines are also used to drive compressors to minimize the environmental, regulatory, and maintenance issues. An advantage is the elimination of the lubrification oil system and of the gearbox, with consequent reduction of operations and maintenance costs.

The use of high-speed machine for industrial air compressor and air blowers, allows to get higher durability and reduced noise.

Another application is for microturbines, small combustion turbine, used to generate energy at sites with space limitation, with few moving parts, high efficiency, low emissions.

1.3 Problems of high speeds electrical machines

Despite the advantages of high-speed machines, there are some problem related to them.

One issue, for example, is related to losses. The core losses are very high, due to the significant working frequency (1000-10000rpm). Moreover, there are eddy current in the permanent magnet and in the winding; this causes an increase of the Joule losses, because the skin effect is significant. The alternating electric current is distributed unevenly inside a conductor: its density is greater on the surface and lower inside, so, there is an increase of the wire's resistance, this phenomenon is called "skin effect". At high speed, it is not negligible, because for a circular wire the resistance increases proportionally to the square root of the frequency. The increase of the resistance, generate higher Joule losses. Consequently, there is an increase of the temperature and a cooling system must be provided, with a consequent increase in weight and size of the machine. High-speed machine needs a rotor sleeve to contain the magnets, it can be made of titanium or carbon fiber. The eddy-current in the sleeve makes some problem for the permanent magnets.

The working high-speed causes also mechanical limitations, for example for bearings and shaft, indeed the centrifugal forces and the stress in the rotor materials became very high, this is a problem, especially for the permanent magnets, because they have a low flexural and tensile strength. For this problem the permanent magnets of high speeds machines must be contained in a non-magnetic sleeve, which limit the tension in the magnets. Another problem correlated to the high speed is the noise.

In PM machines, the maximum stresses, is the tangential stress in the inner surfaces of the permanent magnets and of the sleeve. Reference [3].
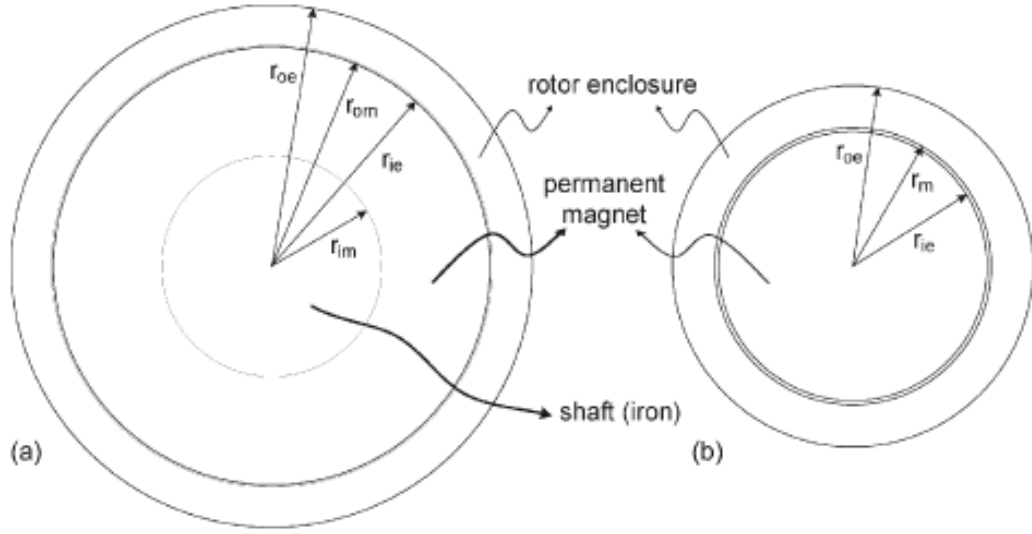
Figure 1.4: Models of PM motor

The Theory of Tresca and Von Mises, define a reference stress that in all points must be lower than the ultimate stress of the material.

$$\sigma_{ref} < \sigma_U; \quad r_i < r < r_o; \quad w < wmax \tag{1.2}$$

Where σ_U is the ultimate stress of the material, depending on the type of the material, r_i is the inner radius of the rotor and r_o is the outer radius of the rotor, w_{max} is the maximum value of the speed range application. Using the equilibrium and congruence equations, it is possible to write the radial and circumferential stresses:

$$\sigma_r = \frac{E}{(1-v)}A + \frac{E}{(1+v)}\frac{B}{r^2} - \frac{3+v}{8}\rho r^2 w^2 \tag{1.3}$$

$$\sigma_c = \frac{E}{(1-v)}A + \frac{E}{(1+v)}\frac{B}{r^2} - \frac{1-3v}{8}\rho r^2 w^2 \tag{1.4}$$

Where *E* is the Young's modulus, *υ* is the Poisson's coefficient, the coefficients *A* and *B* are obtained from the boundary conditions:

$$\sigma_{rm}(0) \neq \infty \tag{1.5}$$

$$\sigma_{re}(r_{ie}) = \sigma_{rm}(r_{im}) \tag{1.6}$$

$$\delta = u_e(r_{ie}) - u_m(r_m) \tag{1.7}$$

8

$$\sigma_{re}(r_{oe}) = 0 \tag{1.8}$$

The parameters are indicated in Figure 1.4, while δ is the shrinkage, or the interference fit, defined as:

$$\delta = r_{om} - r_{ie} \tag{1.9}$$

The boundary surface conditions to respect in all the speed range, are:

$$\sigma_c(r_m) \leq \sigma_{max} \tag{1.10}$$

$$\sigma_r(r_m) \leq 0 \tag{1.11}$$

Another aspect that is influent in high speeds machines is the vibration. When the frequency of the vibration is the same of one of the natural frequencies of the rotor-bearing system, there is the resonance phenomenon, that is a problem. Critical speeds, at which the resonance phenomenon occurs, must be avoided, so the goal is to compute the maximum speed which the rotation becomes unstable and self-excited vibrations take place. Is used the Jeffcott model, the rotor is considered as a shaft with a concentrated mass in one point.

$$\omega \leq \omega_{cr}(1 + \frac{c_n}{c_r}) \tag{1.12}$$

Where ω_{cr} is the critical speed of the system, c_n is the viscous equivalent of the rotor external damping and c_r is the viscous equivalent of the rotor internal dumping. The dynamical speed limit of a PM machine is represented by the first critical speed. To compute it, it is used the Timoshenko's beam model. The non-dimensional stiffness is defined as:

$$k* = \frac{kl^3}{EI_y} \tag{1.13}$$

Where k is the stiffness of the bearings, l is the shaft length, I_y is the surface moment of inertia. It is possible to compute the first critical speed when $k*$ tends to infinite.

$$\Omega_{cr1} = \frac{\pi^2}{l^2}\sqrt{\frac{EI_y}{\rho A}} \tag{1.14}$$

A is the cross section of the shaft.

The critical speed changes if it is considered a rotor not placed in the middle of the shaft, in this case there is a gyroscopic moment, that causes an increase of the critical speed.

In practice the critical speed is computed using finite-element modelling (FEM).

1.4 Materials of high speeds machines

I. *Electrical steel*

The material of the stator and rotor core must be chosen to obtain an optimal in terms of losses, mass, size parameters, power, magnetic flux density, cost.

For the stator and rotor laminations, silicon-iron (SiFe) alloys or cobalt-iron (CoFe) alloys can be used. CoFe has higher saturation magnetization and consequently, higher power density, but it is more expensive compared with SiFe. The lamination is really important for the core losses. In general, a thinner lamination gives lower core losses. For high frequency application, the thickness is generally 0.1 mm.

II. *PMs*

The permanent magnet used in high-speed machine are subjected to mechanical stress and to losses, due to flux pulsation and air-gap space harmonics. In high-speed machine are generally used NdFeB magnet or SmCo magnet, with a high work temperature. In some application are also used magnets in ferrite because of the lower cost than the rare-earth magnets.

III. *Sleeve*

High speed machine needs a rotor to contain magnets, to counteract the centrifugal forces. It can be made as a single nonmagnetic sleeve (Figure 1.5 a) or wound on the HCPM with a composite material filament glued with epoxy resin (Figure 1.5 b).

a)   b)
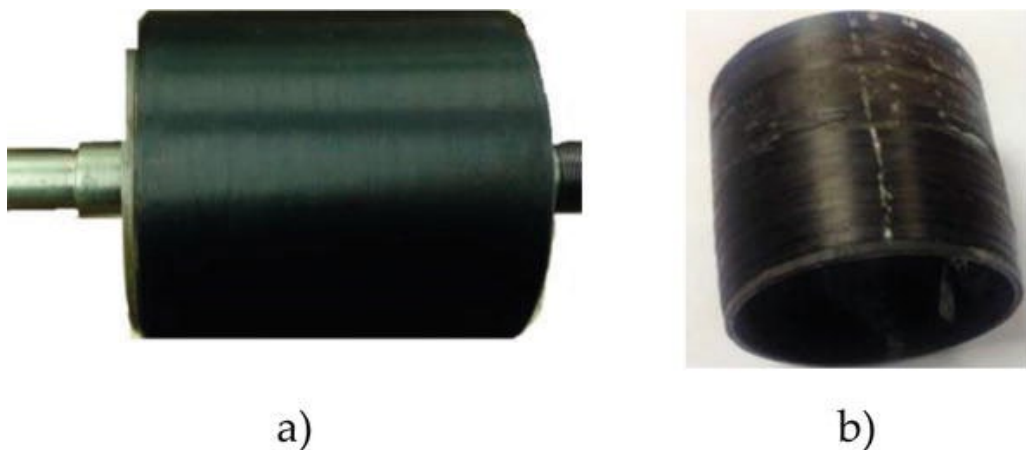
Figure 1.5: Rotor sleeve

The use of composite material is more technological, but it is required a special winding equipment, so the solid non-magnetic sleeves are usually preferred. The material used for these types of sleeve are titanium or carbon fiber. The material of the sleeve should have a minimum electrical conductivity to limit the problems related to eddy current and heating.

Chapter 2

Reverse Engineering of an Existing Machine for FEM Model Calibration

2.1 Introduction of the SPM electrical machine

The electrical machine considered is a Surface Permanent Magnet Motor. The stator is realized in M270-35 A, laminated, the outer diameter is 47.8 mm. The rotor is in a stainless steel (1.4122) and it is not laminated, the radial thickness is 7 mm. The magnets, arranged superficially, are in NdFeB, with a radial thickness of 2 mm, with one pole pair. The sleeve, to contain the magnets, is made in a carbon fiber, with a thickness of 1 mm. The airgap is 1 mm. The shaft diameter is 9.8 mm. The active length of the machine is 11 mm. The motor has 12 slots, there are 64 conductors in each slot, 4 conductors in parallel per phase. The winding layout is a single-layer. The rated speed of the motor is 60000 rpm, the frequency is 1000 Hz, the rated torque is 0.034 Nm, while the rated cogging torque is 0.0002 Nm. The rated current is 5.2 A_{rms}, while the rated voltage in load conditions at the terminals of the machine is 26.2 V_{rms}, the power factor is 0.98. The winding phase resistance is 0.1325 Ω. The voltage constant is 0.0004 V/rpm and the torque constant is 0.0066 Nm/A.
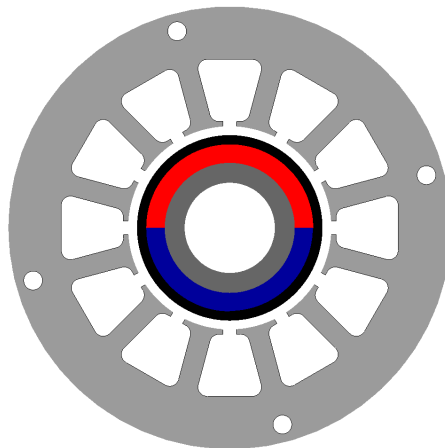
Figure 2.1: Motor section

In the following table are reported the motor materials:

Table 2.1: Material of each motor part

Motor part	Material
Stator	M270-35A
Rotor	M270-35A
Magnet	NdFeB (N33H)
Sleeve	CFK 411
Winding	Copper

The input dates are subdivided as follows:

- Design target

- Winding specification

- Design constraints

I. *Design target*

- Rated torque: 0.034 Nm

- Rated speed: 60000 rpm

- Rated phase-to-phase voltage at machine terminals: 26.2V

- Number of rotor poles: 2

II. *Winding specifications*

The winding layout is the sequent one:
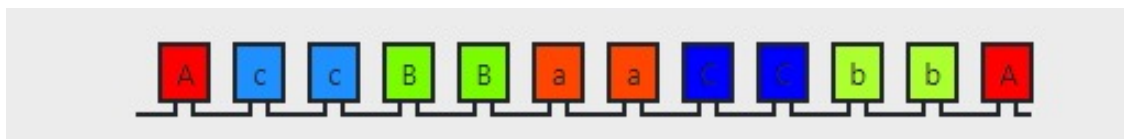
Figure 2.2: Winding Layout
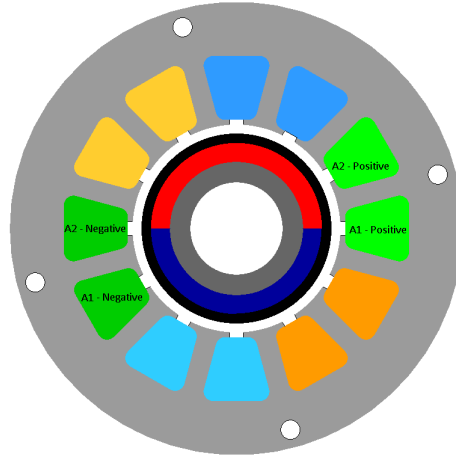
Figure 2.3: Winding Layout in the motor

There are 64 conductors in each slot, 4 conductors in parallel per phase. The winding layout is a single-layer.

For the winding diameters, 5 different measurement have been performed, using a microscope. The measurement results are reported in the following table.

Table 2.2: Diameter measurements

Measurements	Diameter [µm]
1	460.18
2	482.09
3	450.00
4	453.37
5	491.23

From these measures it follows that the conductors can are made of AWG 25, with a diameter of 0.455 mm.

III. *Design constraints*

The design constraints are divided in geometric constraints (airgap height, aspect ratio λ, slot dimensions, magnet radial thickness, magnet polar pitch, slot fill factor), permissible active materials stress indexes (maximum teeth, stator yoke flux, rotor yoke flux density, stator

current density) and material specifications (stator and rotor iron core materials, lamination stacking factor, permanent magnet data, permanent magnet temperature, winding temperature) .

Starting from the input data it is possible to compute all the others quantities.

2.2 Sizing procedure

I. *Air gap flux density calculation*
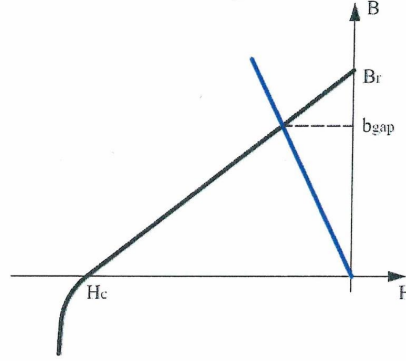
Figure 2.4: Qualitative characteristic curve for a permanent magnet

The magnet working point can be found as the intersection between the PM characteristic and the airgap characteristic, where B_{gap} is the maximum value of the airgap flux density. It is assumed the hypotesis of infinite permeability for the magnetic circuit.

$$b_{gap} = B_r \cdot \frac{h'_{pm}}{h'_{pm} + h'_{gap}}$$

(2.1)

B_r is the magnet residual flux density at the working temperature of the magnet, $h'_{pm} = h_{pm}/\mu_r$ and h'_{gap} is the real air gap length, equal to the product of the actual gap h_{gap} and the Carter coefficient to consider the stator slotting effect.

α_{pm} is the magnet circumferential coverage (in percentage of half pole pitch)

$$\alpha_{pm} = \frac{\alpha_{pm}^{\circ}}{180^{\circ}}$$

(2.2)

The peak value of the fundamental airgap flux density (b_{gap_fund}) is:

$$b_{gap\_fund} = \frac{4}{\pi} \cdot b_{gap} \cdot \sin \alpha$$

(2.3)

Where α is the half pole angle in electrical degrees.

Then, it is possible to write the peak value of the fundamental air gap flux density as follows:

$$b_{gap\_fund} = \frac{4}{\pi} \cdot b_{gap} \cdot \sin(\alpha_m \cdot \frac{\pi}{2}) \qquad (2.4)$$

II. *Sizing procedure and equation for the inner rotor structure*

At the start, the internal rotor diameter D_{ir} is fixed equal to minimum inner diameter imposed by the designer (d_{min}), while the external rotor diameter D_{er} is a little higher.

$$D_{pm} = D_{er} + 2 \cdot h_{pm} \qquad (2.5)$$

$$D_{gap} = D_{pm} + h_{gap} \qquad (2.6)$$

$$D_{is} = D_{pm} + h_{gap} \qquad (2.7)$$

Where D_{pm} is the diameter of the external surface of the permanent magnets, D_{gap} is the diameter at the middle of the airgap, D_{is} is the stator inner diameter, h_{pm} is the permanent magnets thickness and h_{gap} is the airgap thickness.
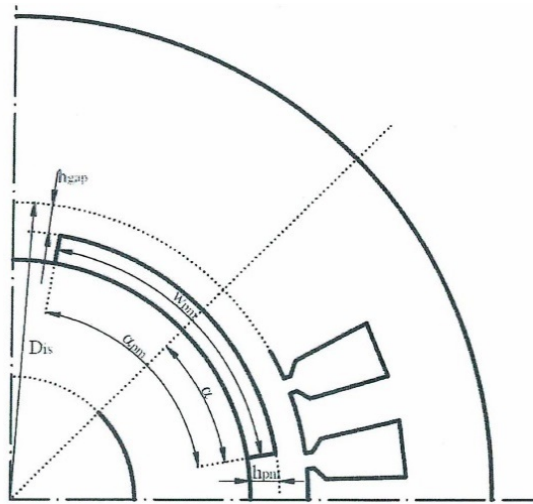
Figure 2.5: Cross section sketch for an inner rotor structure

The axial length of the lamination can be derived from the aspect ratio λ and the stator inner diameter.

$$L_{at} = \lambda \cdot D_{is} \qquad (2.8)$$

The length of the magnet can be calculated as:

$$w_{pm} = \alpha_{pm} \cdot \tau_p \tag{2.9}$$

Where α_{pm} is the magnet circumferential coverage and τ_p is the polar pitch:

$$\tau_p = \frac{\pi \cdot D_{pm}}{2 \cdot p} \tag{2.10}$$

The total magnetic flux per pole and its fundamental value, are computed as follows:

$$\Phi_p = w_{pm} \cdot b_{gap} \cdot L_{at} \tag{2.11}$$

$$\Phi_{p\_fund} = \frac{2}{\pi} \cdot \tau_p \cdot b_{gap\_fund} \cdot L_{at} \tag{2.12}$$

The maximum flux in the yokes corresponds to half of the flux produced by each magnet.

The effective rotor yoke flux density with the actual external rotor diameter is given by the following equation:

$$b_{yr} = \frac{\frac{\Phi_p}{2}}{\frac{D_{er} - D_{ir}}{2} \cdot L_{at} \cdot k_{fe}} \tag{2.13}$$

Where k_{fe} is the lamination stacking factor fixed by the user.

At the start of the sizing procedure, when the external rotor diameter is fixed a little higher than the shaft diameter, the rotor yoke height is small, consequently the effective flux density is high. To reduce this value, the external rotor diameter of the machine is increased.

The internal stator diameter can be expressed as follows:

$$D_{is} = D_{pm} + 2 \cdot h_{gap} \tag{2.14}$$

The rated electromagnetic torque is defined as follows

$$T_{elm} = \frac{\sqrt{2} \cdot \pi}{4} \cdot b_{gap\_fund} \cdot A \cdot D_{is}^2 \cdot L_{at} \cdot k_{avv} \cdot k_{skew} \tag{2.15}$$

Where A is the linear current density, k_{avv} is the fundamental harmonic winding factor and k_{skew} is the skew factor (equal to 1 if the machine is not skewed, as in our case).

The rated electromagnetic torque is a desired parameter, so it is possible to compute the linear current density A and then the conductive material area in the stator slots:

$$a_{Cu} = \frac{A \cdot \pi \cdot D_{is}}{J_s \cdot n_{slot}} \tag{2.16}$$

Where J_s is the stator conductors current density and n_{slot} is the number stator slot, both are input parameters.

The slot useful area can be computed by the input slot filling factor:

$$a_{us} = \frac{a_{Cu}}{k_{fill}} \tag{2.17}$$

The slot current is:

$$I_{slot} = a_{Cu} \cdot J_s \tag{2.18}$$

III. *Stator lamination design*

The stator yoke flux is half of the flux produced by each magnet:

$$\frac{\Phi_p}{2} = b_{ysmax} \cdot h_{ys} \cdot L_{at} \cdot k_{fe} \tag{2.19}$$

Where h_{ys} is the stator yoke thickness, computed as follows:

$$h_{ys} = \frac{b_{gap}}{b_{ysmax} \cdot k_{fe} \cdot 2 \cdot p} \cdot D_{is} \cdot \frac{\alpha_{pm} \cdot \pi}{2} \tag{2.20}$$

The top tooth width is computed as follows:

$$w_{tt} = \frac{b_{gap}}{b_{tsmax} \cdot k_{fe}} \cdot \frac{\pi \cdot D_{is}}{n_{slot}} \tag{2.21}$$

The top stator slot width is:

$$w_{st} = \frac{\pi \cdot (D_{is} + 2 \cdot h_{ics})}{n_{slot}} - w_{tt} \tag{2.22}$$

Considering trapezoidal slot shape, the useful slot area can be expressed as:

$$a_{us} = \frac{w_{st} \cdot w_{sb}}{2} \cdot h_{us} \tag{2.23}$$

Where w_{sb} is the slot bottom width and h_{us} is the slot useful height.

$$w_{sb} = \tau_{sb} - w_{tb} \tag{2.24}$$

Where τ_{sb} is the bottom slot pitch:

$$\tau_{sb} = \frac{\pi \cdot (D_{hics} + 2 \cdot h_{us})}{n_{slot}} \tag{2.25}$$

where D_{hics} is the diameter:

$$D_{hics} = D_{is} + 2 \cdot h_{ics} \tag{2.26}$$

The top stator slot width w_{st} can be written as follows:

$$w_{sb} = w_{st} + \frac{2 \cdot \pi \cdot h_{us}}{n_{slot}} \tag{2.27}$$

Where h_{us} is the slot useful height computed by the equations of a_{us} and w_{sb}:

$$h_{us} = \frac{-w_{st} + \sqrt{w_{st}^2 + \frac{4 \cdot \pi \cdot a_{us}}{n_{slot}}}}{\frac{2 \cdot \pi}{n_{slot}}} \tag{2.28}$$

The second order equation with the sign minus is not been considered because it is not consistent.

Defined the slot dimensions, is possible to calculate the slot height h_{ts}, and the total slot area a_{ts}:

$$h_{ts} = h_{us} + h_{ics} \tag{2.29}$$

$$a_{ts} = a_{us} + so \cdot h_{es} \cdot \frac{so + w_{st}}{2} \cdot h_{is} \tag{2.30}$$

Where *so* is the slot opening.

The geometric tooth dimension can be expressed as follows:

$$w_{tt} = \frac{\pi \cdot D_{hics}}{n_{slot}} - w_{st} \tag{2.31}$$

$$w_{tb} = \frac{\pi \cdot (D_{is} + 2 \cdot h_{ts})}{n_{slot}} - w_{sb} \tag{2.32}$$

$$h_{tooth} = \frac{(D_{es} - D_{is})}{2} - h_{ys} - h_{ics} \tag{2.33}$$

The stator outer diameter is given by the following equation:

$$D_{es} = D_{is} + 2 \cdot (h_{es} + h_{is} + h_{us} + h_{ys}) \tag{2.34}$$

The sizing procedure is finished only if the design constraints are respected and the design target are achieved.

2.3 FEM Model

2.3.1 Geometry, Parameters, Materials, Face Region, Mechanical set

Defined all the parameters, it is possible to model the motor in the software FLUX. All the simulations are 2D Transient magnetic simulations, initialized by static computation. First of all, the geometry of the machine is created. In the section "Geometry" are defined all the parameters (such as speed, phase resistance, number of coils etc.) In the section "Physic" are created 4 different materials: CFK411 for the carbon fiber sleeve, copper for the windings, M270-35A for the iron rotor and stator, NdFe_N33H for the magnets. Another step is to create the face and assign them to the regions. There are 20 different faces: stator, rotor, phaseA1 and A2 positive and negative, phase B1 and B2 positive and negative, phase C1 and C2 positive and negative (for positive or negative orientation of the current in the region), carbon fiber sleeve, rotating airgap, static airgap, compressive airgap, PM positive and negative for the permanent magnets. The three coils are linked to a circuit. The stator is laminated, the thickness of the sheet iron is 0.35 mm and the stacking factor is 0.95. The pre-slot area is set as "Air or vacuum region". There are three different mechanical set: the static one, which is for the static parts (stator, winding, static airgap), the rotating one, which is for the rotating parts (rotor, permanent magnet, carbon fiber sleeve, rotating airgap) and compressive, for the airgap between the static and rotating airgap. The airgap is divided in three different part to have a higher accuracy of the mesh.

2.3.2 Equivalent circuit for FEM simulations

Another step is the equivalent electric circuit of the machine.

In Figure 2.6 is reported the Electric circuit. The coils are assigned to the phase region of the winding. The following electric circuit will be modified to replace the no-load and the load scenarios, in the picture are reported only the coils.
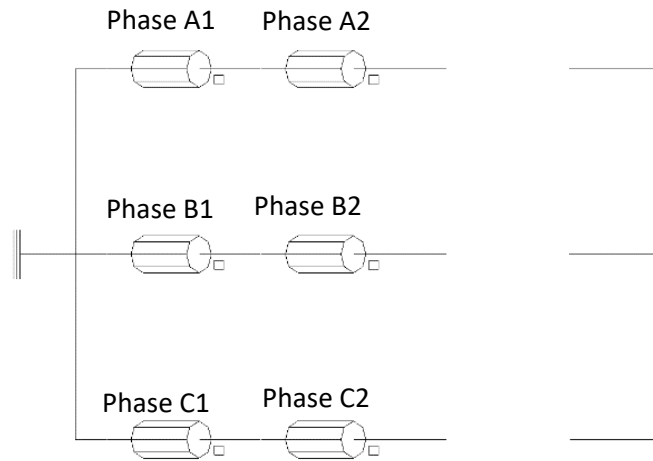
Figure 2.6: Electric circuit used for FEM simulations

2.3.3 Magnetization of the permanent magnets

Two different magnetizations have been investigated: radial and parallel magnetization.

I. *Radial magnetization*
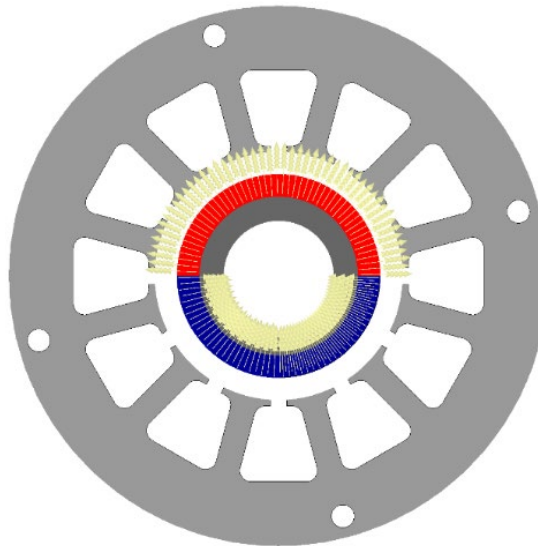
Figure 2.7: Radial magnetization of the permanent magnets

With the radial magnetization, the EMF is not sinusoidal, the waveform is the following:
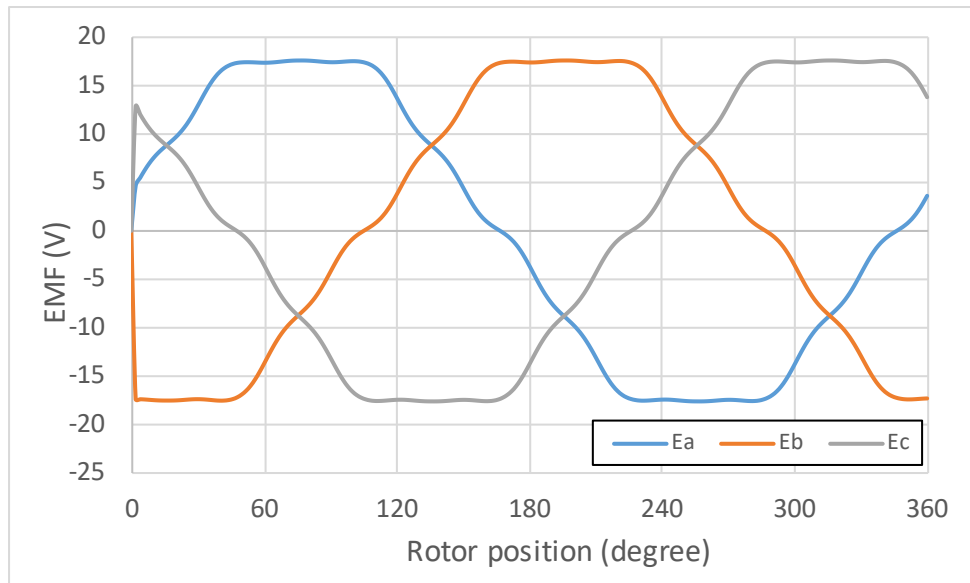
Figure 2.8: EMF with radial magnetization

II. *Parallel magnetization*
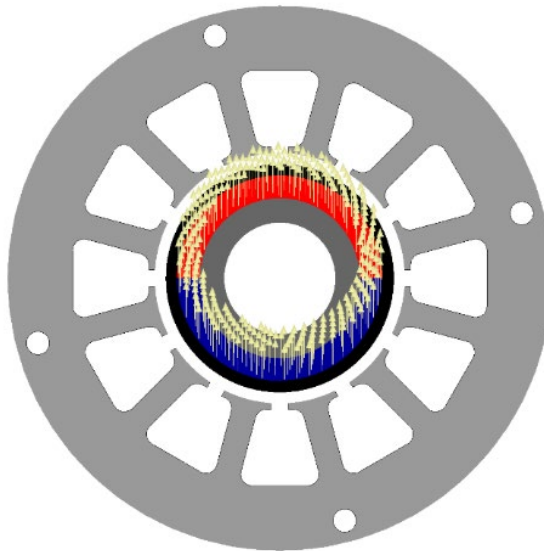
Figure 2.9: Parallel magnetization of the permanent magnets

With the parallel magnetization, the EMF is sinusoidal, the waveform is the following:
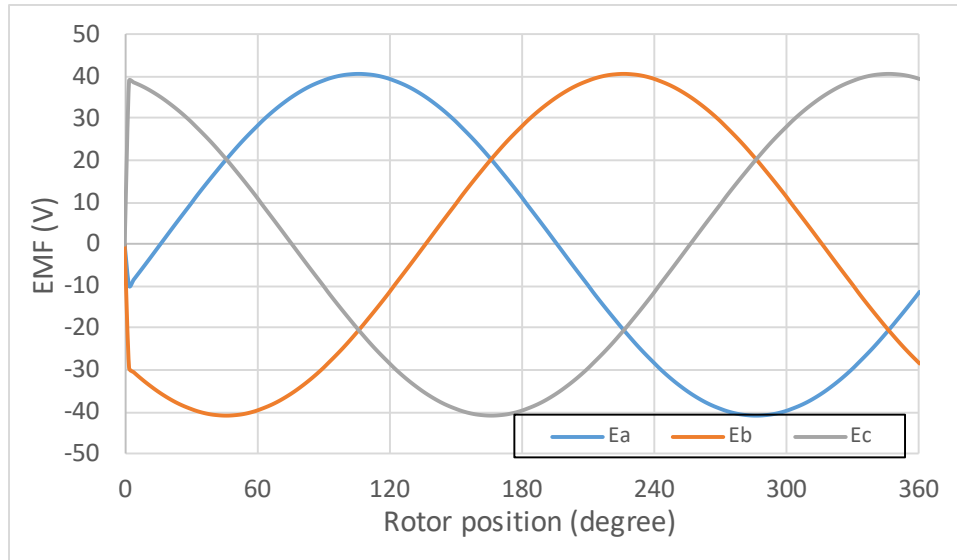
Figure 2.10: EMF with radial magnetization

Consequently, it is assumed a parallel magnetization for the model. Now it is possible to run the simulation.

2.3.4 Definition of B_r for the calibration at the test temperature

It is performed a test on the motor for the computation of the main parameters, the results are reported at the end of the Chapter. The test on the motor is performed at 20 degree, at a speed of 335 rpm and the back-electromotive force has a peak value of 194,3 V (phase-to-phase). The goal is to calibrate the residual induction of the permanent magnet in FLUX to obtain the same value of EMF. The default temperature assumed by FLUX is 20°C. To consider the no-load conditions, the electrical circuit needs to be modified. Three big resistance (10^{12} Ω) are put is series with the coils to consider it as an open circuit.
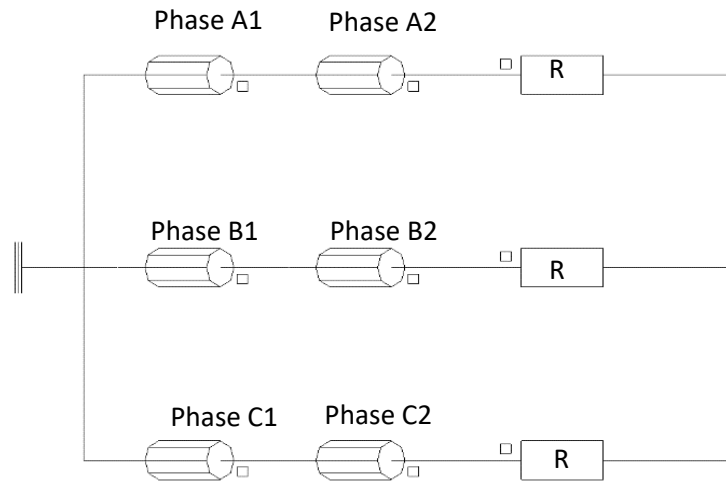
Figure 2.11: Electric circuit used for FEM simulations in no load conditions

The speed is set at 335 rpm, as the real speed at test condition. As first try value it is assumed B_r equal to 1.17 T. In section "Solver" of the software, the scenario is created. The mechanical position is chosen between -4 and 360 degree, with a step value of 2. The start value is not zero because at the start there is a transient and the quantities have big variation before settling down. The software also allows to control some parameters via scenario. From the result of the simulation, it follows that the B_r must be set to 1.05 T to obtain the EMF of the test condition. The EMF obtained with the new value of residual induction is reported in Figure 2.12, its peak value is 203.4 mV.
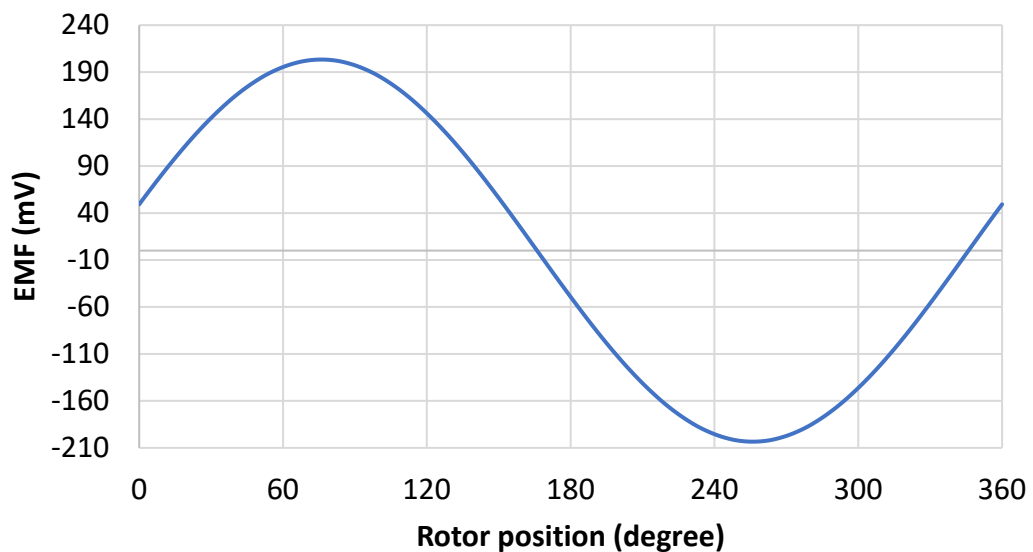
Figure 2.12: EMF by FEM at test condition

2.4 Simulation in No-Load conditions

- EMF

Once the model is defined, the no-load conditions can be simulated. The only parameter that must be changed is the speed, from 335 rpm (speed test), to 60000 rpm (rated speed), the mesh must be improved to have a correct result of the cogging torque.
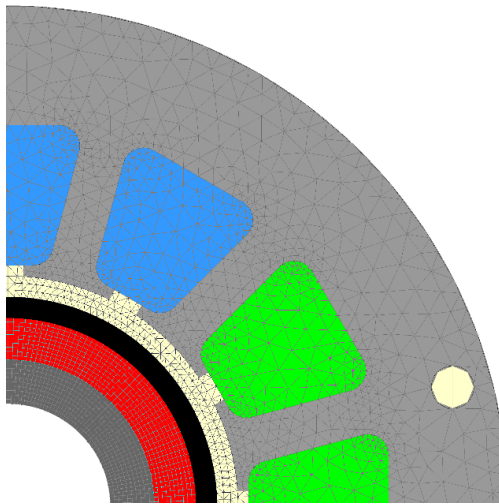
Figure 2.13: Meshed motor

In figure 2.14 it is reported the waveform of the EMF, the peak value is 21 V as it is shown in the FFT Analysis of the EMF in Figure 2.15.
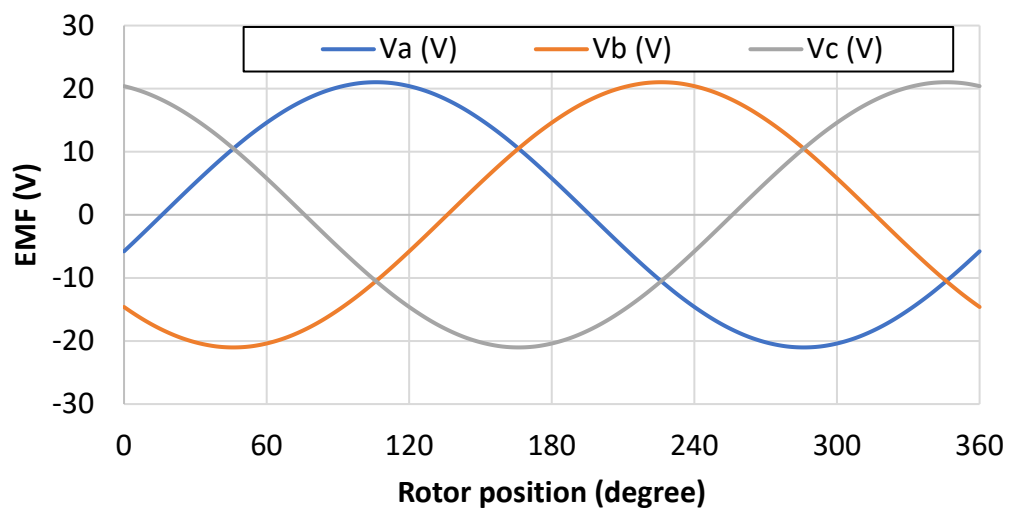
Figure 2.14: EMF at no-load conditions obtained via FEM
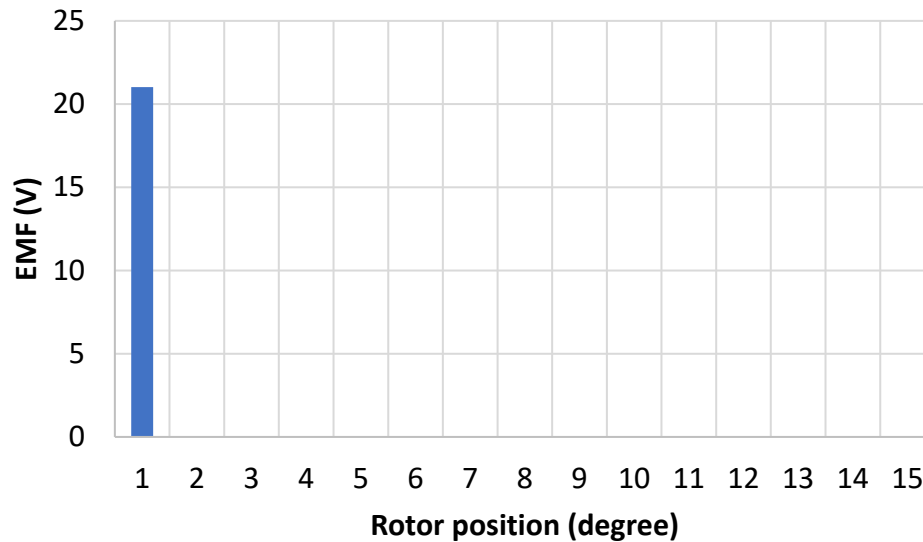
Figure 2.15: FFT of the EMF at no-load conditions

- Cogging torque

The cogging torque is the torque due to the interaction between the permanent magnets and the stator slots, it is due to changes in the reluctance of the magnetic circuit and it is recognizable when the shaft is rotated by hand slowly. The cogging torque, of electromagnetic nature, is always present, even when there is no stator current: for this reason, it is possible to evaluate it qualitatively by turning manually the rotor of motor disconnected from the grid. It is generated by the magnetic attraction between the stator teeth and the permanent rotor magnets due to the rotation of the rotor. It is due to the circumferential component of the attractive force that tries to maintain the alignment between stator teeth and permanent magnets: the rotor tends to align with the maximum number of stator teeth to have the minimum reluctance of a flow line and maximum stored magnetic energy. The cogging pair adds an oscillating component to the constant torque desired by the machine: this can produce vibration, noise and a waveform of the phase current not perfectly sinusoidal, especially at low speed. This phenomenon can be detected in the spectrum of vibrations at one frequency multiple of the rotor speed, which depends on the number of poles and stator slots. The cogging torque can be reduced limiting the change in the reluctance of a flow line, for example, skewing the sides of the magnets compared to those of the stator slots. The cogging torque is adversely affected by the partial

29

demagnetization of the magnets, caused for example by overtemperatures or overcurrent. The cogging torque is a "no-current torque", so it is obtained in the no-load simulation.

The cogging torque is reported in Figure 2.16, while the FFT is in Figure 2.17.
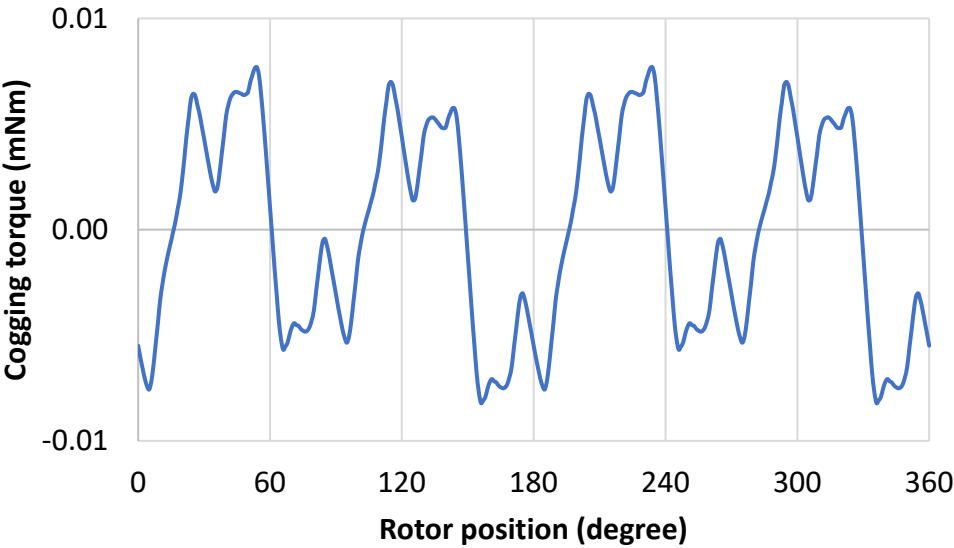
Figure 2.16: Cogging torque
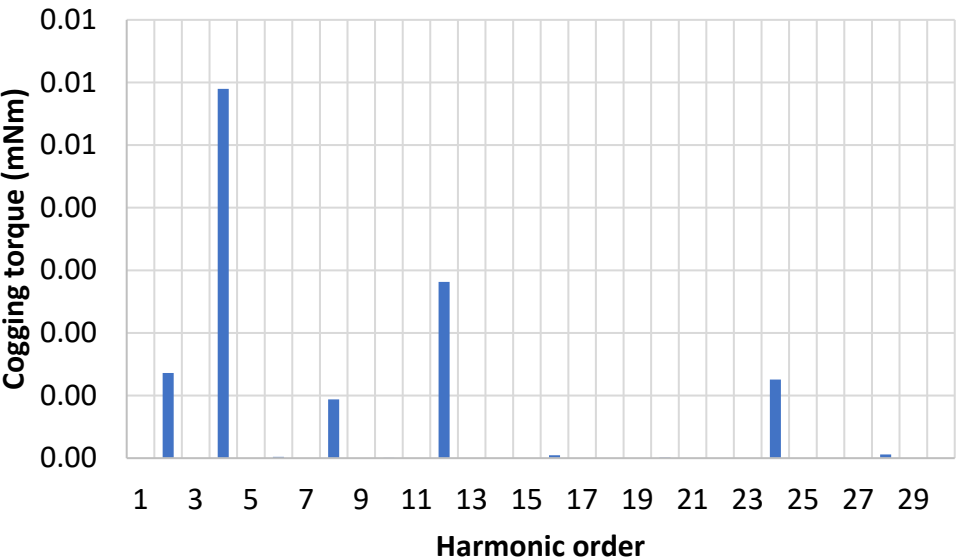
Figure 2.17: FFT of the cogging torque

2.5 Simulation in Load Conditions

- Electromagnetic torque

Considering the three windings with isolated neutral:
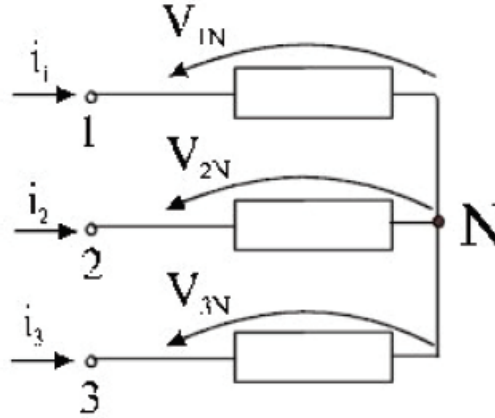
Figure 2.18: Windings with isolated neutral

The voltages can be written as sum of a contribution due to the resistance and a contribution due to the variation over time of the total flow linked with winding:

$$\begin{cases} i_1 = R \cdot i_1 + \dfrac{d\lambda_1}{dt} \\ i_2 = R \cdot i_2 + \dfrac{d\lambda_2}{dt} \\ i_3 = R \cdot i_3 + \dfrac{d\lambda_3}{dt} \end{cases}$$

(2.35)

(2.36)

(2.37)

That flow is in part due to auto and mutual inductances, while in the other part it is due to magnets.

In matrix form:

$$[V] = R \cdot [i] + \frac{d[\lambda]}{dt}$$

(2.38)

Knowing the flux, the equation (2.38) becomes:

$$[V] = R \cdot [i] + L_{eq} \cdot \frac{d[i]}{dt} + \frac{d[\lambda_m]}{dt} = R \cdot [i] + L_{eq} \cdot \frac{d[i]}{dt} + [e] \qquad (2.39)$$

In surface mount brushless motors, the L_{eq} is a real number that does not depend on time but is tied to the machine and is also constant due to the isotropy of the machine; the stator currents and the rotor flow can vary, according to the position of the rotor inside the stator. The voltage is given by the sum of three terms:

- resistive drop

- inductive drop

- f.e.m. due to permanent magnets

The equivalent circuit is the following one:
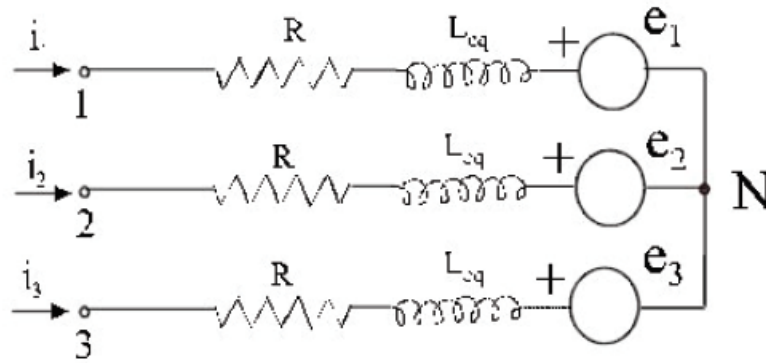
Figure 2.19: Equivalent circuit considering resistive drop, inductive drop, f.e.m. due to permanent magnets

To calculate the torque, it is possible to think of powering the motor and evaluate each contribution through an energy balance, obtaining the contribution of mechanical power and consequently the torque.

The power in input in the machine is:

$$P = V_{1N} i_1 + V_{2N} i_2 + V_{3N} i_3 \qquad (2.40)$$

In matrix term it is possible to write:

$$[i]^T \cdot [V] = [i]^T \cdot R \cdot [i] + [i]^T \cdot L_{eq} \cdot \frac{d[i]}{dt} + [i]^T \cdot [e] \qquad (2.41)$$

$[i]^T \cdot [V]$ represents the input electric power in the windings

$[i]^T \cdot R \cdot [i]$ represents the Joule losses

$[i]^T \cdot L_{eq} \cdot \frac{d[i]}{dt}$ represents the temporal derivative of magnetic energy

$[i]^T \cdot [e]$ is the mechanical power

$$[i]^T \cdot [e] = [i]^T \cdot \frac{d[\lambda_m]}{dt} = [i]^T \cdot \frac{d[\lambda_m]}{d\theta} \cdot \frac{d\theta}{dt} = [i]^T \cdot \frac{d[\lambda_m]}{d\theta} \cdot p \cdot w_m \qquad (2.42)$$

The torque is obtained dividing for the mechanical speed:

$$T = [i]^T \cdot \frac{d[\lambda_m]}{d\theta} \cdot p \qquad (2.43)$$

The expression of the torque in d-q axis is the following one:

$$T = \frac{3}{2} \cdot p \cdot \lambda_m \cdot i_q \qquad (2.44)$$

The equation shows that the torque produced, in the case of an isotropic machine, depends only on the component in the q axis of the stator current, because there is no reluctance torque if there is no difference between the inductances in the d and q axes. If the current is not exactly in the q axis, the torque decrease.

In the simulation at load-conditions it is necessary to consider the effect of the temperature. A temperature of 90°C must be considered and it must be taken into account in the model. Are created the parameters ALPHA and ALPHA_M which are respectively the thermal coefficient of the copper and the temperature coefficient of remanence of the magnets, so the phase resistance and the residual induction of the magnets are modified as follows:

$$R_{phase} = R_{@20}(1 - \alpha \cdot (90 - 20)) \qquad (2.45)$$

Where R$_{@20}$ is the resistance at 20°C and α is 0.00393.

$$B_r = B_{@20}(1 - \alpha_M \cdot (90 - 20)) \qquad (2.46)$$

Where B$_{@20}$ is the residual induction at 20°C and α_M is -0.00115.

The equivalent electric circuit shown in Figure 2.11 must be modified because the stator windings are not open but are fed with sinusoidal current. In the circuit are used only two current generators, because the third current will be automatically computed by the other two, because the windings are in star connection:

$$i_c = -(i_a + i_b) \qquad (2.47)$$

The equivalent circuit is the following:
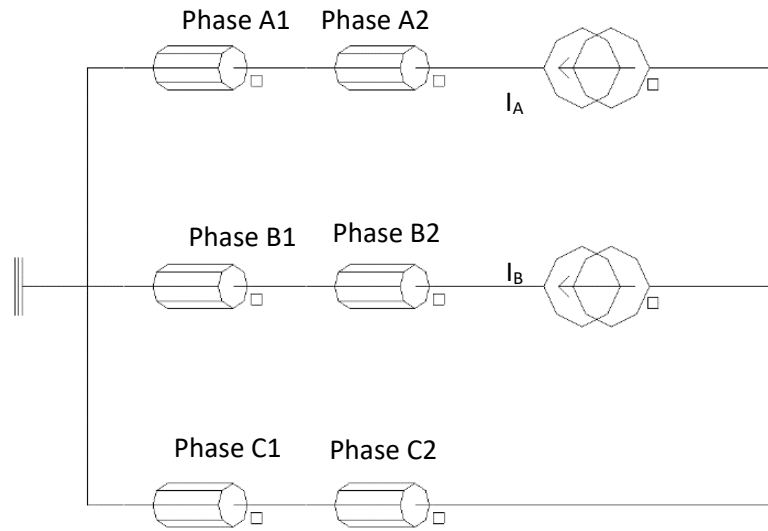
Figure 2.20: Electric circuit used for FEM simulations in load conditions

It is decided to supply current in the q axis. In FLUX are created the two parameters ID and IQ. IQ is set as 7.35 A because the rated current provided by the company is 5.2 A$_{rms}$, while ID is set equal to 0A.

It is necessary to pass from d,q components to a,b,c components. The parameters I_ALPHA and I_BETA are created, their values come from the inverse Park transformation (it is a transformation that retains the modules of the quantities). For the transformation it is needed the electrical angle, which is equal to the mechanical one, because there is only a pole pair.

$$i_\alpha = i_d \cdot \cos \theta_e - i_q \cdot \sin \theta_e \qquad (2.48)$$

$$i_\beta = i_d \cdot \sin \theta_e + i_q \cdot \cos \theta_e \qquad (2.49)$$

To compute the currents in a,b,c components from the alpha and beta components, it is used the inverse Clark transformation, assuming the homopolar current equal to zero. Consequently:

$$I_A = I_\alpha \qquad (2.50)$$

$$I_B = -\frac{1}{2} \cdot I_\alpha + \frac{\sqrt{3}}{2} \cdot I_\beta \qquad (2.51)$$

After running the simulations, the EMF and the phase current are plotted. As it is possible to see in Figure 2.21, they are not in phase, but there is a shift between the phase current and the phase voltage. It means that the current is not supplied exactly in the q axis, but a little bit is also in the d axis.
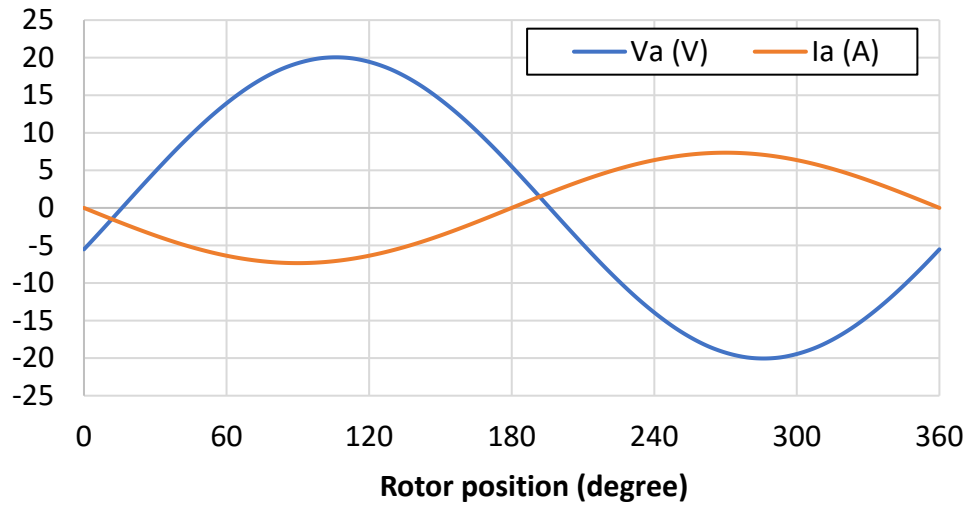
Figure 2.21: EMF and phase current for the phase A before the adjustment

The shift is deleted adding an offset angle ANG_TMAX equal to -195 degree.

$$i_\alpha = i_d \cdot \cos(\theta_e + ANG\_TMAX) - i_q \cdot \sin(\theta_e + ANG\_TMAX) \qquad (2.52)$$

35

$$i_\beta = i_d \cdot \sin(\theta_e + ANG\_TMAX) + i_q \cdot \cos(\theta_e + ANG\_TMAX) \qquad (2.53)$$

After the adding of ANG_TMAX, the EMF and the current are in phase, as it is possible to see in Figure 2.22.
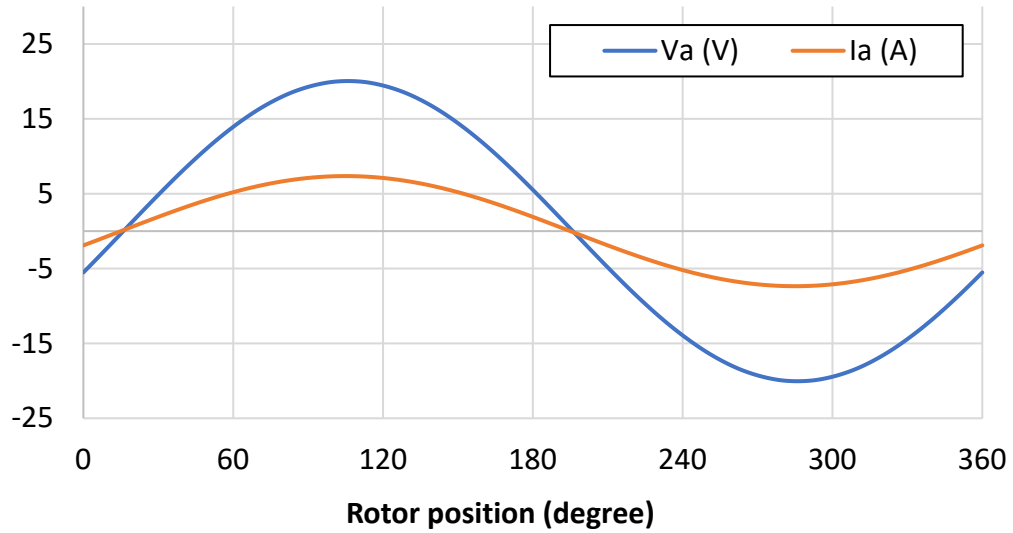
Figure 2.22: EMF and phase current for the phase A after the adjustment

Now the model for the simulation in load conditions is finally ready.

2.5.1 Results

In Figure 2.23 it is reported the phase voltage in load conditions, the peak value is 21.1 V. In Figure 2.25 it is reported the phase-to-phase voltage, the peak value is 36.5 V.

In Figure 2.24 and 2.26 are reported the FFT of the phase voltage and of the phase-to-phase voltage.
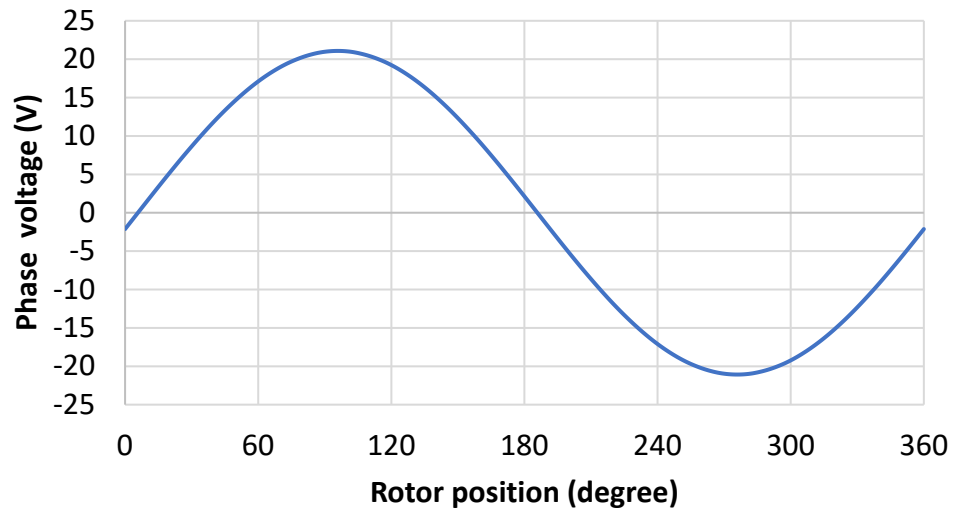
Figure 2.23: Voltage of the phase A in load conditions
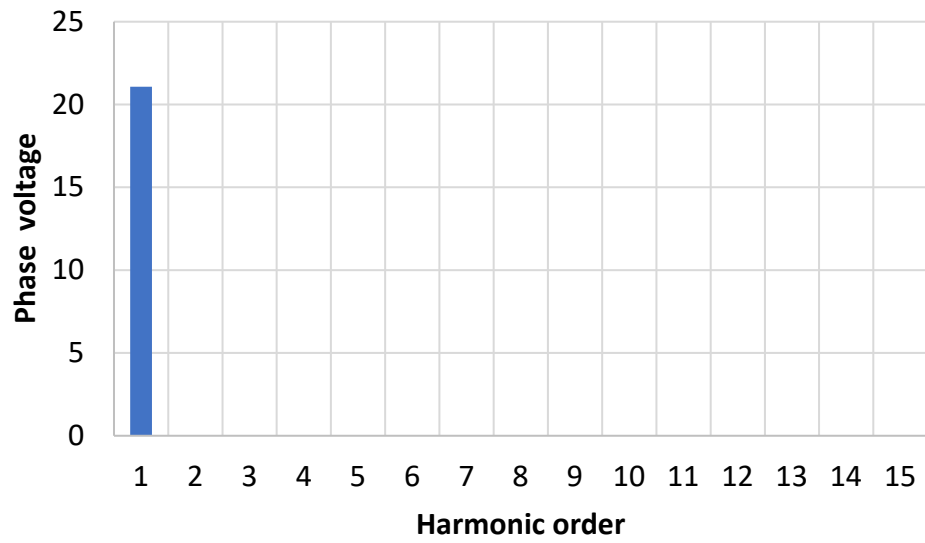
Figure 2.24: FFT of the phase voltage in load conditions
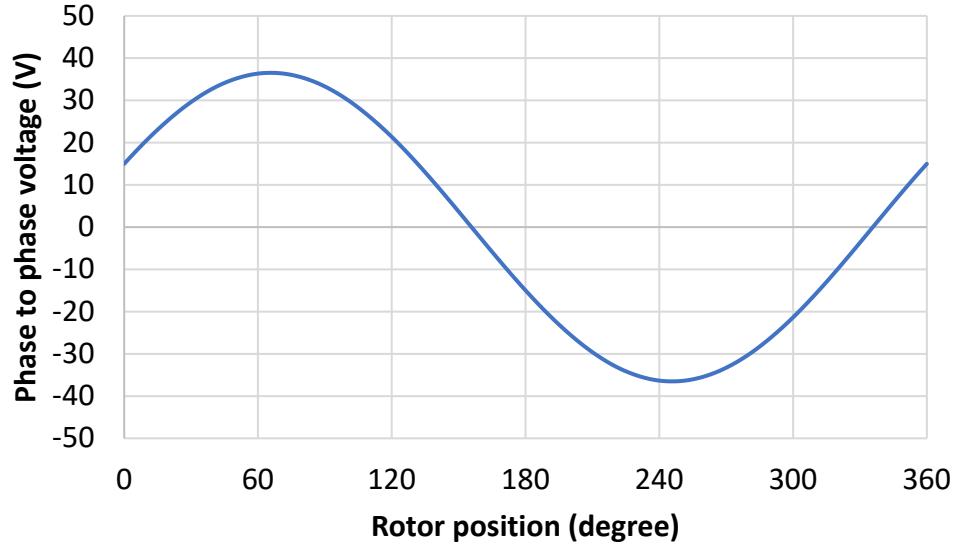
Figure 2.25: Phase to phase voltage in load conditions
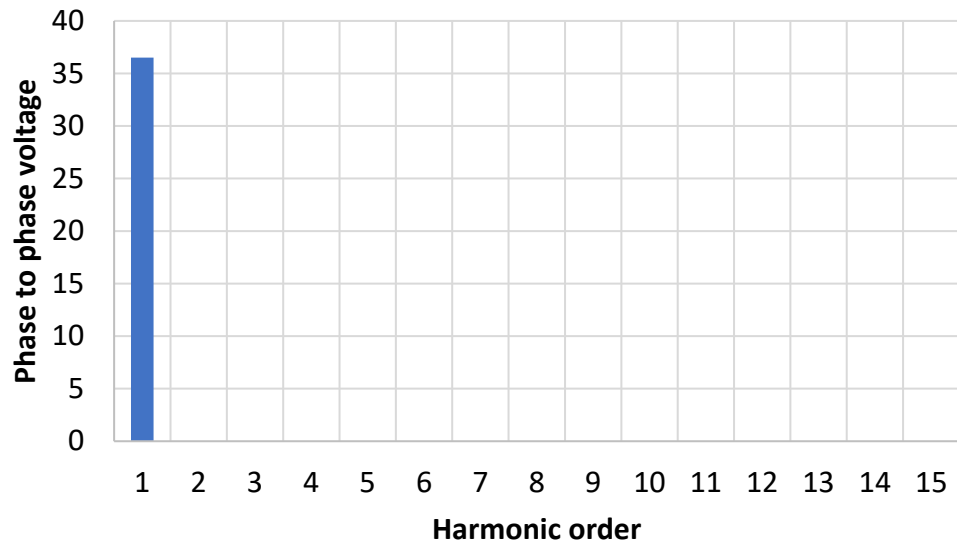
Figure 2.26: FFT of the EMF voltage in load conditions

The rated phase to phase voltage value provided by the company is 26.2 V rms.

$$V_{ph-ph} = 26.2 \ V \qquad (2.54)$$

$$V_{ph,rms} = 15.13 \ V \qquad (2.55)$$

$$V_{ph,max} = 21.4 \ V \qquad (2.56)$$

Consequently, it is possible to see that the voltage phase obtained by FEM is closer to the rated voltage phase.

2.5.2 Torque

The electromagnetic torque obtained by FLUX has an average value of 34 mNm, the waveform is reported in Figure 2.27 and and it is possible to see that it has a very small ripple. In Figure 2.28 is reported the FFT Analysis. The torque obtained is the same of the rated one provided by the company.
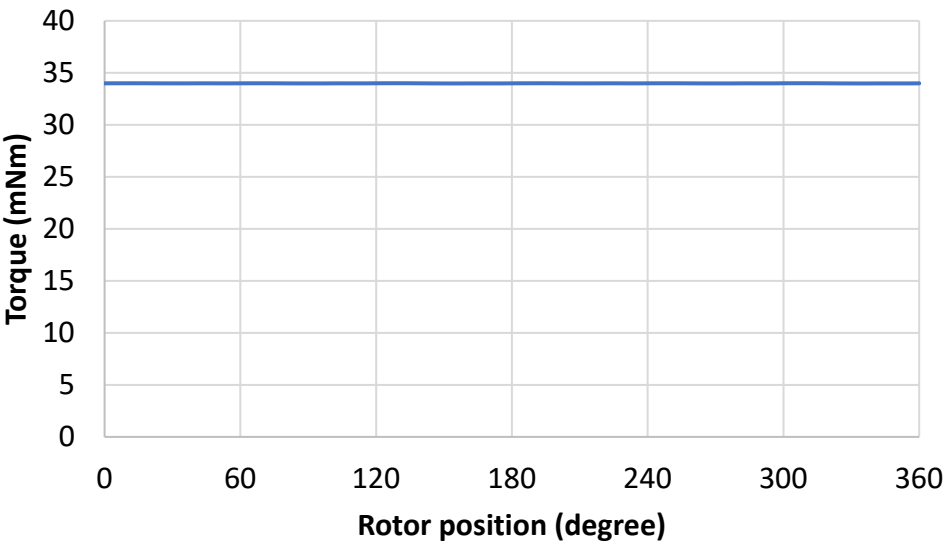
Figure 2.27: Torque
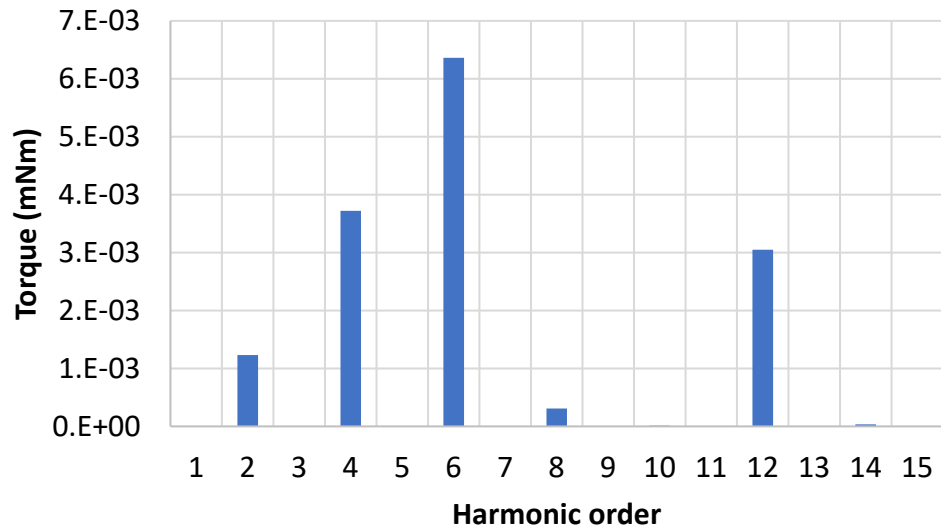
Figure 2.28: FFT of the torque

2.5.3 Torque-current trend

For the simulation of the torque-current trend, the scenario needs to be changed. The current is controlled via scenario and varies from 0 A to 10 A, with a step value of 2 A. For each value of current, it is computed the average torque and then the values are plotted in the Figure 2.29.
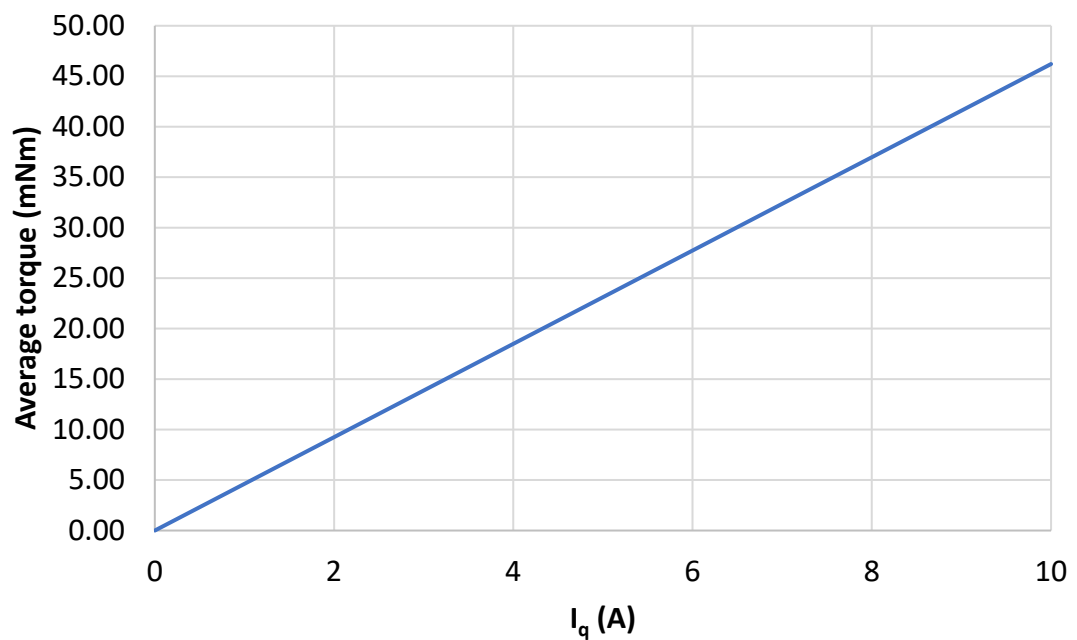
Figure 2.29: Torque-current trend

From the results of the simulation is it possible to see that in this current range there are no problems of saturation.

2.6 Test on the high-speed machine

Based on the current prototype and on the presented algorithm for the design of high-speed electrical machine, it is possible to validate some of the given parameters, just to verify if they are the same provided by the company and to check if the model is good.

I. *Phase to phase resistance*

The given resistance is R_{ph-ph} = 0.265 Ω.

The measurement of the phase resistance is made considering a single-phase supply configuration, because the neutral point is not accessible in PMSMs, consequently, the measured resistance is a "dc resistance".

The measured resistance R_{ph-ph}, using the Volt-Amperometric method, at 21.7°C, is 0.266 Ω.
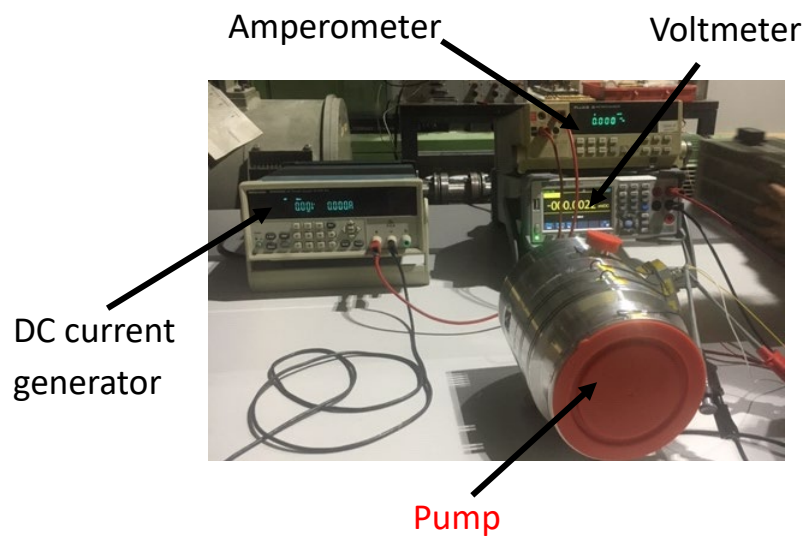
Figure 2.30: Measurements on the motor
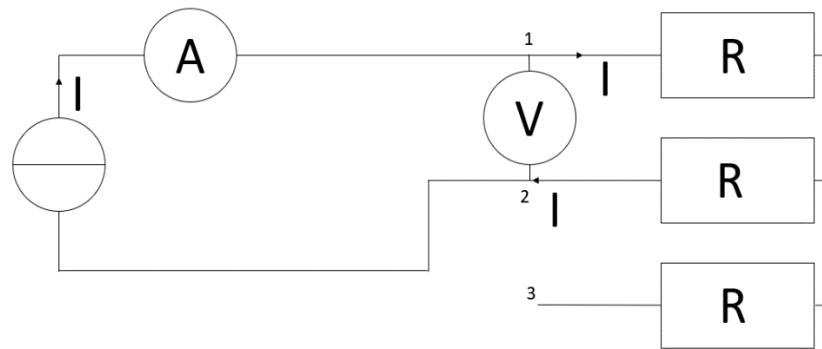
Figure 2.31: Volt-amperometric circuit

The measured values are reported in the following table:

Table 2.3: Measured resistance

Current [A]	Voltage [mV]	R [Ω]	Pin
0.5	133.15	0.2663	A-C
0.999	266.45	0.2667	A-C
0.999	266.57	0.2668	B-C
0.5	133.24	0.2665	B-C
0.5	133.6	0.2672	A-B
0.9995	267.23	0.267	A-B

II. *Voltage coefficient*

From the trend of the EMF in function of the time, reported in Figure 2.32, it is obtained the period and consequently, the frequency and the speed.
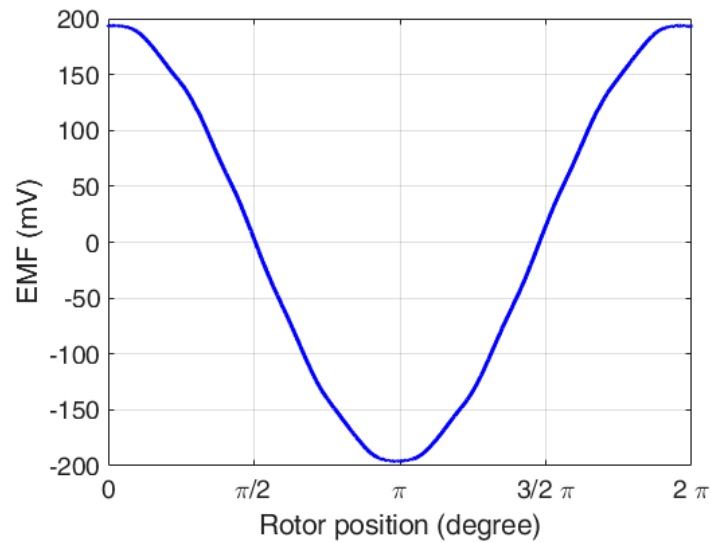
Figure 2.32: EMF in test conditions (@335rpm)

Table 2.4: Table with parameters for the Voltage coefficient

Data	Value
Period	179.1 ms
Frequency	5.58 Hz
Speed	335 rpm
Voltage coefficient	**0.41 mV/rpm**

The measured voltage coefficient is the same of the given one.

III. Synchronous Inductance

The computation of the synchronous inductance for three-phase permanent magnet machine is usually executing with offline tests, using different connection of the single phase of the stator winding. The neutral point in star connected machine is not accessible, so it is used a method based on the single phase supply configuration. In surface mounted permanent magnets machine, the magnets introduce a "magnetic anisotropy" in the stator teeth. The inductance-current trend is linear, because the magnets are seen as an equivalent airgap from the fluxes produced by the stator currents. The rotor of the machine is blocked

in two different position, one with the rotor axis (called PM or IRON) parallel with the magnetic axis of the phase 1 assumed as reference and the other one perpendicular to the magnetic axis of the phase 1, (Figure 2.33).
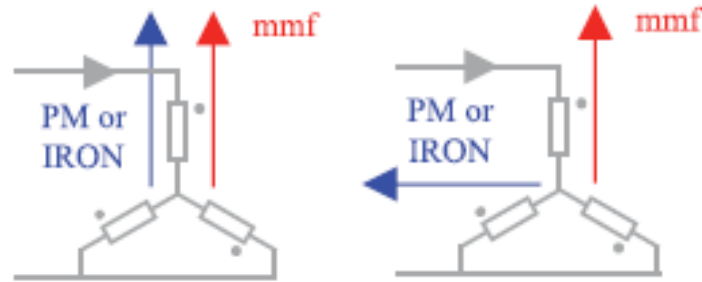
Figure 2.33: Different configurations of the PM axis

For the test, the injected current is from 0 to 4 A (to avoid saturations problems). The measurements are repeated three times and then averaged. The white wire is the pin B, the yellow wire is the pin C and the red wire is the pin D. The colors reported are the ones of the wires welded by Politecnico di Torino, not the ones reported on the datasheet of the company.

The alignment in dc is effectuated considering the supply between the red wire and the parallel of the yellow and the white wires.

The first repetition is done considering a frequency of 500 Hz, the second and the third repetitions are done with a frequency of 1000Hz.

Table 2.5: First measurement at 500 Hz

I_{rms}	V_{rms}	P(W)	Q(Var)	S(VA)	PF	z	x	L_d
0.6	0.41	0.082	0.23	0.24	0.34	0.47	0.45	1.42E-4
1.17	0.83	0.33	0.91	0.97	0.34	0.47	0.45	1.44E-4
2.1	1.48	1.03	2.89	3.07	0.34	0.48	0.46	1.45E-4
3.1	2.19	2.22	6.3	6.68	0.33	0.48	0.46	1.46E-4
4	2.89	3.85	10.97	11.62	0.33	0.48	0.46	1.47E-4

Table 2.6: Second measurement at 1000 Hz

I$_{rms}$	V$_{rms}$	P(W)	Q(Var)	S(VA)	PF	z	x	L$_d$
0.34	0.44	0.63	0.14	0.15	0.22	0.87	0.86	1.37E-4
0.99	1.32	0.29	1.27	1.3	0.22	0.89	0.88	1.4E-4
2.02	2.73	1.22	5.38	5.52	0.22	0.9	0.89	1.42E-4
3.03	4.13	2.73	12.21	12.51	0.22	0.91	0.9	1.43E-4
4.03	5.53	4.8	21.78	22.31	0.22	0.92	0.91	1.44E-4

Table 2.7: Third measurement at 1000 Hz

Irms	Vrms	P(W)	Q(Var)	S(VA)	PF	z	x	Ld
0.34	0.44	0.03	0.14	0.15	0.22	0.87	0.86	1.37E-4
0.66	0.88	0.13	0.57	0.58	0.22	0.88	0.87	1.38E-4
0.99	1.32	0.29	1.27	1.3	0.22	0.89	0.88	1.40E-4
2.02	2.73	1.23	5.39	5.53	0.22	0.9	0.89	1.42E-4
3.02	4.13	2.74	12.21	12.52	0.22	0.91	0.9	1.43E-4
4.03	5.53	4.8	21.71	22.3	0.22	0.92	0.91	1.44E-4

2.7 Parameters computation

2.7.1 End-winding length
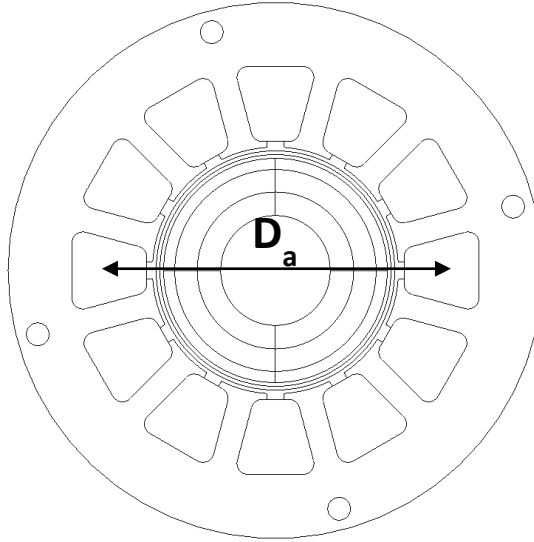
Figure 2.34: Average diameter D_a

The needed parameters are the number of slots per pole per phase q, the number of conductors in series per phase Z, the phase resistance R, the number of parallels path a.

$q = 2$

$Z = 64$

$a = 4$

$R_{phase} = 0.1325 \, \Omega \, (@ \, 20°C)$

Consequently, the number of turns is:

$$N_1 = q \cdot \frac{Z}{a} = 2 \cdot \frac{64}{4} = 32 \tag{2.57}$$

The average diameter D_a is 30.76 mm. It represents the distance between the middle of one slot and the middle of the diametral one (Figure 2.34). The active length L of the machine, as mentioned previously, is 11 mm.
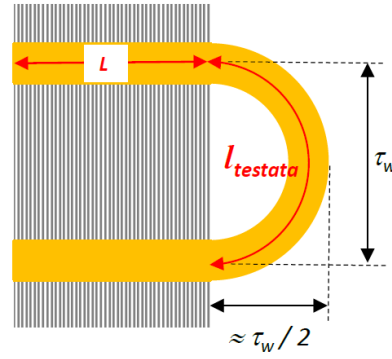
Figure 2.35: End winding

The winding pitch is easily calculated from the equation:

$$\tau_w = \frac{\pi \cdot D_a}{2 \cdot p} \cdot \frac{5}{6} = 0.0403 \ m \tag{2.58}$$

The factor $\frac{5}{6}$ is to take into account that the winding layout is not diametral. Knowing the wire diameter d_{wire} and the slot area S_{slot}, it is possible to compute the fill factor k_{fill}, obtained as the ratio between the area occupied only by copper and the total slot area. Consequently, the header length is computed and then the average length (referring to Figure 2.35) and finally the phase resitance.

$d_{wire} = 0.455 \ mm$ (AWG 25)

$S_{slot} = 37.1 \ mm^2$

$$k_{fill} = \frac{S_{Cu,slot}}{S_{slot}} = 0.28 \tag{2.59}$$

$$L_{header} = k_{header} \cdot \tau_w \tag{2.60}$$

$$L_{average} = 2 \cdot (L + L_{header}) \tag{2.61}$$

$$R = \rho \cdot \frac{L_{average} \cdot N}{S_{cond}} \tag{2.62}$$

The coefficient k_{header} takes into account the shape of the end winding, it can vary between 1.45 and 1.7.

From the equation (2.62), knowing the phase resistance, the resistivity (0.0174 Ωmm²/m @20°C), the wire diameter and the number of turns, it is possible to compute the average length of the winding.

$$L_{average} = \frac{S_{cond} \cdot R}{\rho \cdot N} = \frac{4 \cdot (\pi \cdot 0.455^2/4) \cdot 0.1325}{0.0174 \cdot (64/4) \cdot 2} = 0.155 \, m \tag{2.63}$$

From the equation 2.61, knowing the average length, it is possible to compute the length of the header.

$$L_{header} = \frac{L_{average}}{2} - L = 0.067 \, mm \tag{2.64}$$

Finally, it is possible to compute the header coefficient using the equation 2.60:

$$k_{header} = L_{header} \cdot \frac{1}{\tau_w} = 1.66 \tag{2.65}$$

2.7.2 Inductance computation

In rotating electrical machines, the total flux is given by the sum of the main flux and the leakage flux. The leakage flux does not take part to the energy conversion, consequently, more magnetic material is required than in the theoretic case without leakage flux. To take into account this phenomenon, the leakage slot inductance and the leakage end-winding inductance are subtracted from the magnetization inductance.

I. *Magnetization inductance*

It is expected that the magnetization inductance will be the same for the d and q axis because the surface mounted permanent magnets synchronous machine is isotropic.

The given parameters are the number or phase *m*, the pole pair *p*, the thickness of the effective airgap δ_0 met by the current linkage (obtained by the sum of the thickness of the airgap, of the sleeve and of the permanent magnets), the equivalent length *Lp* obtained by

multiplying the active length for the stacking factor 0.95, the winding pitch τ_w, the fundamental winding factor $k_{w,1}$, the number of turns and assuming the Carter factor equal to 1.

$m = 3$

$p = 1$

$\tau_w = 0.0403 \ m$

$\delta_0 = 0.004 \ m$

$L_p = 0.011 * 0.95$

$k_{w,1} = 0.966$

$N_s = 32$

$K_{Carter} = 1$

The flux of a single phase is computed as follows:

$$\Psi_m = k_{w,1} \cdot N_s \cdot \alpha_i \cdot \tau_w \cdot L_p \cdot \widehat{B_m} \qquad (2.66)$$

Where α_i is the ratio between the average flux density and the peak value of the flux density, for a sinusoidal flax density distribution, its value is $2/\pi$ and $\widehat{B_m}$ is the magnetic flux density in the airgap, that can be expressed in function of the current linkage $\widehat{\theta s}$.

$$\widehat{B_m} = \frac{\mu_0 \cdot \widehat{\theta s}}{\delta_0} \qquad (2.67)$$

Where $\widehat{\theta s}$ for a single phase is:

$$\widehat{\theta s} = \frac{4}{\pi} \cdot \frac{k_{w,1} \cdot N_s}{2 \cdot p} \cdot \sqrt{2} \cdot I_s \qquad (2.68)$$

Substituting the equation (2.68) e (2.68) in (2.66), it follows:

$$\Psi_m = k_{w,1} \cdot N_s \cdot \alpha_i \cdot \frac{\mu_0}{\delta_0} \frac{k_{w,1} \cdot N_s}{2 \cdot p} \cdot \tau_w \cdot L_p \cdot \sqrt{2} \cdot I_s \qquad (2.69)$$

Dividing the equation (2.69) for the peak value of the current, it follows:

$$L_m = \alpha_i \cdot \frac{2 \cdot \mu_0 \cdot \tau_w}{\pi \cdot p \cdot \delta_0} \cdot L_p \cdot (k_{w,1} \cdot N_s)^2 \qquad (2.70)$$

But this equation is for a single phase, so, multiplying the equation (2.70) for the number of phase *m* it is possible to compute the main magnetization inductance:

$$L_m = \frac{m}{2} \cdot \frac{2}{\pi} \cdot \mu_0 \cdot \frac{1}{2 \cdot p} \cdot \frac{4}{\pi} \cdot \frac{\tau_w}{\delta_0} \cdot L_p \cdot \left(k_{w,1} \cdot N_s\right)^2 = 7.7 \cdot 10^{-5} \text{ H} \qquad (2.71)$$

The main magnetization inductance is $7.7 \cdot 10^{-5}$ H.

II. *Leakage slot inductances*

The computation of the leakage slot inductance is related at the slot geometry and the winding arrangement.
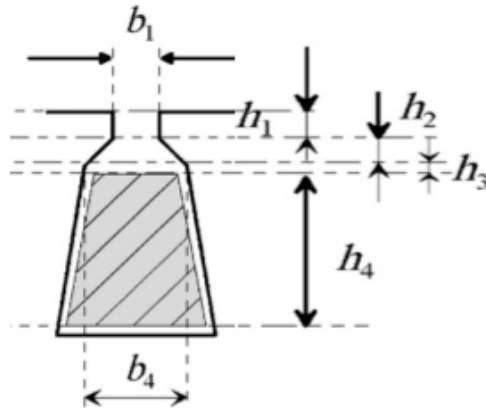
Figure 2.36: Trapezoidal slot for the leakage induction computation

The geometric known parameters are the following:

$h_1 = 0.526 \cdot 10^{-3}\ m$

$h_2 = 1.057 \cdot 10^{-3}\ m$

$h_3 = 0.643 \cdot 10^{-3}\ m$

$h_4 = 4.866 \cdot 10^{-3}\ m$

$b_1 = 1.5 \cdot 10^{-3}\ m$

$b_4 = 3.574 \cdot 10^{-3}\ m$

The permeance factor is given from the following equation:

$$\lambda_u = \frac{h_4}{3 \cdot b_4} + \frac{h_3}{b_4} + \frac{h_1}{b_1} + \frac{h_2}{b_4 - b_1} \cdot \ln \frac{b_4}{b_1} = 1.4269 \qquad (2.72)$$

The leakage inductance can be calculated with the equation (2.73).

$$L_u = \mu_0 \cdot l' \cdot \frac{Q}{m} \cdot \left(\frac{Z_q}{a}\right)^2 \cdot \lambda_u = 4.8 \cdot 10^{-6} \text{ H} \qquad (2.73)$$

III. *Leakage end-winding inductance*
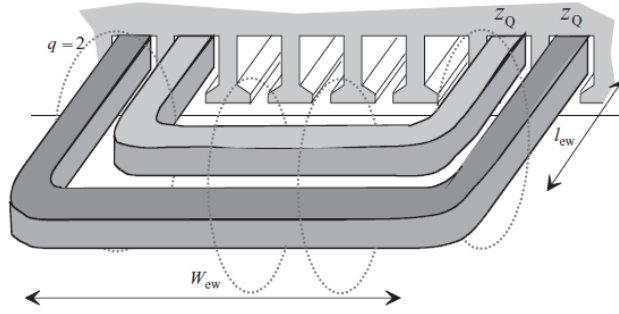
Figure 2.37: Reference for the end-winding leakage inductance

$l_{ew} = 0.02416 \, m$

$W_{ew} = 0.04832 \, m$

$\lambda_{lew} = 0.324$

$\lambda_{wew} = 0.215$

Where λ_{lew} and λ_{wew} are the permeance factor of the end winding, the values are tabulated for different combination of stator and rotor.

$$l_{end-winding} = 2 \cdot l_{ew} + W_{ew} \qquad (2.74)$$

$$l_w \cdot \lambda_w = 2 \cdot l_{ew} \cdot \lambda_{lew} + W_{ew} \cdot \lambda_{wew} = 0.026 \qquad (2.75)$$

$$L_w = \frac{Q}{m} \cdot q \cdot \left(\frac{Z_q}{a}\right)^2 \cdot \mu_0 \cdot l_w \cdot \lambda_w = 6.7 \cdot 10^{-5} \text{ H} \qquad (2.76)$$

2.7.3 Computation of the inductances by FEM

To compute the inductances by FEM, two different simulation have been performed. It is not necessary to use two different simulations, because the motor is isotropic, but in this way, it is checked that $L_d = L_q = L_m$.

The B_r of the magnets is set equal to 0. In one simulation the current is supplied in the d axis, in the other one in the q axis. The current is controlled via scenario, changing the value from 0 A to 7.35 A, with a step value of 0.5 A. For each value of current it is computed the fundamental magnetic flux density in the airgap.

The inductances in d and q axis for each current are computed by the following equation:

$$L_m = K_w \cdot N_s \cdot \frac{2}{\pi} \cdot \tau \cdot L \cdot \frac{B_{foundamental}}{i_q} \tag{2.77}$$

The fundamental of the magnetic flux density in the airgap is computed by FLUX.

Table 2.8: Values of the magnetic flux density in the airgap for different stator current

I	B_d	B_q	L_d	L_q
0	0	0	0	0
0.5	4.00E-03	4.00E-03	7.95E-05	7.95E-05
1	8.00E-03	8.00E-03	7.95E-05	7.95E-05
1.5	1.20E-02	1.20E-02	7.95E-05	7.95E-05
2	1.60E-02	1.60E-02	7.95E-05	7.95E-05
2.5	2E-02	2E-02	7.96E-05	7.96E-05
3	2.4E-02	2.4E-02	7.96E-05	7.96E-05
3.5	2.8E-02	2.8E-02	7.96E-05	7.96E-05
4	3.2E-02	3.2E-02	7.96E-05	7.96E-05
4.5	3.6E-02	3.6E-02	7.96E-05	7.96E-05
5	4E-02	4E-02	7.97E-05	7.97E-05
5.5	4.4E-02	4.4E-02	7.97E-05	7.97E-05
6	4.81E-02	4.81E-02	7.97E-05	7.97E-05
6.5	5.21E-02	5.21E-02	7.97E-05	7.97E-05
7	5.61E-02	5.61E-02	7.97E-05	7.97E-05

By the average of the different inductance values obtained for each current, it is obtained the value of the magnetization inductance:

$$L_m = 7.96 \cdot 10^{-5} \text{ H} \tag{2.78}$$

Finally, the L_s is computed as follows:

$$L_s = L_m + L_{leakage} = 7.96 \cdot 10^{-5} + 4.8 \cdot 10^{-6} + 6.7 \cdot 10^{-5} = 1.5 \cdot 10^{-4} \tag{2.79}$$

The L_s computed by hand is closer to the measured one (paragraph 2.6).

Chapter 3

Losses

3.1 Iron losses

3.1.1 Introduction

The losses are an important aspect of electrical machine. There is a difference between simulated and measured iron losses; to match them, some "loss correction factors" are introduced.

In literature there are several iron loss calculation models:

- Steinmetz equation
- Loss separation into hysteresis and eddy current losses (Bertotti)
- Mathematical hysteresis models (Loss Surface Model)

I. Steinmetz equation

It is an empirical equation used when a magnetic material is subject to a sinusoidal magnetic flux.

$$P = k \cdot f^a \cdot B^b \qquad\qquad (3.1)$$

Where P is the power loss in mW/cm^3, f is the frequency in KHz, B is the peak magnetic flux density, k, a and b are the Steinmetz coefficient, computed empirically. Iron losses are divided into hysteresis losses and eddy current losses. If are considered only the hysteresis losses, a is 1 and b is 2, but to take into account of the non-linearity, a is between 1 and 2 and b is between 2 and 3.

If the magnetic flux is not sinusoidal, it can be used the general equation:

$$P = \frac{1}{T} \cdot k_i \cdot | \left(\frac{dB}{dT}\right) |^a \cdot (\Delta B^{b-a}) \tag{3.2}$$

Where ΔB is the peak-to-peak magnetic flux density, and k_i is defined in the equation (3.3).

$$k_i = \frac{k}{(2\pi)^{a-1} \cdot \int_0^{2\pi} | \cos \theta |^a \cdot 2^{b-a} \cdot d\theta} \tag{3.3}$$

The parameters a and b are the same previously defined.

II. *Iron loss separation models*

Iron losses can be divided into static hysteresis losses, dynamic eddy current losses and excess losses. The equation of p_{Fe} is correct for NiFe alloys, but not for SiFe alloys, so, an empirical correction factor C_{exc} (excess loss factor) is introduced.

$$p_{Fe} = k_1 \cdot \hat{B}^{\alpha_1} \cdot f + k_2 \cdot f^{\alpha_2} \cdot \hat{B}^{\alpha_2} + k_3 \cdot f^{\alpha_3} \cdot \hat{B}^{\alpha_3} \tag{3.4}$$

Where k_1 is the coefficient of hysteresis losses, k_2 is the coefficient of eddy current losses, k_3 is the coefficient of losses in excess, α_1 is the exponent of the classical losses, α_2 is the exponent of the eddy current losses and α_3 is the exponent of the excess losses, f is the frequency, and $\hat{B}$ is the peak value of the magnetic flux density.

K_3 is described using the Bertotti's statistical model:

$$C_{exc} = \sqrt{S \cdot V_0 \cdot \sigma \cdot G} \tag{3.5}$$

Where S is the cross sectional area of the lamination sample, $G = 0.136$ is a dimensionless coefficient of the eddy current damping, σ is the electric conductivity of the lamination, V_0 is the statistical distribution of the local coercive fields.

The model is correct only if the skin effect is negligible.

III. *Loss Surface Model*

Iron losses are proportional to the inner area B-H-hysteresis loop.

The loss surface model is a hysteresis model that take into account of the dynamic phenomena. It is assumed that knowing the time variation of the flux density and its excitation frequency, the material behavior is defined. The applied field on the surface is linked to the average flux density in the section.

The total magnetic field is represented by the sum of the static and dynamic fields.

$$H(B, dB/dt) = H_{stat}(B, history) + H_{dyn}(B, dB/dt) \qquad (3.6)$$

The iron loss can be obtained integrating the total magnetic field on the considered volume region

$$\int_v H \, dB \qquad (3.7)$$

B is the magnetic flux density and dB/dt its rate of change. The model connects the magnetic field H on the sheet surface with the flux density B in the thickness of sheet. The static part is modeled by the scalar hysteresis model, the dynamic part is modeled by two analytical equations describing the low and high values of the flux density derivatives after substracting H_{stat}.

3.1.2 Iron losses computation by FEM with sinusoidal supply

The stator iron losses are computed by FEM using the two different method: Bertotti and Loss Surface Method. The computation of the iron losses has been performed in no-load and load conditions. In the load conditions it is assumed a temperature of 90°.

I. *Bertotti Method*

In the FLUX simulation it is necessary to put the Bertotti coefficients directly in the material properties, to compute the iron losses.

The input parameters are the electrical conductivity, 1923077 1/(Ωm), the thickness of the iron sheet, equal to 3.5E-4 m, the density of the material, equal to 7650 kg/m^3, the

frequency, equal to 1000 Hz and the volume, 1.31E-04kg. The values of the iron loss curve provided by the material in function of the magnetic flux density at 1000 Hz are reported in Table 3.1.

Table 3.1: Iron loss curve provided by the datasheet for 1000 Hz

B (T)	Measured Loss (W/kg)
0.1	0.99
0.2	3.67
0.3	7.63
0.4	12.70
0.5	18.90
0.6	26.40
0.7	35.40
0.8	46.00
0.9	58.40
1	73.00
1.1	90.10

For each value of B, are computed the hysteresis losses, the classical losses and the excess losses, using the equations (3.8), (3.9) and (3.10) respectively. Then, Bertotti modified losses are computed as sum of hysteresis losses, classical losses and excess losses. Consequently, using a statistical tool on Excel, are obtained the Bertotti coefficients that minimize the square root of the difference between the values of the Measured Loss (Table 3.1) and Bertotti modified (Table 3.2). All the results are reported in Table 3.2.

In this way, the curve of Bertotti losses is closer to the curve of the measured losses provided by the datasheet, as it is shown in Figure 3.1.

$$Hysteresis\ losses = \ k_1 \cdot B(T) \cdot \alpha_1 \cdot f \cdot V \qquad (3.8)$$

$$Classical\ losses = k_2 \cdot B(T) \cdot (\alpha_2)^2 \cdot f \cdot V \qquad (3.9)$$

$$Excess\ losses = \ k_3 \cdot B(T) \cdot (\alpha_3)^2 \cdot f \cdot V \qquad (3.10)$$

Where k_1, k_2, k_3, α_1, α_2, α_3 are the Bertotti's coefficients previously defined, f is the frequency and V is the volume.

Table 3.2: Computation of the losses

| hysteresis losses	classical losses	excess losses	Bertotti modified (W/kg)	square of difference	
0.73	0.00062	0.013	**0.74**	0.061	7.05
2.9	0.0025	0.037	**2.95**	0.512	6.99
6.56	0.0056	0.069	**6.63**	0.997	6.48
11.66	0.0099	0.106	**11.77**	0.86	5.48
18.21	0.0156	0.15	**18.38**	0.27	4.62
26.23	0.022	0.19	**26.44**	0.002	4.345
35.7	0.031	0.25	**35.97**	0.33	4.343
46.63	0.04	0.3	**46.97**	0.93	4.013
59.01	0.05	0.358	**59.42**	1.04	3.078
72.85	0.062	0.412	**73.34**	0.113	2.04
88.15	0.075	0.483	**88.71**	1.92	1.92
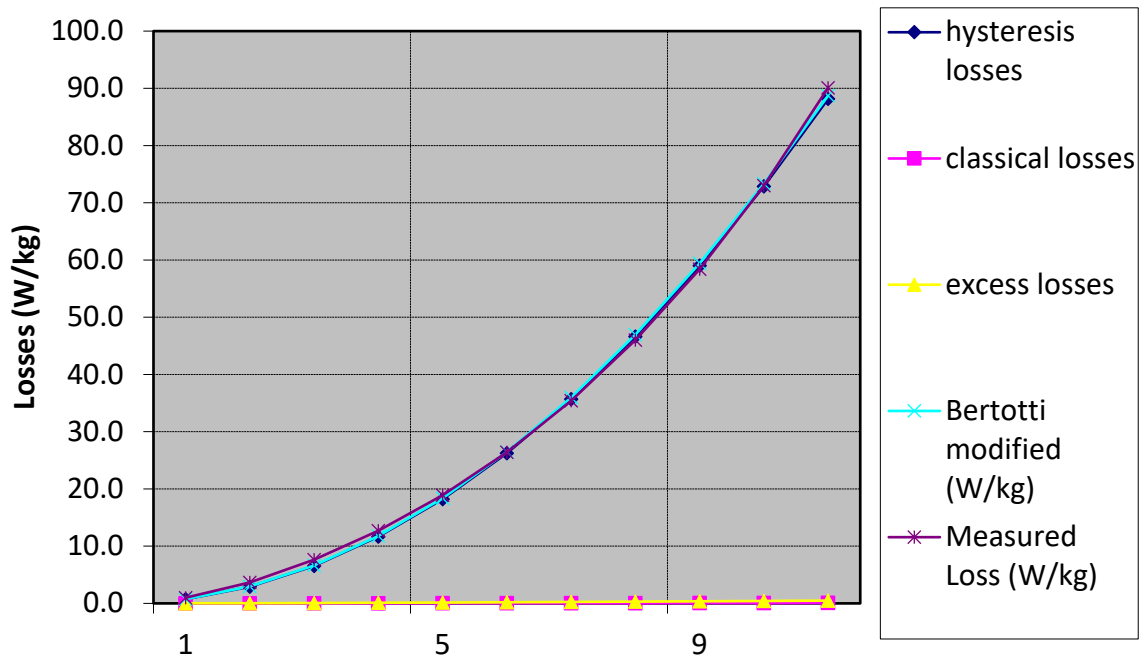
Figure 3.1: Losses trend

Consequently, the computed Bertotti coefficients are:

k_1 = 557.34

k_2 = 0.00048

k_3 = 0.1

α_1 = 2

α_2 = 2

α_3 = 1.5

II. *Loss Surface Method*

The Loss Surface Method is directly effectuated by FLUX.

Are reported the results for the no-load simulation obtained with the two different computation. In no load conditions the iron losses are 5.51 W using Bertotti and 7.34 W using the Loss Surface Method. In load conditions the iron losses are 4.86 W using Bertotti and 6.41 W using the Loss Surface Method. The results are reported in Figure 3.2, Figure 3.3, 3.4 and 3.5. As it is possible to see, the iron losses in no-load conditions are higher than the iron losses in load conditions. It is acceptable because the magnetic flux density in no load conditions is higher than the one in load conditions, as it shown in Figure 3.6 and 3.7.
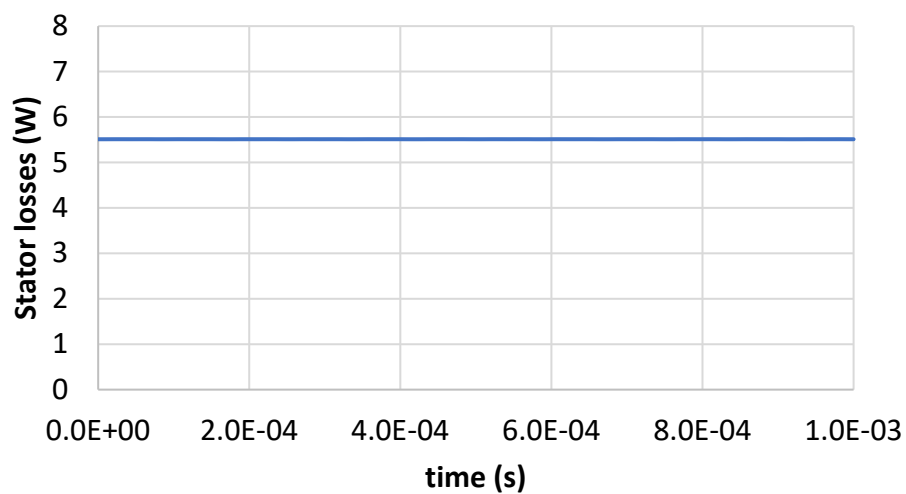

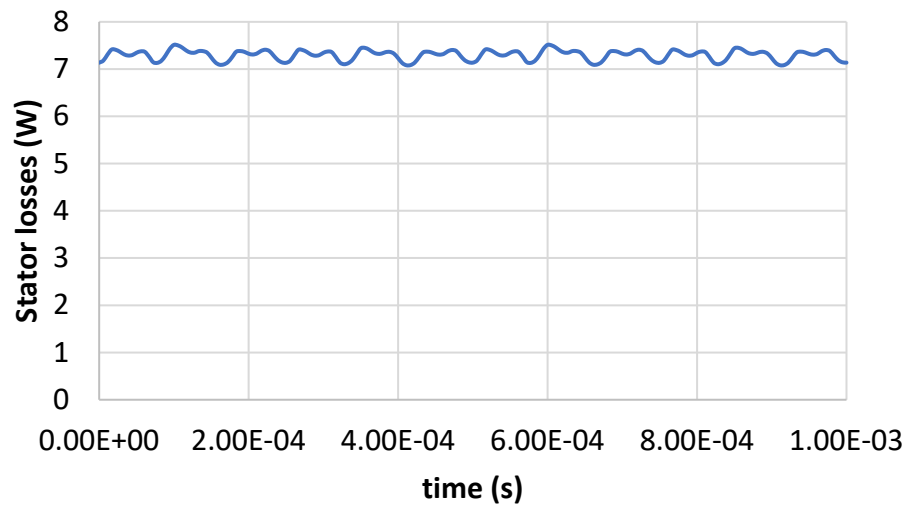*Figure 3.2: Stator losses using Bertotti method in no-load conditions*

Figure 3.3: Stator losses using Loss Surface Method in no-load conditions
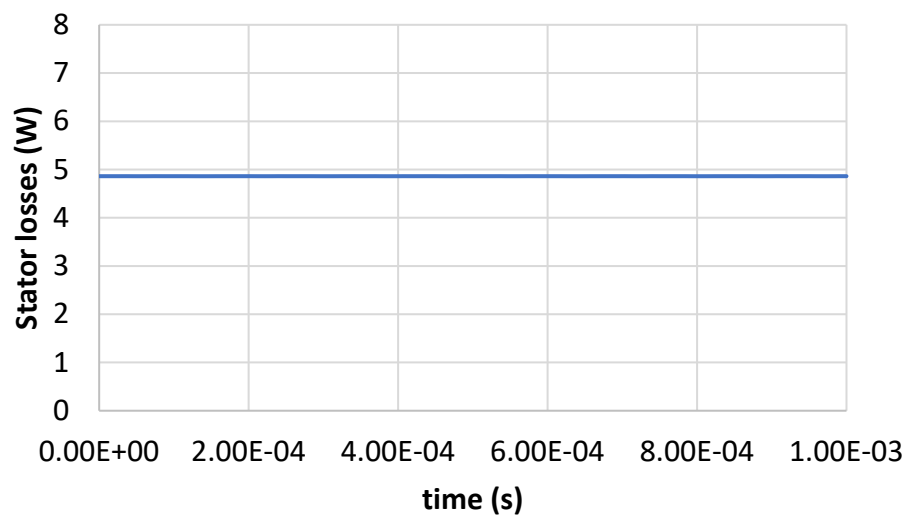

Figure 3.4: Stator Losses using Bertotti Method in load conditions
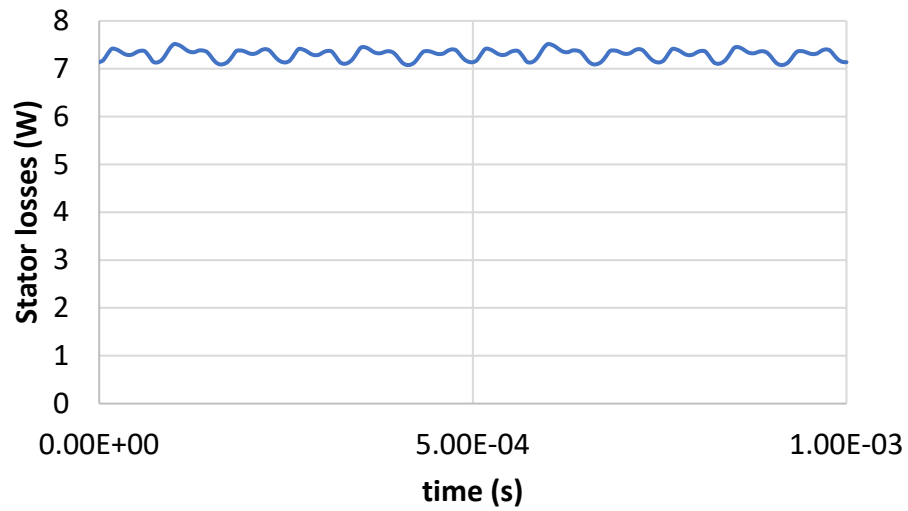
Figure 3.5: Stator Losses using the Loss Surface Method in load conditions

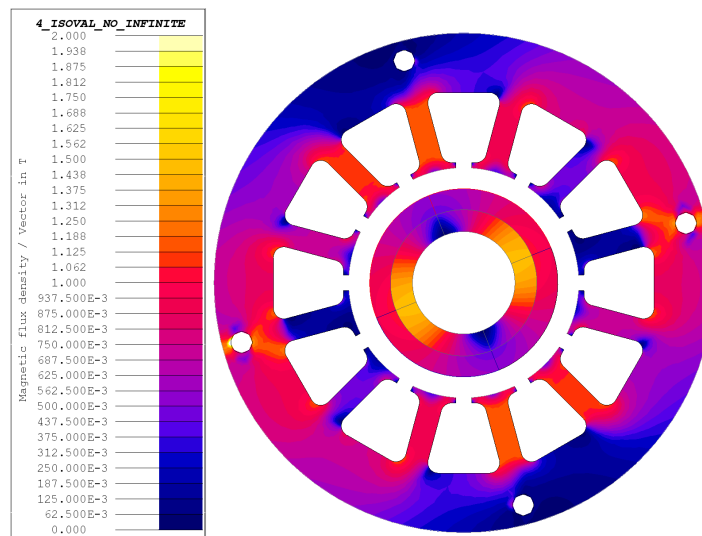The Loss Surface Method is considered more accurate.

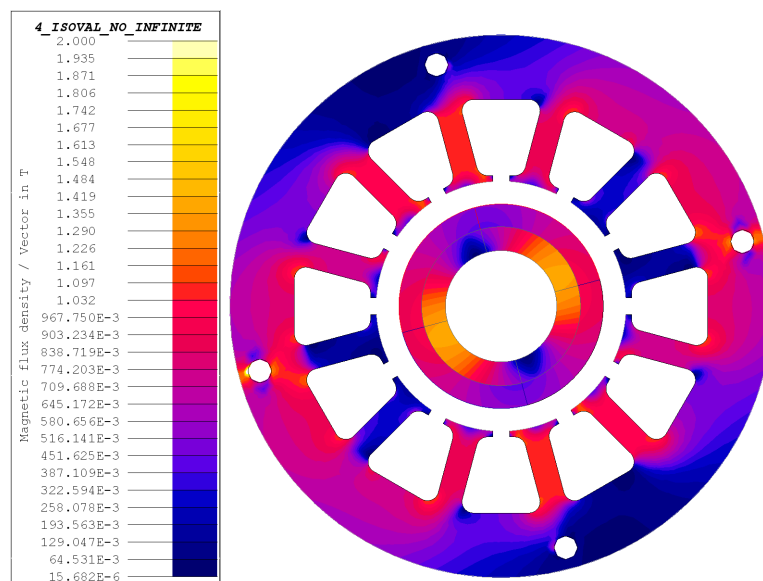*Figure 3.6: Magnetic flux density in no-load conditions*

Figure 3.7: Magnetic flux density in load conditions

3.2 Losses in the Permanent Magnet and in the Sleeve

To compute the losses in the PM and in the carbon fiber sleeve, it is necessary to create another electrical equivalent circuit, reported in the Figure 3.8.
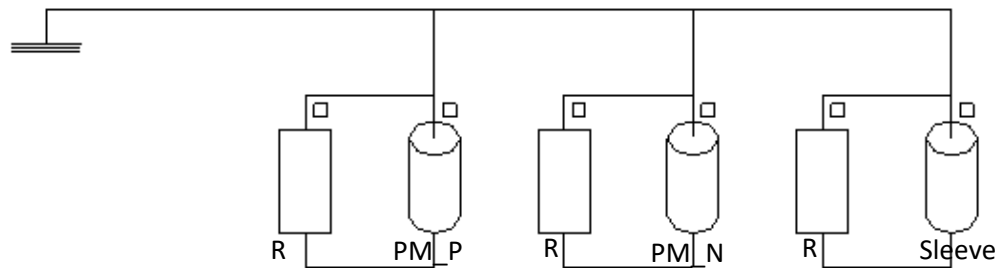

Figure 3.8: Equivalent circuit for the computation of the losses in the sleeve and in the permanent magnets

After the creation of the circuit, the three solid conductors are assigned at the face region, one is assigned to the sleeve and the other one to the permanent magnets. The resistances in parallel with the solid conductors are big (10^9 Ω). Finishing the circuit, it is possible to compute the losses in the carbon fiber sleeve and in the permanent magnets as Joule losses in the solid conductors. The resistivity of the sleeve is 3.0303E-4 Ωm and the one of the magnets is 1.5E-6 Ωm, the values are reported in the datasheet of the materials. The losses have been computed in no-load and load conditions (in load conditions is assumed a temperature of 90°C).

In no load conditions the sleeve losses are 3.97 mW, while the permanent magnets losses are 5.68 mW, as shown respectively in Figure 3.9 and 3.10. In load conditions the sleeve losses are 6.9 mW and the permanent magnets losses are 18.8 mW, as reported in Figure 3.11 and 3.12.
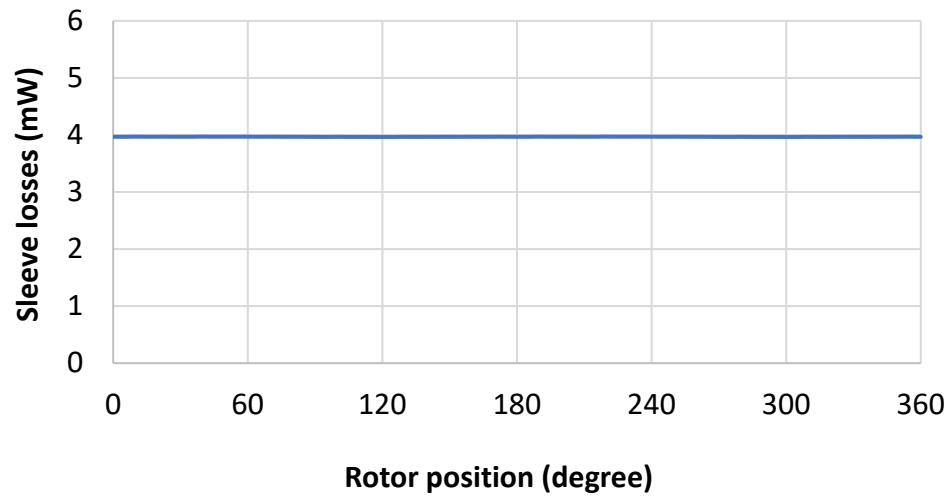
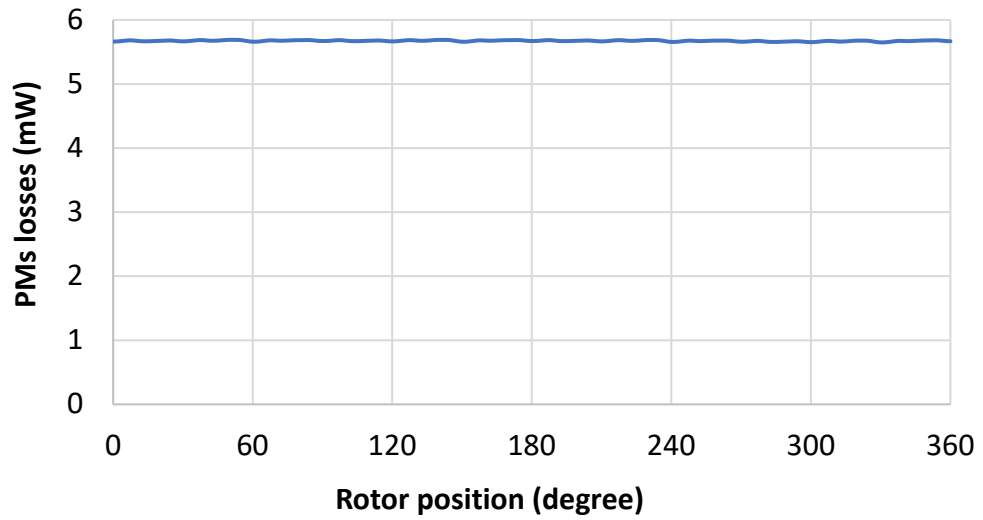*Figure 3.9: Joule losses in the sleeve in no-load conditions*

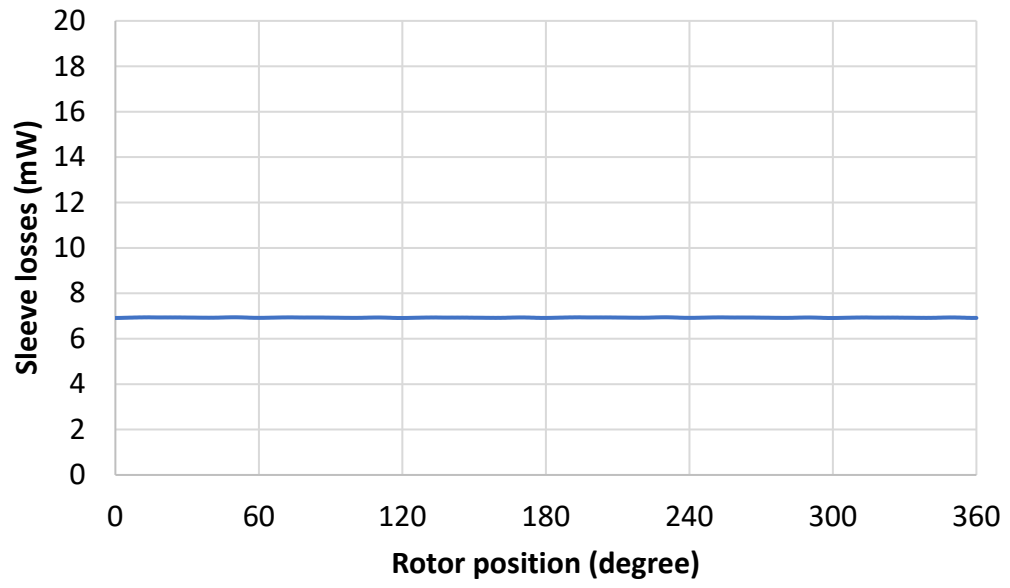*Figure 3.10: Joule losses in the permanent magnets in no-load conditions*

Figure 3.11: Joule losses in the sleeve in load conditions
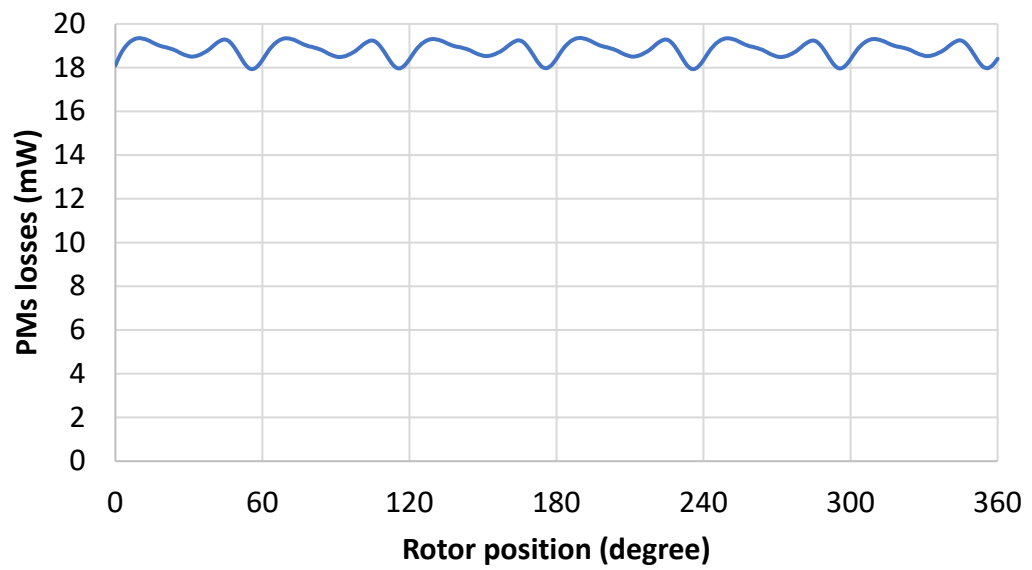
Figure 3.12: Joule losses in the permanent magnets in load conditions

3.3 Copper Losses

Copper losses are an unwanted energy transfer in term of heat, in the conductors. The copper losses are expressed with the Joule low:

$$P = 3 \cdot R \cdot I^2 \tag{3.11}$$

The resistance at the working temperature (90°C), is computed in the following equation:

$$R = R_0 \cdot (1 + \alpha \cdot (T - T_0) = 0.1325 \left(1 + 0.00393 \left(90 - 20\right)\right) = 0.17 \, \Omega \tag{3.12}$$

Where R_0 is the resistance at 20°C (0.1325 Ω), α is the thermal coefficient, T is the working temperature (90°C) and T_0 is 20°C.

Considering the resistance value and the current of 5.2 A$_{rms}$ the copper losses are:

$$P = 13.8 \, W \tag{3.13}$$

3.4 Iron losses with PWM or PAM supply

3.4.1 Introduction to different modulations

There are different modulation techniques, used to carry the information through signals, changing some of its characteristic, such as amplitude, frequency, width, ecc.

The modulation happens with the comparison of the modulation signal with a carrier signal, that has constant amplitude and frequency.
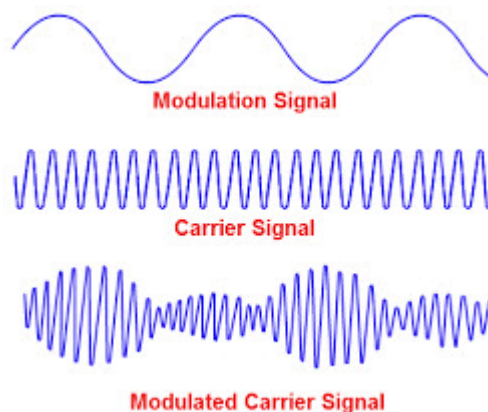

Figure 3.13: Modulation signal, Carrier signal, Modulated signal

The modulation can be continuous wave modulation, or pulse modulation.

In the continuous wave modulation, the characteristics that can be modified are:

- Amplitude (*Amplitude modulation*)
- Phase (*Phase modulation*)
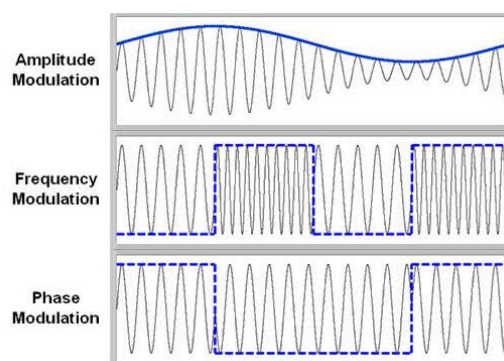- Frequency (*Frequency modulation*)

Figure 3.14: Different type of modulation

The pulse modulation can be divided into digital or analog modulation.

In the analog pulse modulation, the characteristic that can be modified are:

- Width (*Pulse Width Modulation*)

- Amplitude (*Pulse Amplitude Modulation*)

- Position (*Pulse Position Modulation*)

The digital modulation can be divided in *Delta Modulation* and *Pulse Code Modulation*.

Our interest is directing towards two different pulse modulation technique (PWM and PAM) and how they influence the stator iron losses.

Pulse Amplitude Modulation

In the PAM, the amplitude of each pulse is given by the instantaneous amplitude of the modulation signal. The signal is sampled at regular intervals, T_s.
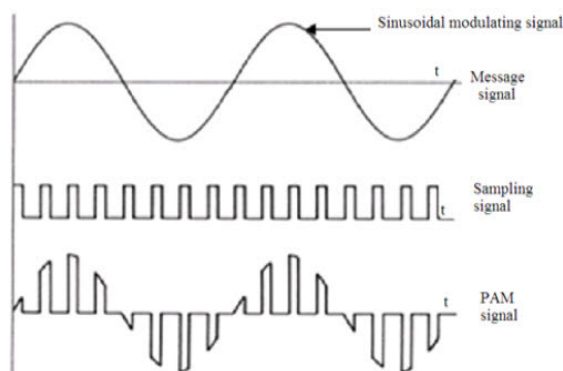

Figure 3.15: Pulse Amplitude Modulation

There are two different sampling tecqniques:

- *Flat Top PAM*: the amplitude of each pulse is given by the amplitude in the sampling time and cannot be modified during the sampling time (sample and hold), consequently, the top of the pulse is flat.

Figure 3.16: Flat Top Pulse Amplitude Modulation

- *Natural PAM*: the amplitude of each pulse follows the amplitude of the modulating signal instant by instant
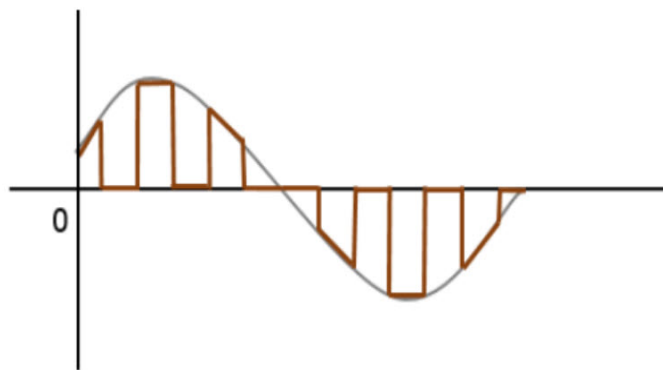
Figure 3.17: Natural Pulse Amplitude Modulation

Pulse Width Modulation

The width of the pulse varies proportional to the instantaneous amplitude of the message signal, while the amplitude remains constant, so it is possible to obtain a desired value of amplitude.

There are three different type of pulse width modulation:

a) The leading edge is constant, while the trailing edge varies proportionally of the message signal

b) The trailing edge is constant, while the leading edge varies proportionally of the message signal

c) The center of the pulse is constant, while the trailing and the leading edges change.

70

Figure 3.18: Different type of Pulse width Modulation

3.4.2 Iron losses with PWM supply

It is important to consider the effect of the converter modulation on the machine losses, especially for high speed applications.

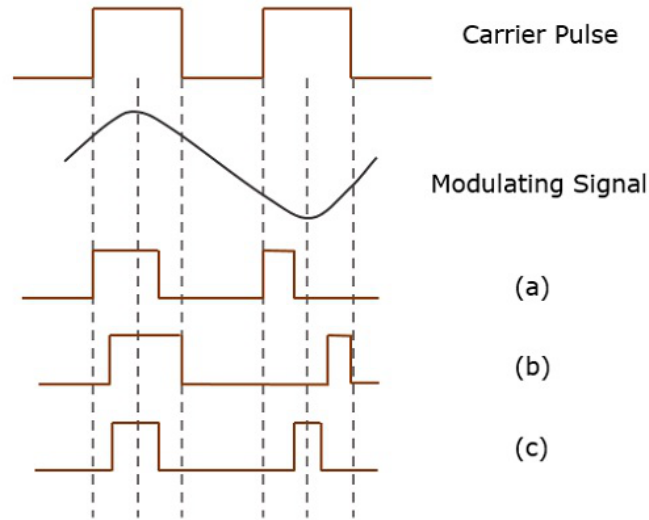In this section, the goal is to analyze the losses with PWM supply. It is acceptable to consider that the magnetic work conditions are not influenced by higher order flux density harmonic, under PWM supply. With this assumption it is possible to divide the period in small intervals and to consider in each of them a constant magnetic condition, defined by the instantaneous value of the fundamental flux density. In practice, in each time interval, a constant magnetic permeability (different from the others) is considered, assuming a linear condition. Then, in each interval, are calculated the power losses that come from the higher order harmonics; summing all the power losses and dividing by the number of intervals, it is possible to obtain the average power losses for each harmonic. The total power losses considering PWM supply are obtained summing the power losses that come from the fundamental harmonic and all the higher order harmonics. The results obtained by some measurements, show that it is possible to consider the trend of the iron losses as a polynomial equation:

$$k(B) = 1 + A_1 B + +A_2 B^2 + A_3 B^3 + A_4 B^4 \qquad (3.14)$$

Where *k (B)* is the relative iron loss increase factor, given by the ratio between the iron loss for the higher order harmonic with the dc-bias field and the one obtained without dc-bias field. The coefficients A_1, A_2, A_3, A_4 define the trend of *k(B),* are obtained by experimental measurements. *B* is the value of the fundamental flux density. Now the average value of *k(B)* must be computed. In general, it is possible to consider:

$$k_{AV} = 1 + \alpha_1 A_1 B_{max} + +\alpha_2 A_2 B_{max}^2 + \alpha_3 A_3 B_{max}^3 + \alpha_4 A_4 B_{max}^4 \qquad (3.15)$$

Where B_{max} is the maximum value of the flux density. The coefficients α_1, α_2, α_3 and α_4 approximate the trend of the flux density. If it is considered only the first harmonic, the computation can be limited to a quarter of the fundamental harmonic:

$$k_{AV} = \frac{4}{T} \int_0^{\frac{T}{4}} k(B) dt \qquad (3.16)$$

Where *k(B)* is valid only for the specified time instant. *T* is the period.

$$B(t) = B_{max} \sin(\omega t) \qquad (3.17)$$

Substituting (3.17) into (3.14), we obtain (3.15), with these coefficients:

$$\alpha_1 = \frac{2}{\pi}, \alpha_2 = \frac{1}{2}, \alpha_3 = \frac{4}{3\pi}, \alpha_4 = \frac{3}{8} \qquad (3.18)$$

Now it is possible to compute the iron losses with respect to the presence of the fundamental harmonic.

$$P_{iAC} = P_i k_{AV,i} \qquad (3.19)$$

$P_{i,AC}$ represents the power losses of the higher order harmonic with the fundamental one, P_i are the power losses of the higher order harmonic without the fundamental one, $k_{AV,I}$ is the coefficient representative of the iron loss increase.

Finally, the total iron losses with PWM supply, can be computed as follows:

$$P_{TOT} = P_1 + \sum_{i=m}^{n} P_i k_{AV,i} \qquad (3.20)$$

Where $k_{AV,I}$ is the average coefficient of the iron loss increase for the i-th harmonic, P_{TOT} represents the total iron loss with PWM supply, *m* is the number of the first harmonic in the flux density spectrum, n is the number of the last harmonic in the flux density spectrum, P_1

is the iron loss for the fundamental harmonic and P_i are the iron losses of the i-th harmonic, considering it with the other ones equal to zero.

In FLUX it is not possible to consider the presence of the converter, so, to remedy this problem, it is possible to power the motor, not with sinusoidal supply, but with the modulated current.

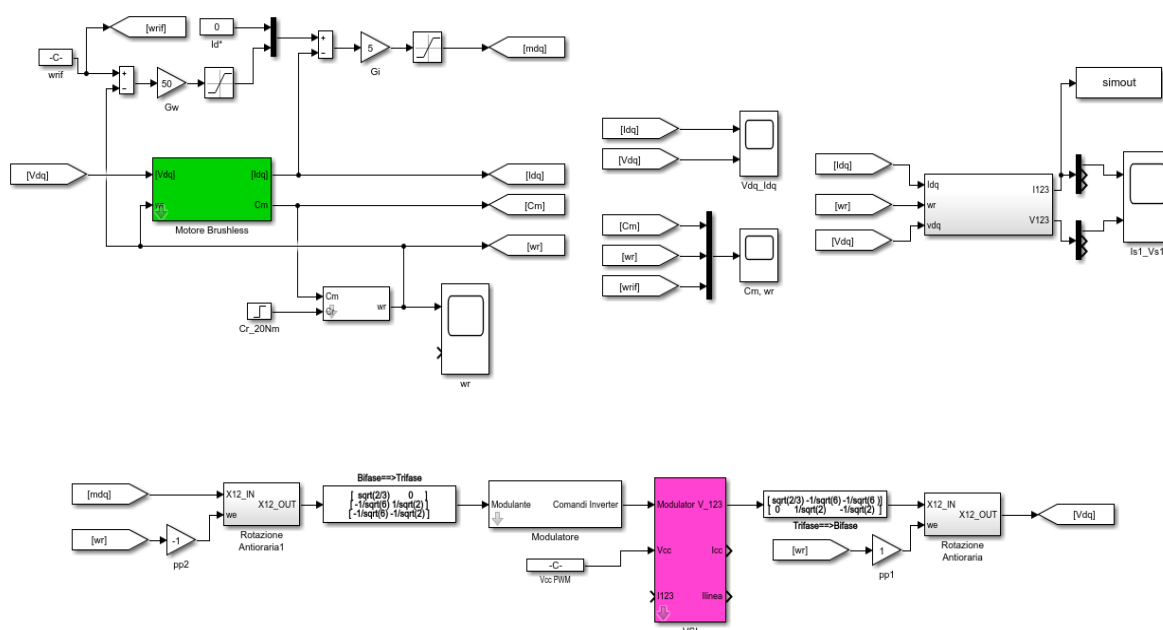In Simulink it is possible to simulate the converter and the motor with block diagrams.

Figure 3.19: Simulink blocks for PWM supply

In the mask of the motor are set all the main parameters (stator resistance, synchronous inductance, permanent magnets flux, pole pair). The reference value of the speed is equal to the rated value (60000 rpm). The switching frequency of the converter is set to 25000 Hz and the V_{bus} is 48 V. The problem is that in this condition the currents are practically sinusoidal.

It is possible to compute the iron losses considering a hysteresis control of the currents. The block on Simulink is reported in Figure 3.20. In this modulation technique the commutation of the switch is based on the comparison of the effective alternating current respect of a reference value, for example a hysteresis band. When the output current from the inverter crosses the limit of the hysteresis band placed around the desired range, takes place the

73

commutation. If the current exceeds the upper limits, the switch that was leading is open, while the other one is closed, in this way the current start to decrease until it reaches the lower limit of the band, causing the inverse switching. The frequency of the switching commutation depends on how fast the current passes from one limit to the other one, this frequency during a period of the current, does not remain constant, but varies with the current waveform.
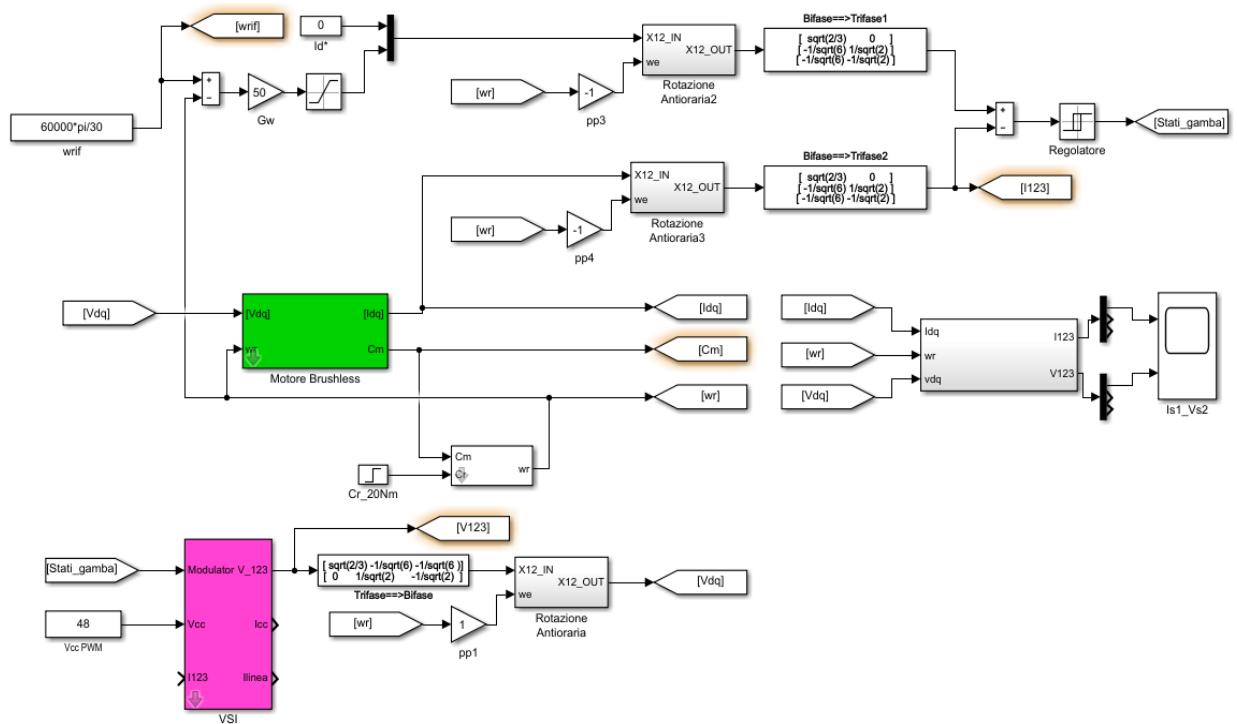

Figure 3.20: Simulink blocks considering hysteresis currents control

The parameters considered are the same specified for the simulation with PWM supply. After running the simulation, it is possible to export the values of the phase currents in function of the time in the workspace of Matlab. The currents-time trend is reported in Figure 3.21, considering only the last period. Then, are computed the values of the currents in function of the rotor position (Figure 3.22) to use in FLUX.
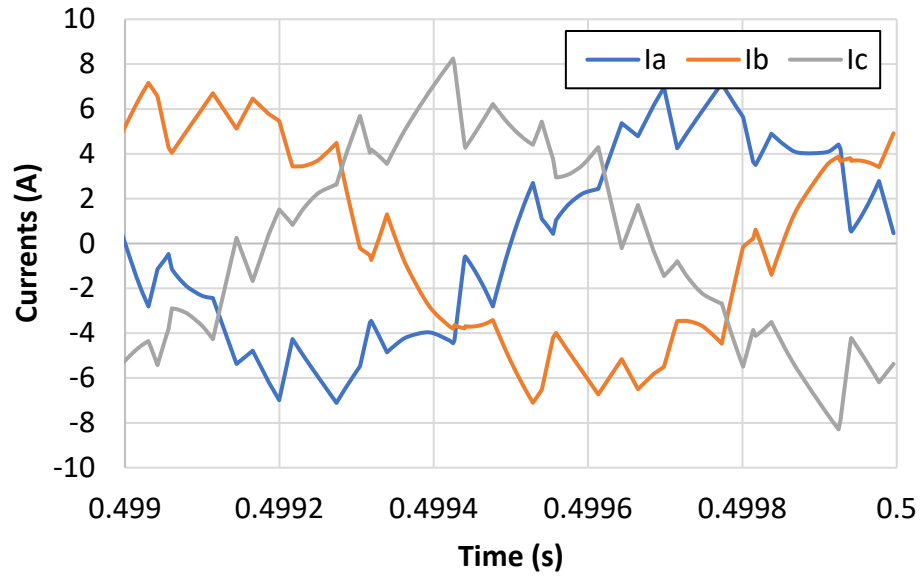
Figure 3.21: Phase current with hysteresis control in function of the time
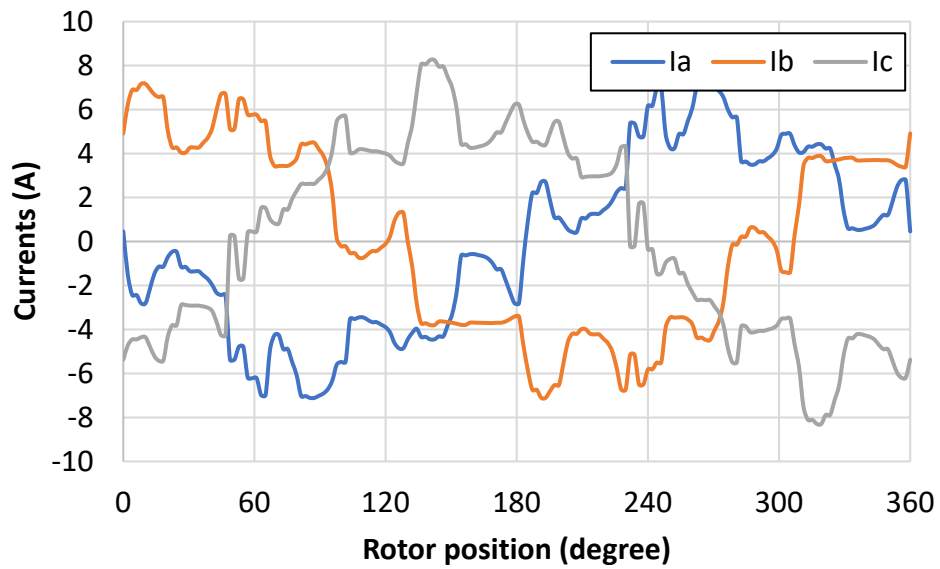

Figure 3.22: Phase current with hysteresis control in function of the rotor position

In the simulation at load conditions, are created the three parameters I_A, I_B and I_c, feeding the currents in the 1,2,3 frame without any transformation. It is possible to define the parameters as a table of value. The electric circuit is modified, considering three current

generators, for the three phase (Figure 3.23) and assigning for each of it the values previously created.

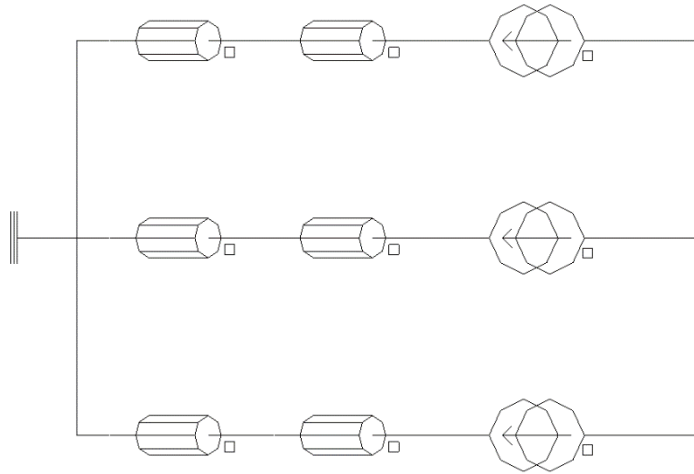*Figure 3.23: Electric circuit modified with three current generators*

The average iron losses using Bertotti, are 4.93 W (Figure 3.24), while the iron losses using the Loss Surface Method, are 7.39 W (Figure 3.25). The iron losses with hysteresis control of the currents are a little bit higher for the harmonic contents.
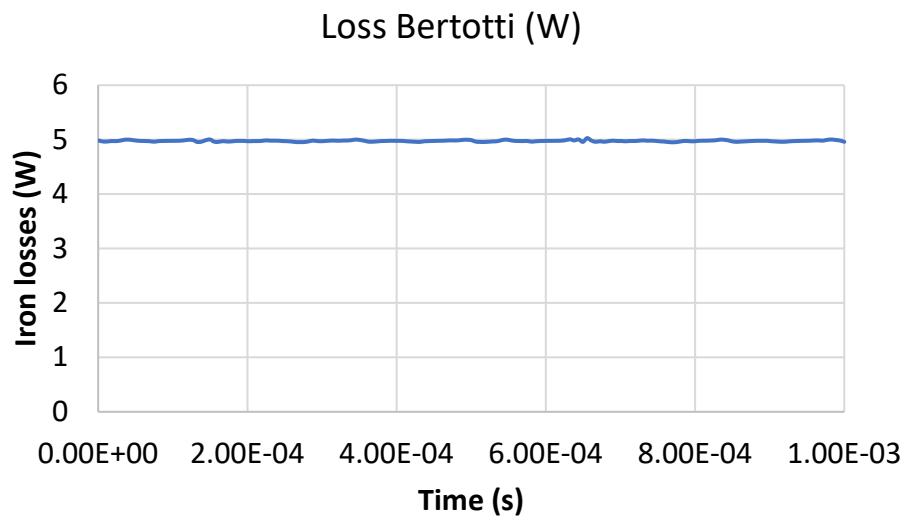

Figure 3.24: Iron losses with Bertotti method using hysteresis control of the currents
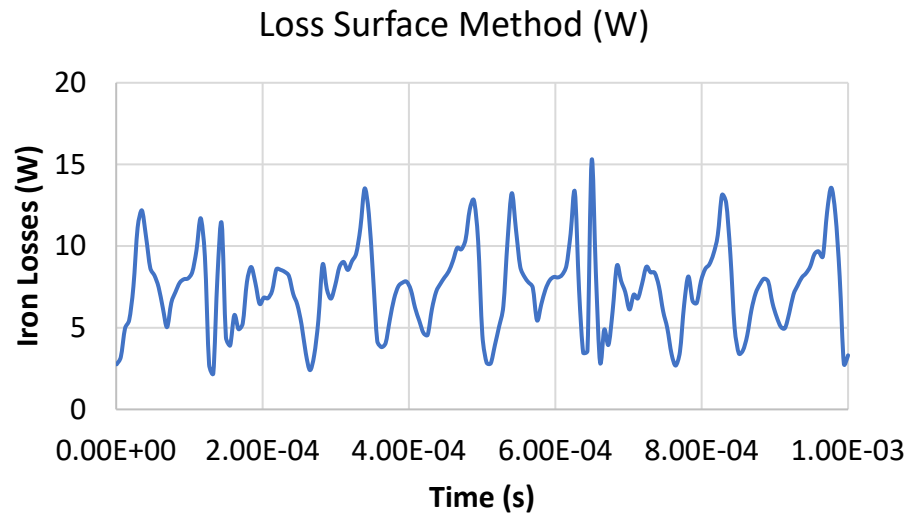
Figure 3.25: Iron losses with Loss Surface Method using hysteresis control of the currents

Chapter 4

New project solutions starting from the Agilent motor

The goal of this chapter is to analyze new design typologies starting from the Agilent motor, to obtain economic and performance advantages. The new solutions need to be designed and compared with the Agilent motor. Some of the new design choices are for example the use of a new stator with a double layer layout for the windings and the use of magnets in ferrite and not in neodymium. The double layer layout has clear advantages: simple construction of the heads, possibility of using the same coils, possibility of shortening the pitch. Furthermore, the use of ferrite instead of neodymium has obvious economic advantages. The new design is investigated in order to achieve the same performance of the start motor.

4.1 New stator with the old rotor

The new stator parameters are reported in the table 4.1.

Table 4.1: New stator parameters

New stator parameter	Value
Rated voltage	9.53 V
Rated torque	0.0127 Nm
Stator wire section	0.7952 mm^2
Wires in series per phase	40
Reference temperature	90°C
Outer diameter	48 mm
Inner diameter	25.1 mm

Active length	18 mm
End winding form coefficient	1.6760
Slot number	12
Number of pole	2
Phase resistance	0.08808 Ω (@90°C)

First of all, it is created the machine with the new stator in FLUX and the old rotor is inserted in it. Consequently, the new motor has a big airgap of 4 mm. The materials used for the motor parts are the same of the start motor. The parameters to modify in FLUX are the geometric parameters of the stator, the phase resistance, the wires in series per phase, the stator wire section and the active length.

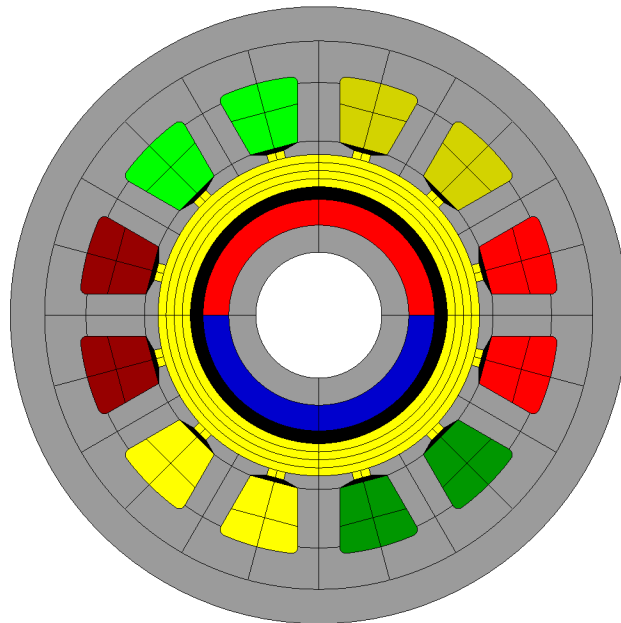The new machine is reported in Figure 4.1.

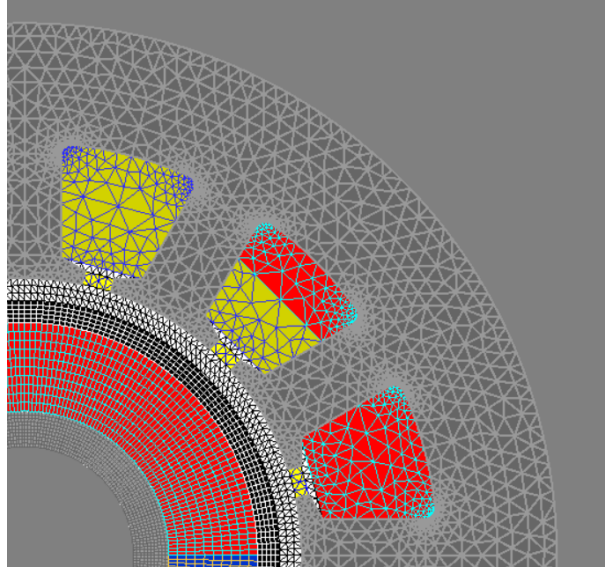*Figure 4.1: New machine with new stator and old rotor*

Figure 4.2: Meshed new machine

I. Simulation in no load conditions

For the simulation in no load conditions the temperature is 20°C. The peak value of the EMF is 33 V, as it is shown in Figure 4.3. In Figure 4.4 is reported the Fast Fourier Transform Analysis of the EMF.
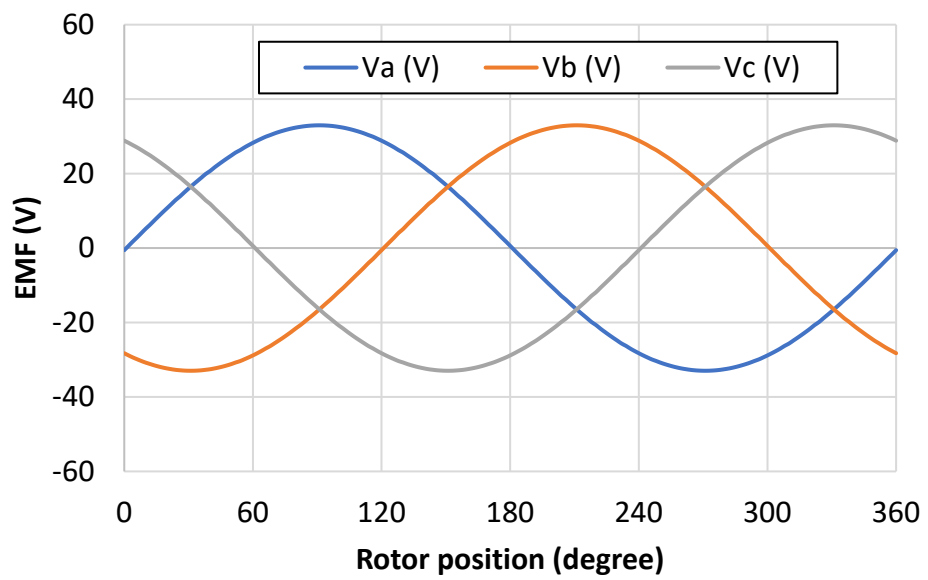
Figure 4.3: EMF in no load conditions
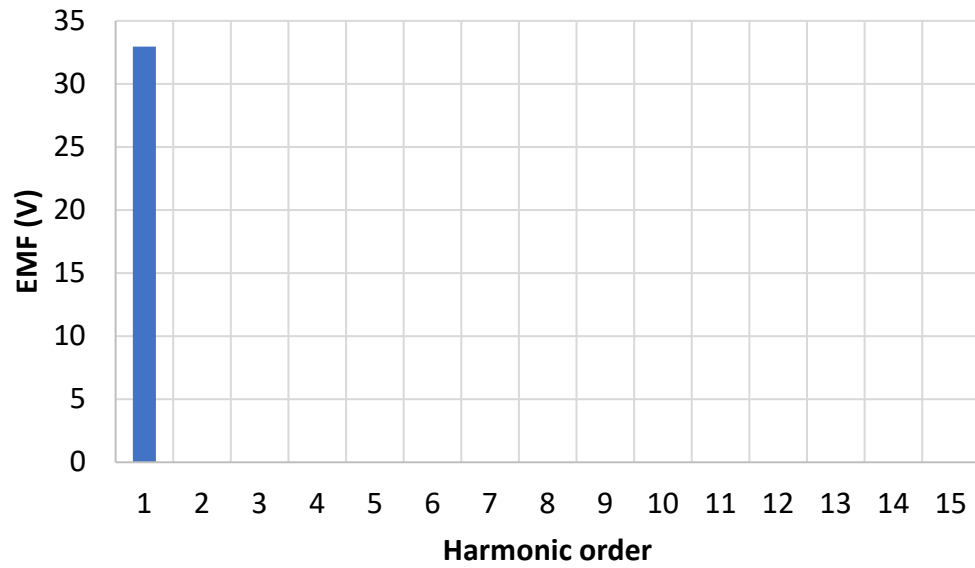
Figure 4.4: FFT of the EMF in no load conditions

II. Simulation in load conditions

A temperature of 90°C must be considered and it must be taken into account in the model, as seen previously. After checking that the phase current and the phase voltage are in phase, it is possible to continue. In Figure 4.5 it is reported the torque trend, the average value is 53.3 mNm. In Figure 4.6 is reported the FFT.
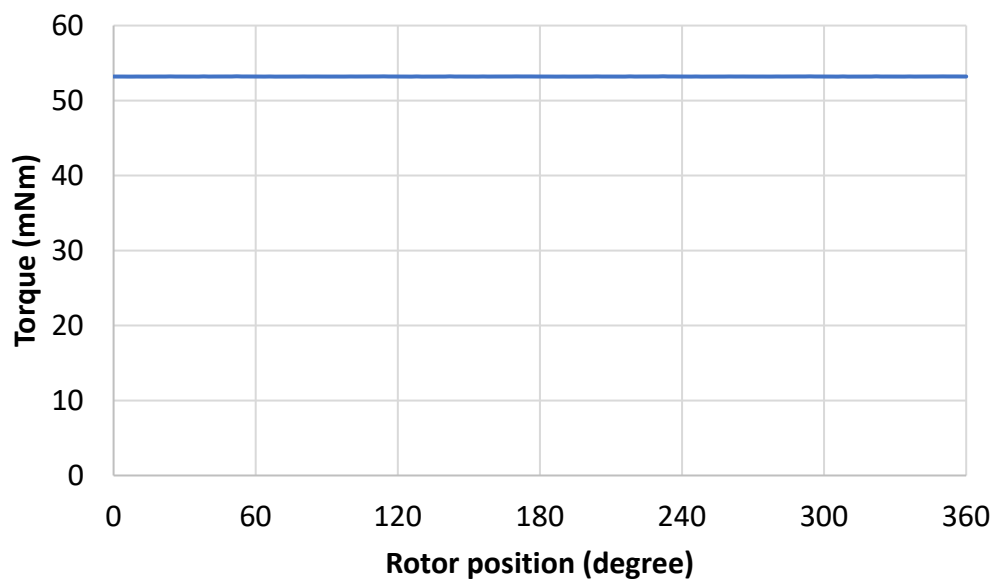
Figure 4.5: Torque trend in load conditions
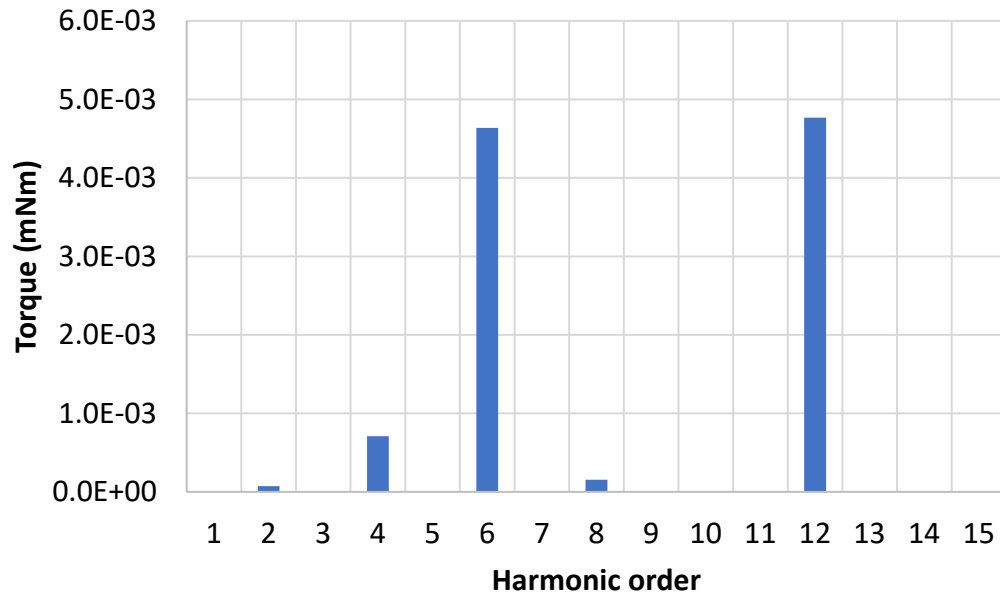
Figure 4.6: FFT of the torque in load conditions

The rated voltage of the inductance motor is 9.53 V (13.5 V as peak value). To obtain the rated voltage, the motor winding must be rewound.

$$Z = \frac{40 \cdot 13.5}{33} = 16 \tag{4.1}$$

The results with the new number of conductors in series per phase are reported.

I. Simulation in no load conditions

The peak value of the EMF is 13.2 V, closer to the rated one. In Figure 4.7 is reported the EMF trend and in Figure 4.8 there is the FFT analysis of the EMF.
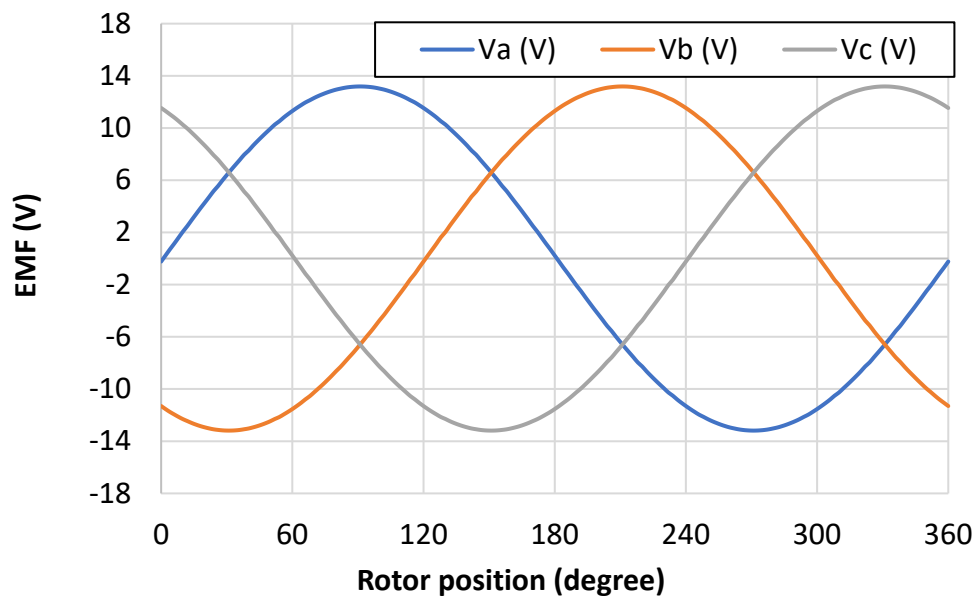
Figure 4.7: EMF in no load conditions with 16 conductors in series per phase
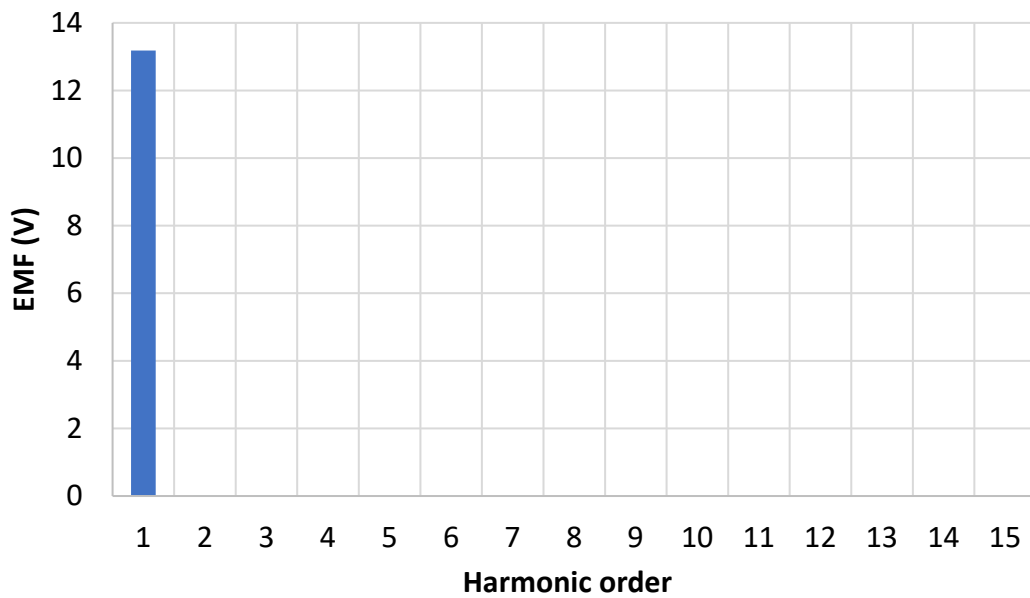
Figure 4.8: FFT of the EMF in no load conditions with 16 conductors in series per phase

II. Simulation in load conditions

The temperature in load conditions is 90°C. The torque trend is reported in Figure 4.9, the average value is 21.3 mNm and the torque ripple is very small, as it is shown in the FFT of the torque, in Figure 4.10.

Figure 4.9: Torque with 16 conductors in series per phase

Figure 4.10: FFT of the torque with 16 conductors in series per phase

4.2 New stator with adapted new rotor

The next step is to adapt the rotor to obtain a rated airgap of 1 mm. Another request of the company is to use permanent magnets in Ferrimax 30BH (C8), currently used for the production of vacuum pumps, with a bus at 24 Vdc. The material characteristics are reported in Table 4.2.

Table 4.2: Characteristic of Ferrimax 30BH (C8)

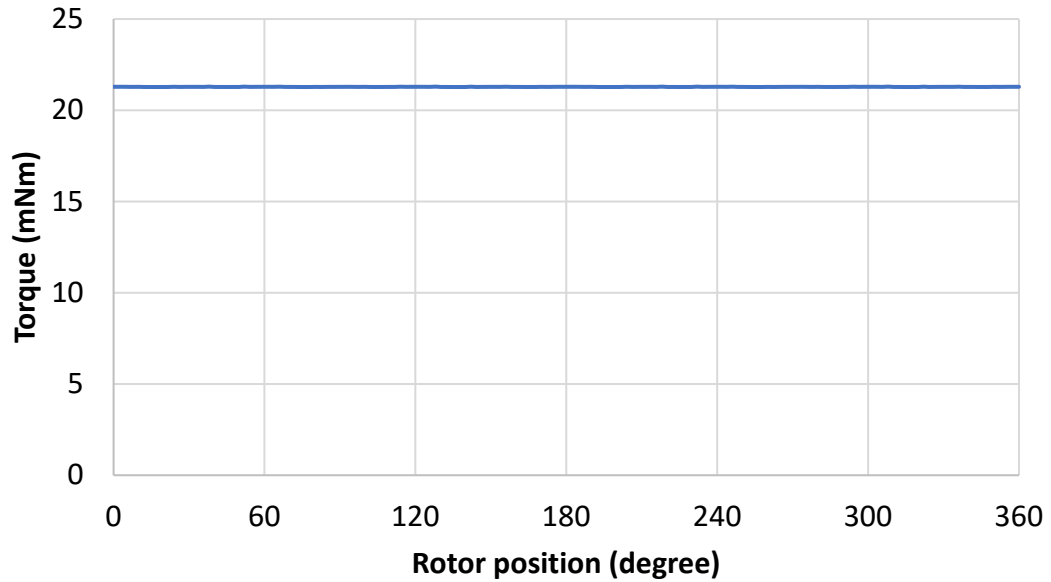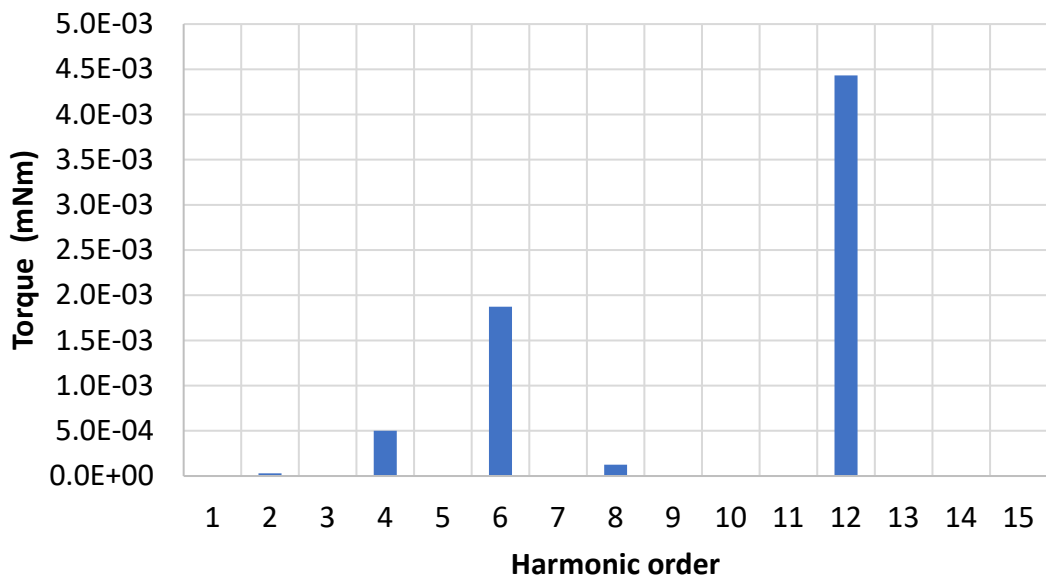| Br (mT)	HcJ (KA/m)	(BH)max (KJ/m3)	Thermal coefficient	Relative permeability (H/m)	Resistivity (µΩm)
380-400	230-250	27-31	-0.2%/°C	1.7	1.56

For the new material of permanent magnets B_r is 0.39 T, μ_r is 1.7 H/m, the thermal coefficient is -0.2% and the resistivity is 1.01 µΩm. In the neodymium magnets previously used, Br was 1.05 T, μ_r was 1.05 H/m, the resistivity was 1.56 µΩm and the thermal coefficient was -0.115%. The winding layout is the one of the Jarvis stator, a double layer with 40 conductors in series per phase and a reduced pitch of 1 slot. The thickness of the permanent magnet and the rotor yoke must be modified.

Three different configurations (reported in Figure 4.11) have been implemented in FLUX to check which one is the optimal solution to obtain the rated voltage of 13.5 V (peak value) and a torque of 20-22 mNm.
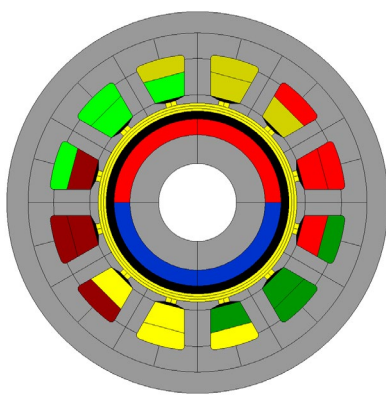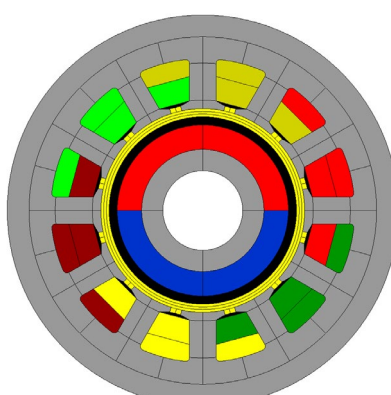
Figure 4.11 a)   *Figure 4.11 b)*   *Figure 4.11 c)*
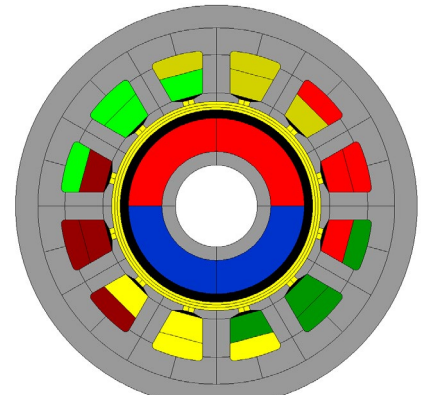
Configurations with different PMs thickness

As previously seen, the phase voltage and the phase current must be in phase, it means that all the current is supplied in the q axis and the torque is the maximum value.
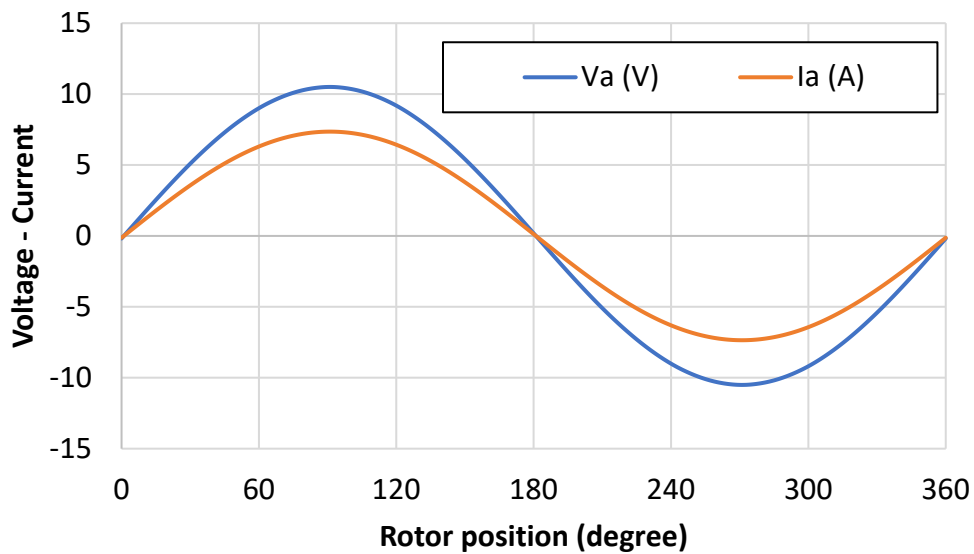
Figure 4.12: Phase voltage and phase current

4.2.1 Simulation in no-load conditions

- EMF

In the no-load conditions the working temperature is 20 degree. For the Ferrimax permanent magnets, B_r is equal 0.39 T and μ_r is equal 1.7 H/m. Considering a permanent magnets thickness equal 2 mm, the peak value of the phase voltage is 7.2 V, for a thickness of 3 mm, the peak value of the phase voltage is 9.12 V and finally, considering a thickness of 4 mm, the peak value of the voltage is 10.5 V. The EMF waveforms are reported in Figure 4.13 while the FFT Analysis are reported in Figure 4.14.
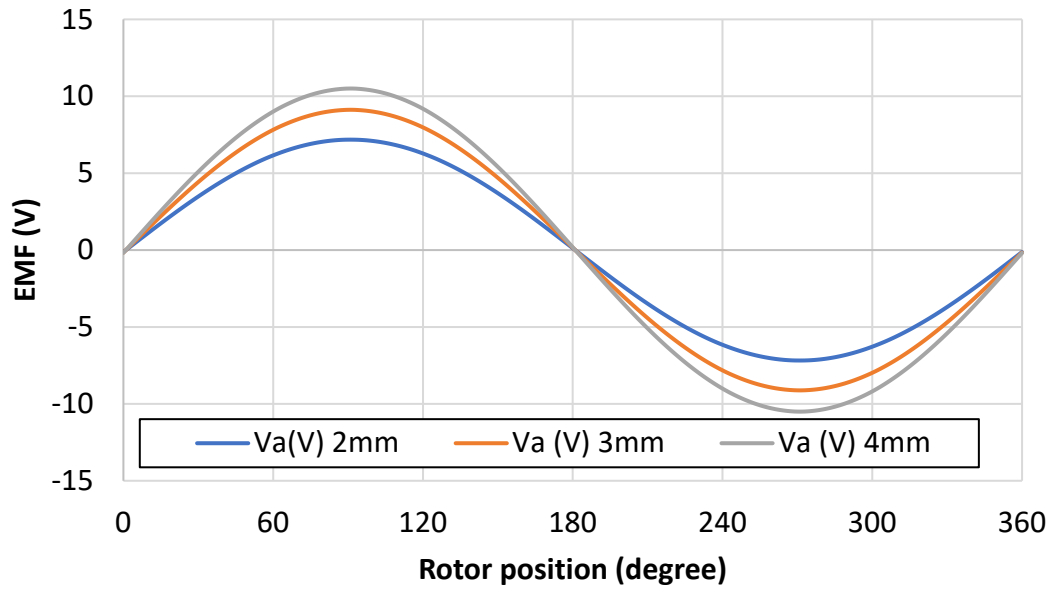
Figure 4.13: Phase voltage for the three different permanent magnets thickness

Figure 4.14: FFT of the phase voltage for the three different permanent magnets thickness

- Losses

The iron losses have been evaluated with Bertotti and Loss Surface Method. The iron losses using Bertotti are 0.93 W, 1.49 W and 1.96 W respectively for a thickness of the permanent

magnets of 2 mm, 3 mm and 4 mm. The results are reported in figure 4.15. The iron losses using the Loss Surface Method are 1.28 W, 1.97 W and 2.56 W respectively for a thickness of the permanent magnets of 2 mm, 3 mm and 4 mm. The results are reported in figure 4.16.
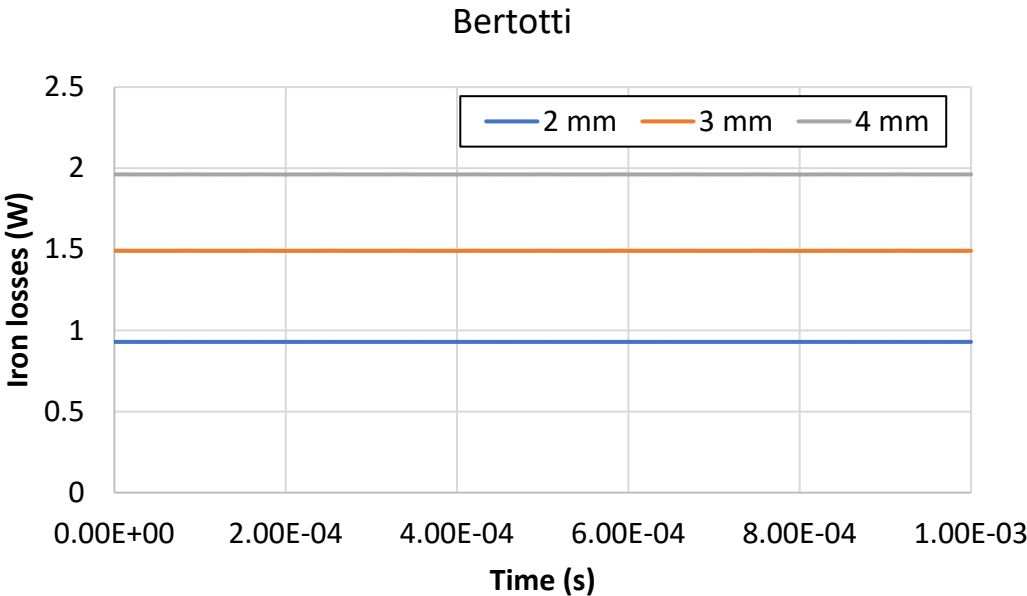
Figure 4.15: Iron losses using Bertotti for the three different permanent magnets thickness
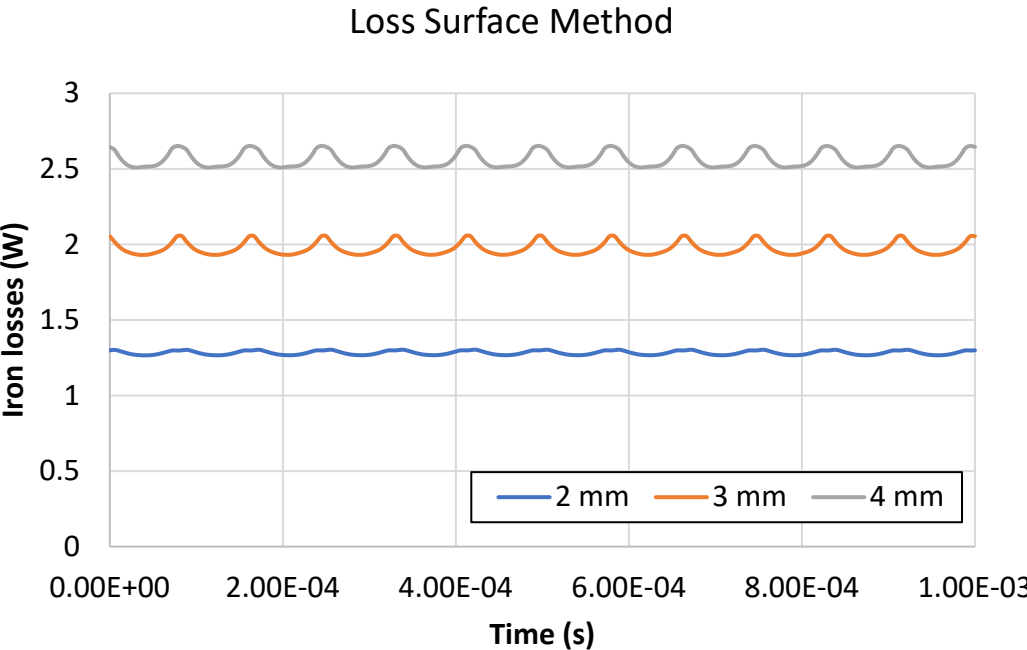
Figure 4.16: Iron losses using the Loss Surface Method for the three different permanent magnets thickness

The sleeve losses in no load conditions are 0.64mW, 1.03 mW and 1.37mW, respectively for a permanent magnets thickness equal to 2 mm, 3 mm and 4 mm. The results are reported in Figure 4.17.
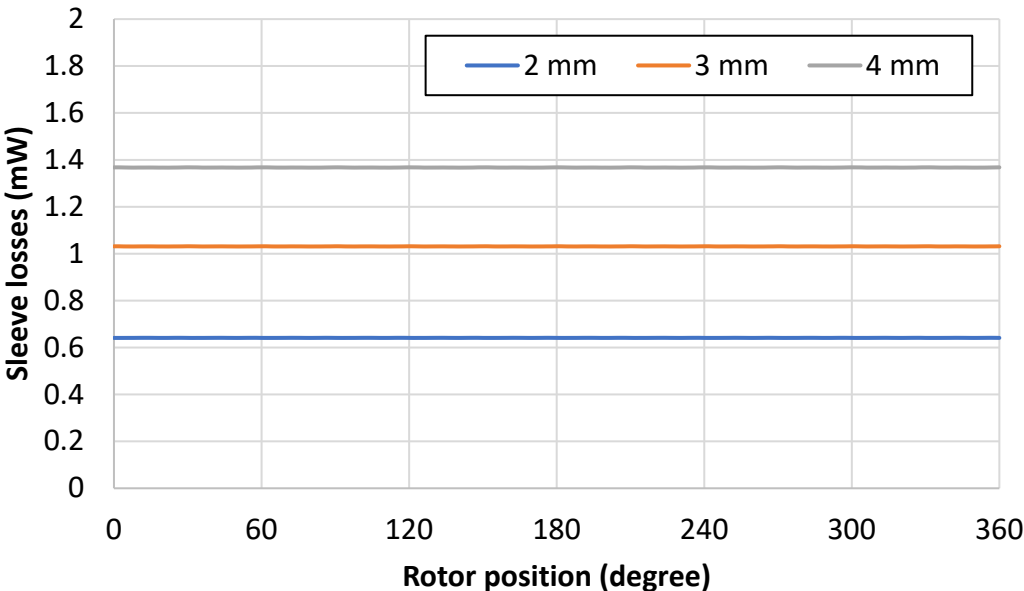
Figure 4.17: Sleeve losses for the three different permanent magnets thickness

The permanent magnet losses in no load conditions are 2.55mW, 3.9mW and 5.17mW respectively for a permanent magnets thickness of 2mm, 3mm and 4mm. The results are reported in Figure 4.18.
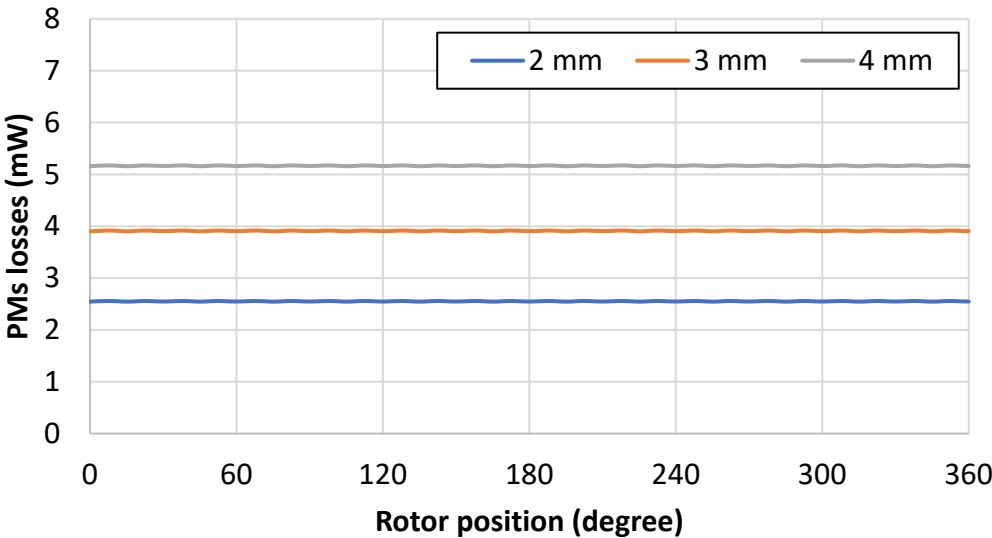
Figure 4.18: PMs losses for the three different permanent magnets thickness

4.2.2 Simulation in load conditions

The reference temperature is 90 degree.

- Torque

The average electromagnetic torques are 19mNm, 25mNm and 28mNm, respectively for a permanent magnets thickness equal 2 mm, 3 mm and 4 mm. The results are reported in Figure 4.19 while the FFT of the torque are reported in Figure 4.20, where it is possible to see that the torque ripple is very small.
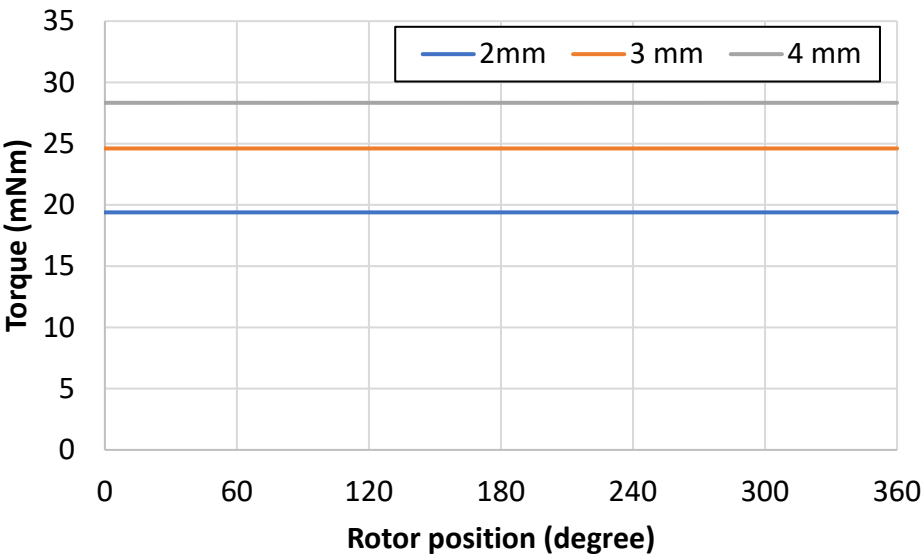
Figure 4.19: Torque for the three different permanent magnets thickness
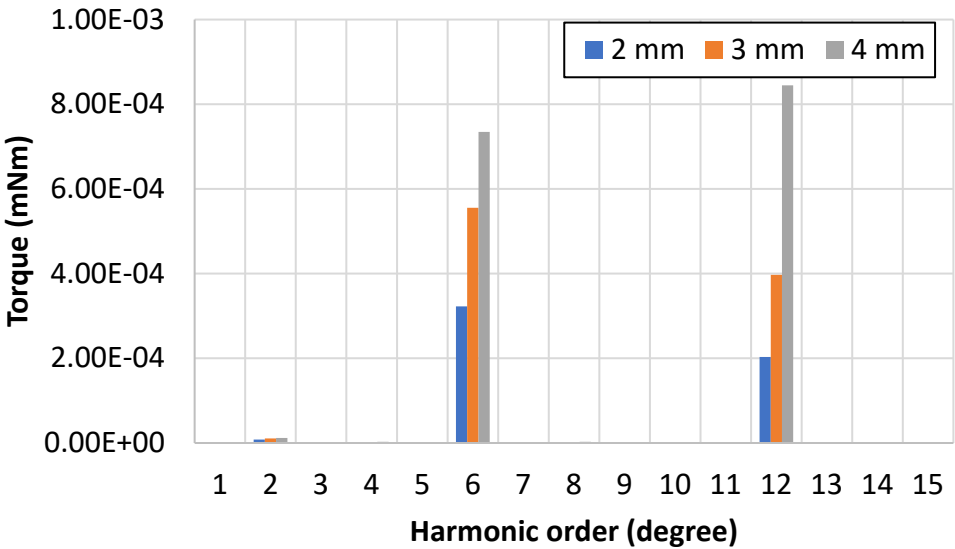
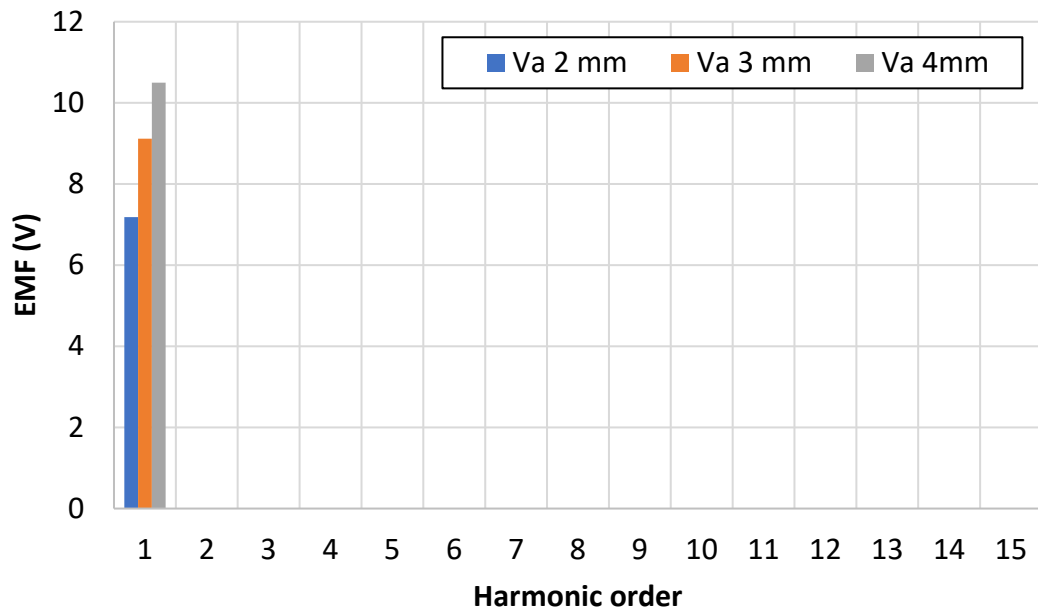*Figure 4.20: FFT of the torque for the three different permanent magnets thickness*

The iron losses have been evaluated with Bertotti and Loss Surface Method. The iron losses using Bertotti are 1.02 W, 1.24 W and 1.49 W respectively for a thickness of the permanent magnets of 2 mm, 3 mm and 4 mm. The results are reported in figure 4.21. The iron losses using the Loss Surface Method are 1.39 W, 1.67 W and 1.97 W respectively for a thickness of the permanent magnets of 2 mm, 3 mm and 4 mm. The results are reported in figure 4.22. Considering the iron losses computed using the Loss Surface Method, which is considered more accurate than Bertotti, the iron losses in no-load conditions are higher than the one in load conditions. The reason of this phenomenon is to be found in the magnetic flux density, that is higher in no load conditions, as it is possible to see in Figure 4.23 and 4.24.
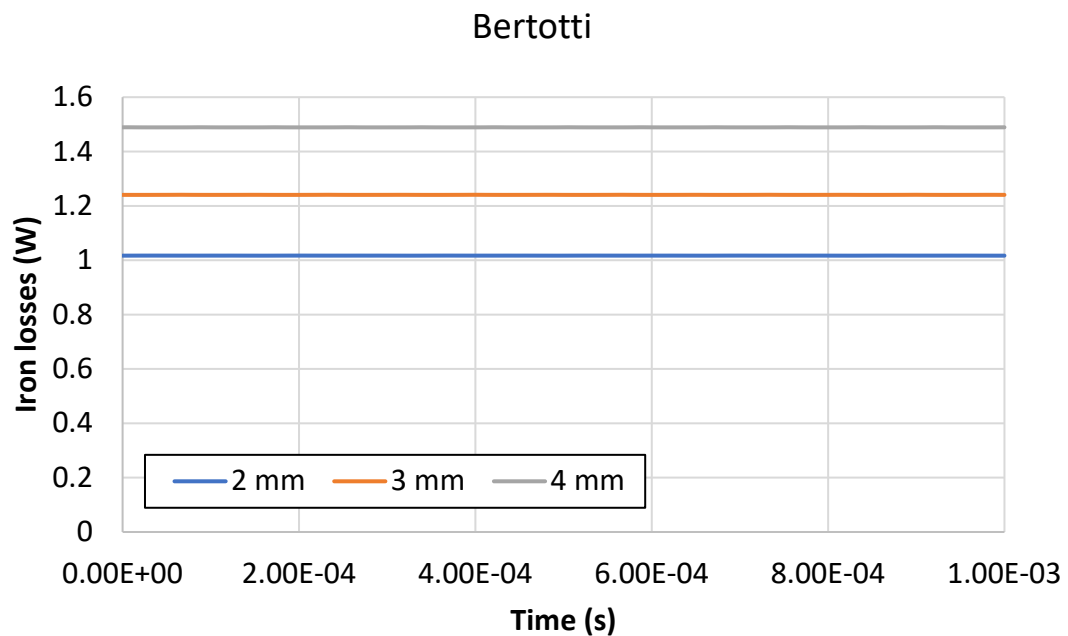
Figure 4.21: Iron losses in load conditions using Bertotti for the three different permanent magnets thickness

91
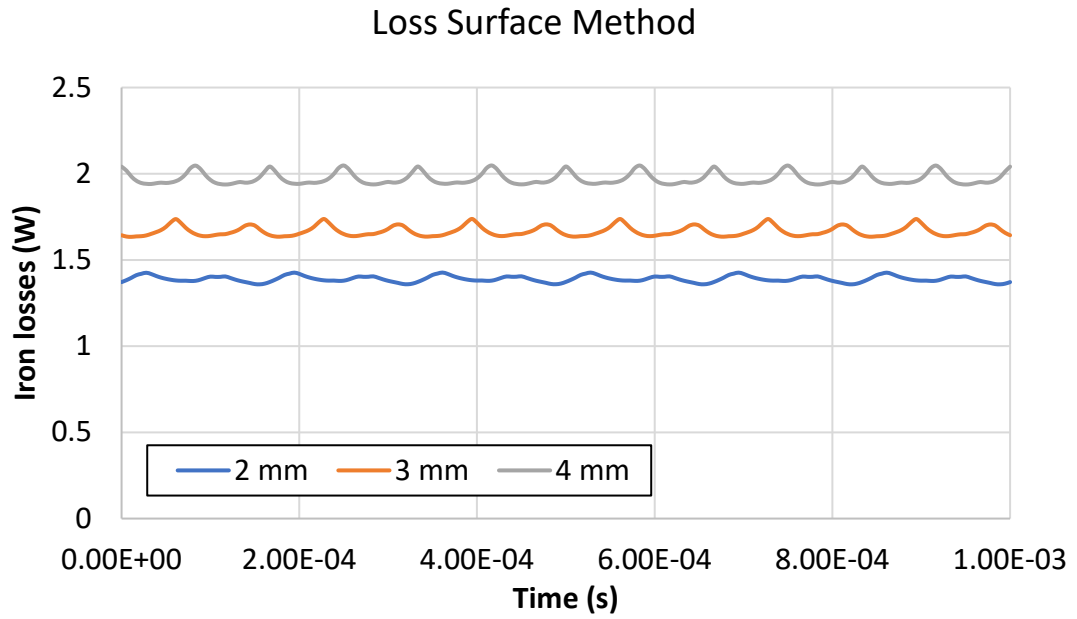
Figure 4.22: Iron losses in load conditions using the Loss Surface Method for the three different permanent magnets thickness
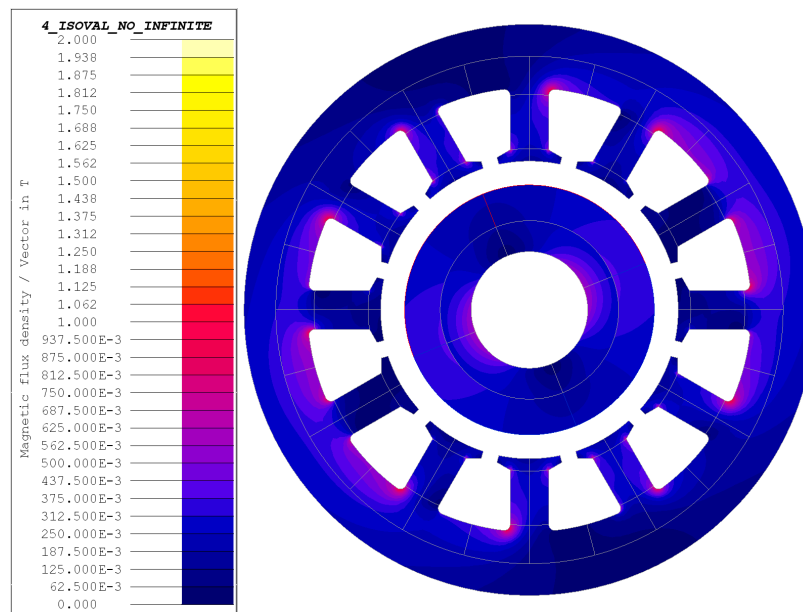
Figure 4.23: Magnetic flux density in no-load conditions with a PMs thickness of 3 mm
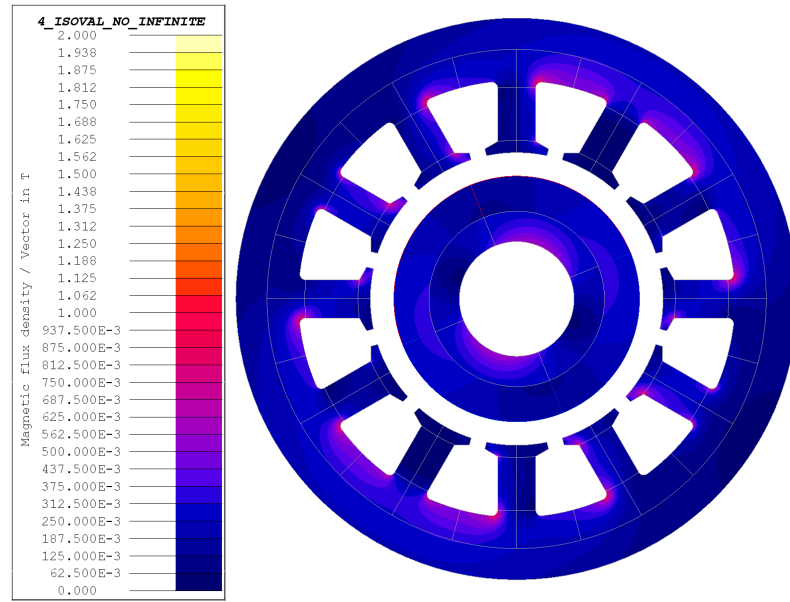
Figure 4.24: Magnetic flux density in load conditions with a PMs thickness of 3 mm

The sleeve losses in load conditions are 11.3 W, 11.22 W and 11.2 W, respectively for a permanent magnets thickness equal to 2 mm, 3 mm and 4 mm. The results are reported in Figure 4.25.
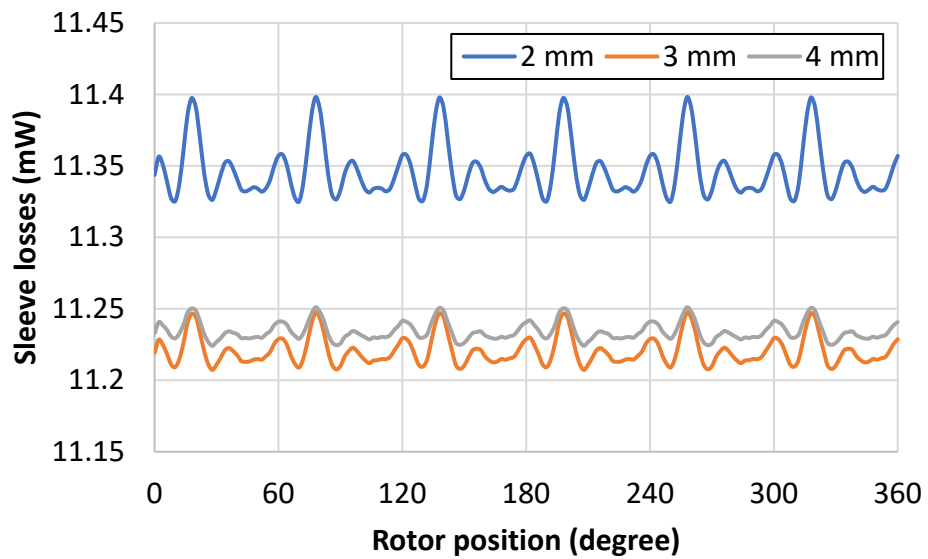
Figure 4.25: Sleeve losses in load conditions for the three different permanent magnets thickness

The permanent magnet losses in load conditions are 60 mW, 55 mW and 54 mW respectively for a permanent magnets thickness of 2mm, 3mm and 4mm. The results are reported in Figure 4.26.
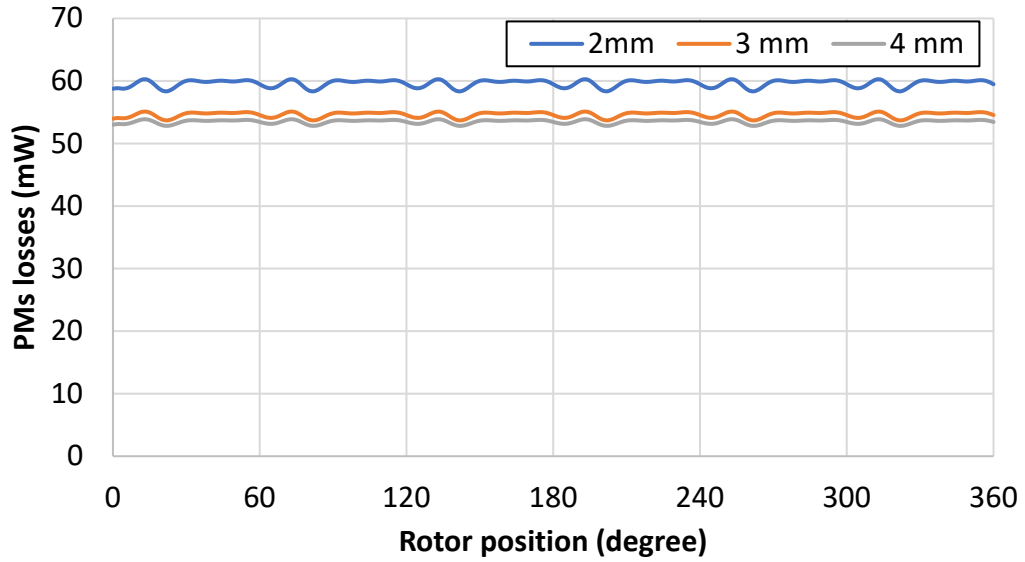
Figure 4.26: Permanent magnets losses in load conditions for the three different permanent magnets thickness

The results of the losses in no-load and load conditions for the different thickness of the PMs, are reported respectively in Table 4.3 and Table 4.4 to compare and do some evaluations.

Table 4.3: Losses in no-load conditions for the different thickness of the PMs

PMs thickness (mm)	Iron losses (W) (LSM)	Pms losses (mW)	Sleeve losses (mW)
2	1.28	2.55	0.64
3	1.97	3.9	1.03
4	2.56	5.17	1.37

Table 4.4: Losses in load conditions for the different thickness of the PMs

PMs thickness (mm)	Iron losses (W) (LSM)	Pms losses (mW)	Sleeve losses (mW)
2	1.39	60	11.3
3	1.67	55	11.22
4	1.97	54	11.2

The copper losses are:

$$P = 3 \cdot R \cdot I^2 = 6.5 \, W \tag{4.2}$$

From the results obtained with the three different configurations, it is possible to deduce that the optimal configuration is the one with a permanent magnets thickness of 3 mm, with an EMF of 9.12 V and a torque of 25 mNm.

4.2.3 Inductance computation

I. *Magnetization inductance*

The given parameters are the number or phase *m*, the pole pair *p*, the thickness of the effective airgap δ_0 met by the current linkage (obtained by the sum of the thickness of the airgap, of the sleeve and of the permanent magnets), the equivalent length *Lp* obtained by multiplying the active length for the stacking factor 0.97, the winding pitch τ_w, the fundamental winding factor $k_{w,1}$, the number of turns and assuming the Carter factor equal to 1. The effective airgap is different for the three configurations, because the radial thickness of the permanent magnets is different. δ_{01} is the equivalent airgap considering a magnet thickness of 2 mm, δ_{01}, δ_{02}, δ_{03} are the equivalent airgap considering respectively a permanent magnets thickness of 2, 3 and 4 mm. *Da* is the distance between the middle of a slot, to the middle of the diametral one.

$m = 3$

$p = 1$

$\delta_{01} = 0.004\ m$

$\delta_{02} = 0.005\ m$

$\delta_{03} = 0.006\ m$

$L_p = 0.018 * 0.97$

$k_{w,1} = 0.933$

$N_s = 20$

$K_{Carter} = 1$

First of all, the winding pitch must be computed:

$$\tau_w = \frac{\pi \cdot D_a}{2 \cdot p} \cdot \frac{5}{6} = 0.043m \tag{4.3}$$

There is a coefficient to take into account of the reduced pitch of one slot. From the equation (4.3) it is possible to compute the magnetization inductance, that is different for the three configurations:

$$L_m = \frac{m}{2} \cdot \frac{2}{\pi} \cdot \mu_0 \cdot \frac{1}{2 \cdot p} \cdot \frac{4}{\pi} \cdot \frac{\tau_w}{\delta_0} \cdot L_p \cdot \left(k_{w,1} \cdot N_s\right)^2 \tag{4.4}$$

From the equation (4.4) it follows:

$L_{m1} = 5 \cdot 10^{-5}\ H$

$L_{m2} = 4 \cdot 10^{-5}\ H$

$L_{m3} = 3.33 \cdot 10^{-5}\ H$

II. Leakage slot inductance

Considering the trapezoidal slot in Figure 2.36, the geometric parameters of the slot for the leakage slot inductance computation are:

$h_1 = 0.6 \cdot 10^{-3}\ m$

$h_2 = 0.33 \cdot 10^{-3}\ m$

$$h_3 = 0 \ m$$

$$h_4 = 5.239 \cdot 10^{-3} \ m$$

$$b_1 = 1.36 \cdot 10^{-3} \ m$$

$$b_4 = 3.823 \cdot 10^{-3} \ m$$

The permeance factor is given from the following equation:

$$\lambda_u = \frac{h_4}{3 \cdot b_4} + \frac{h_3}{b_4} + \frac{h_1}{b_1} + \frac{h_2}{b_4 - b_1} \cdot \ln\frac{b_4}{b_1} = 1.0365 \tag{4.5}$$

The leakage inductance is the following:

$$L_u = \mu_0 \cdot l' \cdot \frac{Q}{m} \cdot \left(\frac{z_q}{a}\right)^2 \cdot \lambda_u = 3.64 \cdot 10^{-5} \text{H} \tag{4.6}$$

III. Leakage end-winding inductance

Considering the Figure 2.37, it is possible to compute the end-winding inductance.

$$l_{ew} = 0.0215 \ m$$

$$W_{ew} = 0.043 \ m$$

$$\lambda_{lew} = 0.324$$

$$\lambda_{wew} = 0.0215$$

Where λ_{lew} and λ_{wew} are the permeance factor of the end winding, the values are tabulated for different combination of stator and rotor.

$$l_{end-winding} = 2 \cdot l_{ew} + W_{ew} \tag{4.7}$$

$$l_w \cdot \lambda_w = 2 \cdot l_{ew} \cdot \lambda_{lew} + W_{ew} \cdot \lambda_{wew} = 0.015 \tag{4.8}$$

$$L_w = \frac{Q}{m} \cdot q \cdot \left(\frac{z_q}{a}\right)^2 \cdot \mu_0 \cdot l_w \cdot \lambda_w = 6 \cdot 10^{-5} \text{ H} \tag{4.9}$$

4.2.4 Computation of the inductances by FEM

To compute the inductances by FEM, two different simulation have been performed. It is not necessary to use two different simulations, because the motor is isotropic, but in this way, it is checked that $L_d = L_q = L_m$. The B_r of the magnets is se equal to 0. In a simulation the current is supplied in the d axis, in the other one in the q axis. The current is controlled via scenario, changing the value from 0 A to 7.35 A, with a step value of 0.5 A. For each value of current it is computed the fundamental magnetic flux density in the airgap.

The inductances in d and q axis for each current are computed by the following equation:

$$L_m = K_w \cdot N_s \cdot \frac{2}{\pi} \cdot \tau \cdot L \cdot \frac{B_{foundamental}}{i_q} \tag{4.10}$$

The fundamental of the magnetic flux density is computed in FLUX.

Table 4.5: Values of the different magnetic flux density in the airgap for different stator current for a permanent magnets thickness of 2 mm

I	B_d	B_q	L_d	L_q
0	0	0	0	0
0.5	6.56E-03	6.56E-03	9.45E-05	9.45E-05
1	1.31E-02	1.31E-02	9.45E-05	9.45E-05
1.5	1.97E-02	1.97E-02	9.45E-05	9.45E-05
2	2.63E-02	2.63E-02	9.45E-05	9.45E-05
2.5	3.28E-02	3.28E-02	9.45E-05	9.45E-05
3	3.94E-02	3.94E-02	9.45E-05	9.45E-05
3.5	4.60E-02	4.60E-02	9.45E-05	9.45E-05
4	5.26E-02	5.26E-02	9.46E-05	9.46E-05
4.5	5.92E-02	5.92E-02	9.46E-05	9.46E-05
5	6.58E-02	6.58E-02	9.46E-05	9.46E-05
5.5	7.24E-02	7.24E-02	9.47E-05	9.47E-05
6	7.90E-02	7.90E-02	9.47E-05	9.47E-05
6.5	8.56E-02	8.56E-02	9.47E-05	9.47E-05
7	9.22E-02	9.22E-02	9.47E-05	9.47E-05

Table 4.6: Values of the different magnetic flux density in the airgap for different stator current for a permanent magnets thickness of 3 mm

I	B_d	B_q	L_d	L_q
0	0	0	0	0
0.5	5.37E-03	5.37E-03	7.32E-05	7.32E-05
1	1.07E-02	1.07E-02	7.32E-05	7.32E-05
1.5	1.61E-02	1.61E-02	7.32E-05	7.32E-05
2	2.15E-02	2.15E-02	7.32E-05	7.32E-05
2.5	2.69E-02	2.69E-02	7.32E-05	7.32E-05
3	3.22E-02	3.22E-02	7.32E-05	7.32E-05
3.5	3.76E-02	3.76E-02	7.33E-05	7.33E-05
4	4.30E-02	4.30E-02	7.33E-05	7.33E-05
4.5	4.83E-02	4.83E-02	7.33E-05	7.33E-05
5	5.38E-02	5.38E-02	7.33E-05	7.33E-05
5.5	5.92E-02	5.92E-02	7.33E-05	7.33E-05
6	6.46E-02	6.46E-02	7.33E-05	7.33E-05
6.5	7.00E-02	7.00E-02	7.34E-05	7.34E-05
7	7.55E-02	7.55E-02	0.000132	0.000132

Table 4.7: Values of the different magnetic flux density in the airgap for different stator current for a permanent magnets thickness of 4 mm

I	B_d	B_q	L_d	L_q
0	0	0	0	0
0.5	4.52E-03	4.52E-03	5.94E-05	5.94E-05
1	9.04E-03	9.04E-03	5.94E-05	5.94E-05
1.5	1.36 E-02	1.36 E-02	5.94E-05	5.94E-05
2	1.8E-02	1.8E-02	5.94E-05	5.94E-05
2.5	2.26E-02	2.26E-02	5.94E-05	5.94E-05
3	2.71E-02	2.71E-02	5.95E-05	5.95E-05
3.5	3.17E-02	3.17E-02	5.95E-05	5.95E-05
4	3.62E-02	3.62E-02	5.95E-05	5.95E-05

4.5	4.07E-02	4.07E-02	5.95E-05	5.95E-05
5	4.53 E-02	4.53 E-02	5.95E-05	5.95E-05
5.5	4.98 E-02	4.98 E-02	5.95E-05	5.95E-05
6	5.44 E-02	5.44 E-02	5.95E-05	5.95E-05
6.5	5.89 E-02	5.89 E-02	5.95E-05	5.95E-05
7	6.35E-02	6.35E-02	5.95E-05	5.95E-05

Making the average of the different inductance values obtained for each current, it is obtained the value of the magnetization inductance. The results for the three different configurations are:

$$L_{m1} = 9.46\text{E} - 05 \text{ H}$$

$$L_{m2} = 7.33\text{E} - 05 \text{ H}$$

$$L_{m3} = 5.95\text{E} - 05 \text{ H}$$

Finally, the L_s is computed as follows:

$$L_{s1} = L_{m1} + L_{leakage} = 1.91\ E - 04\ H \tag{4.11}$$

$$L_{s2} = L_{m2} + L_{leakage} = 1.7\ E - 04\ H \tag{4.12}$$

$$L_{s3} = L_{m3} + L_{leakage} = 1.56\ E - 04\ H \tag{4.13}$$

4.3 Slotless motor

The goal in this section is to analyze a slotless motor starting from the Agilent motor of the Chapter 2, using the same material, winding layout and parameters. In the slotless motor the winding are fixed with a resin that gives them rigidity. They are placed in the airgap, between the stator and the rotor, without iron teeth; therefore, the first advantage is the absence of the cogging torque and consequently the lowering of the noise. Another advance is the lower inductance, due to the absence of the slot leakage. The losses of a slotless motor are very low, consequently, the slotless motor has a higher efficiency.

The slotless motor has also some disadvantages, the airgap is higher than a slotted motor, it is due to the presence of the winding in this area. Consequently, the flux density and the torque are lower. To get around this problem, it is possible to realize larger permanent magnets, but this leads to an increase in cost. Also, the litz wires used in this motor are more expensive than the windings used in the slotted machine.
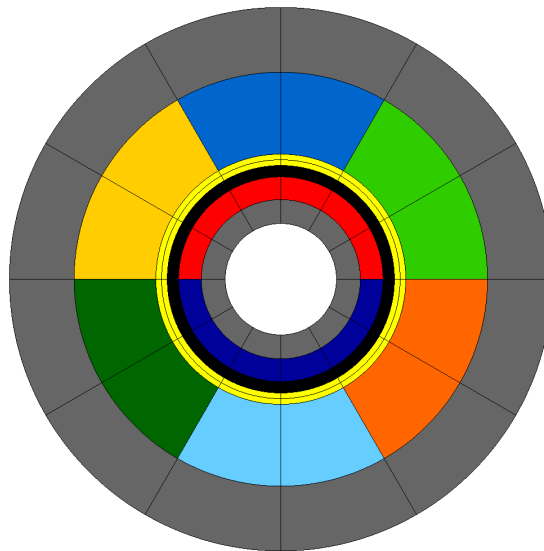

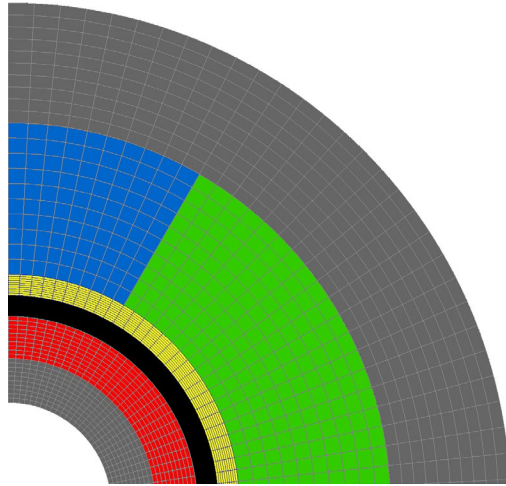*Figure 4.27: Slotless motor section*

Figure 4.28: Mapped mesh of the slotless motor

4.3.1 Simulation in no-load conditions

- EMF

The EMF in the slotless motor has a peak value of 9.114 V (Figure 4.29 and Figure 4.30), while the slotted motor EMF was of 21 V. The cogging torque is 0, indeed it is due to the interaction between the permanent magnets of the rotor and the stator slots (Figure 4.31).
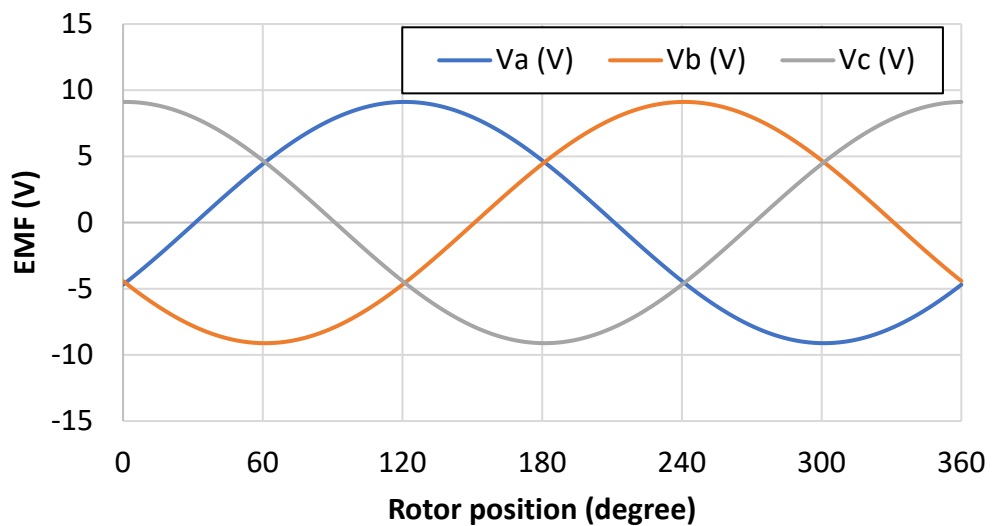

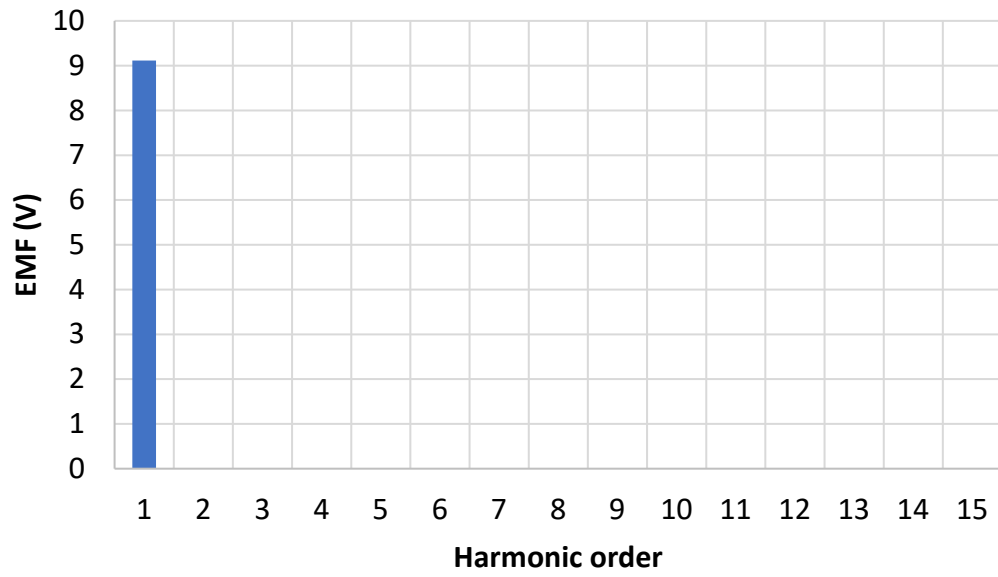*Figure 4.29: EMF of the slotless motor in no-load conditions*

Figure 4.30: FFT of the EMF of the slotless motor in no-load conditions
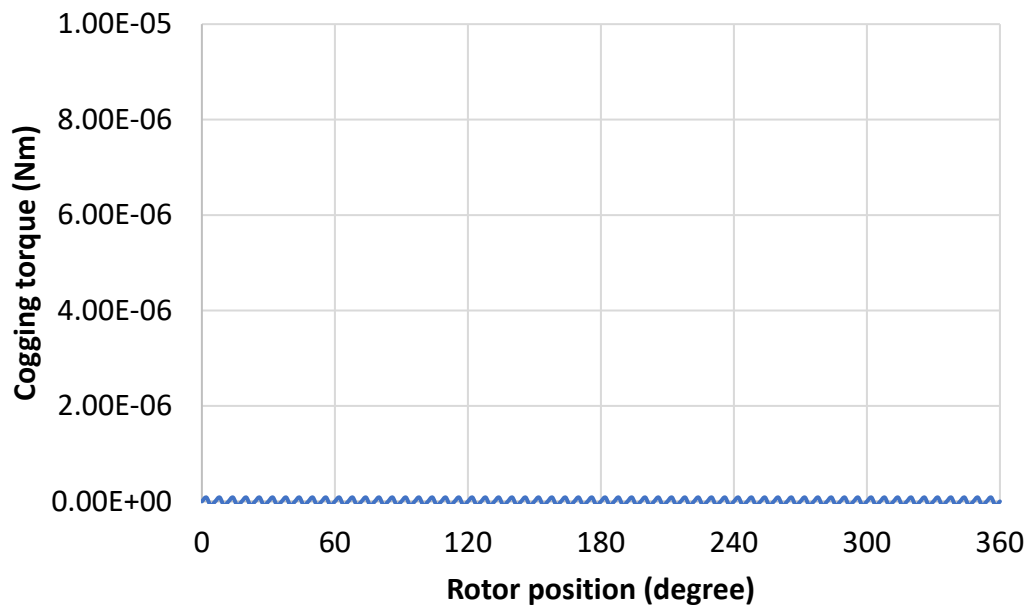

Figure 4.31: Cogging torque of the slotless motor

- Losses

The iron losses have been evaluated with Loss Surface Method. The average value of the iron losses is 0.89 W (Figure 4.32).
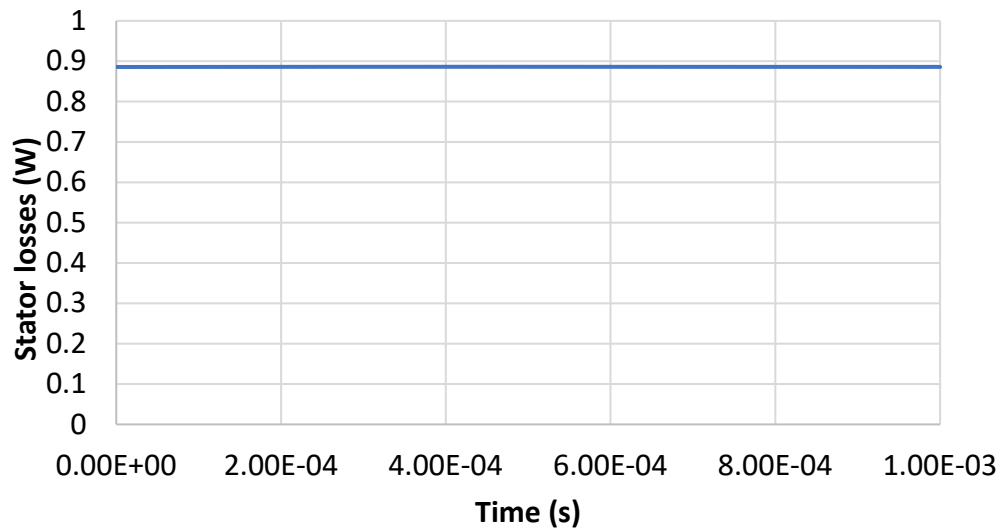
Figure 4.32: Iron losses of the slotless motor using Loss Surface Method

4.3.2 Simulation in load conditions

After checking that the phase voltage and the phase current are in phase, the torque is computed. The simulation in load conditions is always at 90°C, using the same current of the Agilent motor, 5.2 A_{rms}. The average torque is 15mNm, with a small ripple; the results of the simulation are reported in Figure 4.33 and 4.34.

Figure 4.33: Torque of the slotless motor considering 5.2A$_{rms}$

Figure 4.34: FFT of the torque of the slotless motor considering 5.2A$_{rms}$

4.3.3 New current value

The area of the regions were the conductors are inserted are bigger than the slot area, consequently, the resistance of the slotless motor is lower than the resistance of the slotted motor. The new resistance is:
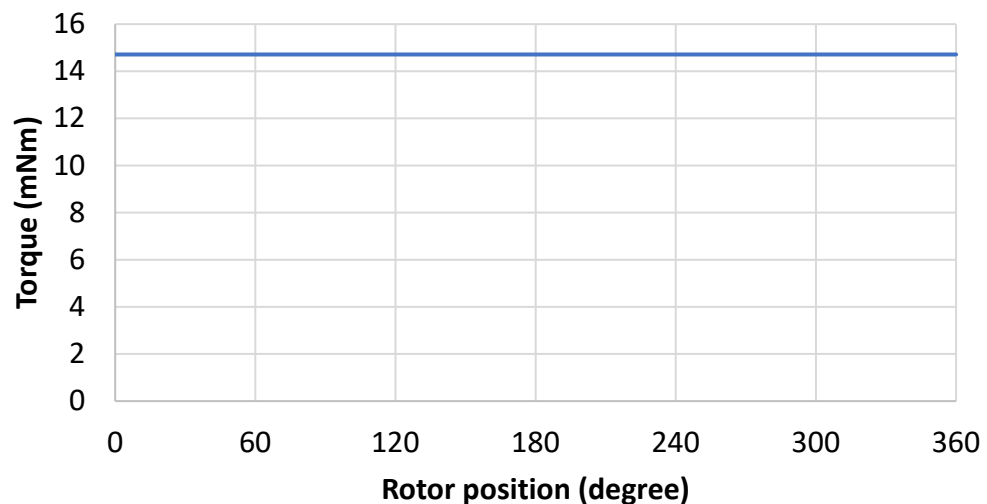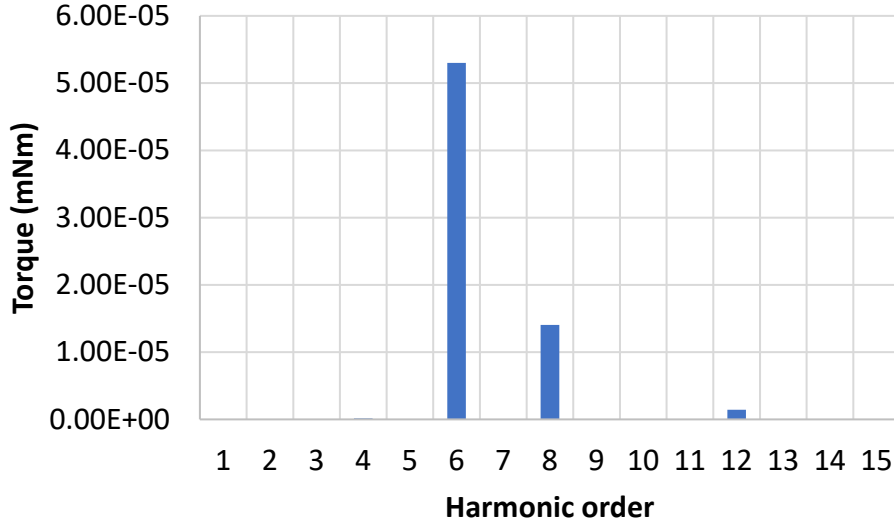
$$R = R_0 \cdot (1 + \alpha \cdot (T - T_0)) \cdot \frac{Aslot_{old}}{Asector} = 0.114 \ \Omega \qquad (4.14)$$

Where R_0 is the resistance of the slotted motor at 20°C, α is the copper temperature equal to 0.00393, A_{slot} is the area of the slot of the slotted motor and A_{sector} is the area of the region where there are the conductors in the slotless motor.

The resistance of the slotted machine at 90°C was of 0.17 Ω and the Joule losses where 14W, supplying the stator with a current of 5.2 A$_{rms}$. In the soltless machine, for the same amount of Joule losses, it is possible to feed the stator windings with higher currents, having a lower phase resistance. The new current value is:

$$I = \sqrt{\frac{P}{3 \cdot R}} = 6.4 \ Arms \qquad (4.15)$$

The current is easily computed by the Joule losses equation:

105

$$P = 3 \cdot R \cdot I^2 \hspace{4cm} (4.16)$$

For slotless PM machine, there are two resultant field to consider in the proximity effect loss calculation, one is caused by armature, and one is caused by permanent magnets. The total field changes with time, and it assumes importance for high speed machine because of the high frequency. It is possible to consider the simplified equation for Joule losses (Equation 4.16), assuming to use Litz wires. The Litz wires are many strands in parallel, where each strand change position in the wire cross-section. With this assumption the proximity effect losses are negligible for the computation of the copper losses machine.

4.3.4 Simulation results with new current value

The new current value in FLUX is i_q equal to 9.051 A (as peak value). The new electromagnetic torque has an average value of 18 mNm, Figure 4.35 and Figure 4.36. The iron losses are 0.61 W using Bertotti method and 0.8 W using the Loss Surface Method (Figure 4.37 and 4.38). The sleeve losses are 0.02 mW and the permanent magnets losses are 0.213 mW (Figure 4.39 and 4.40).

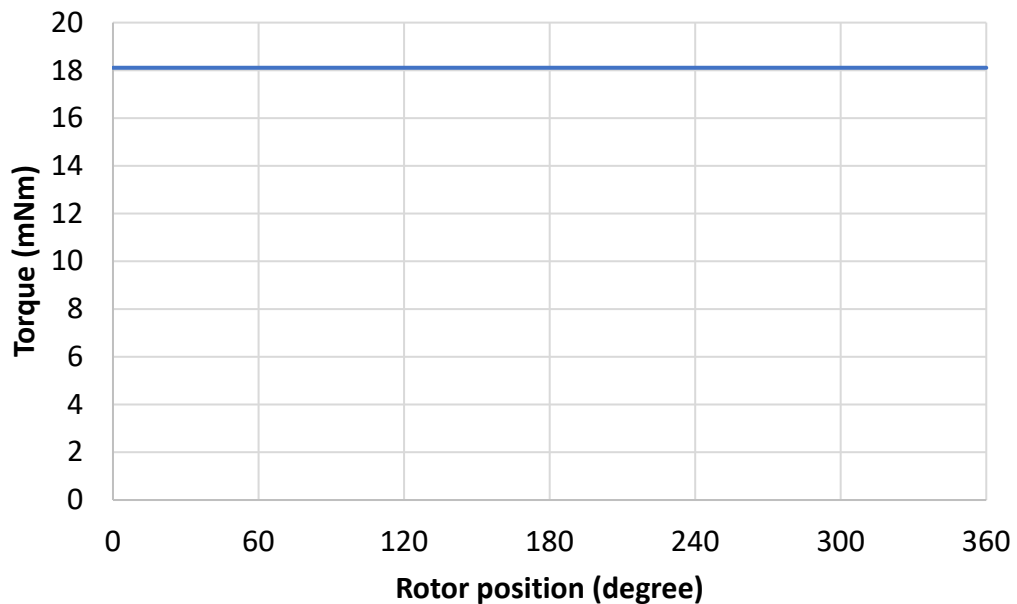Figure 4.35: Torque of the slotless motor with the new current value
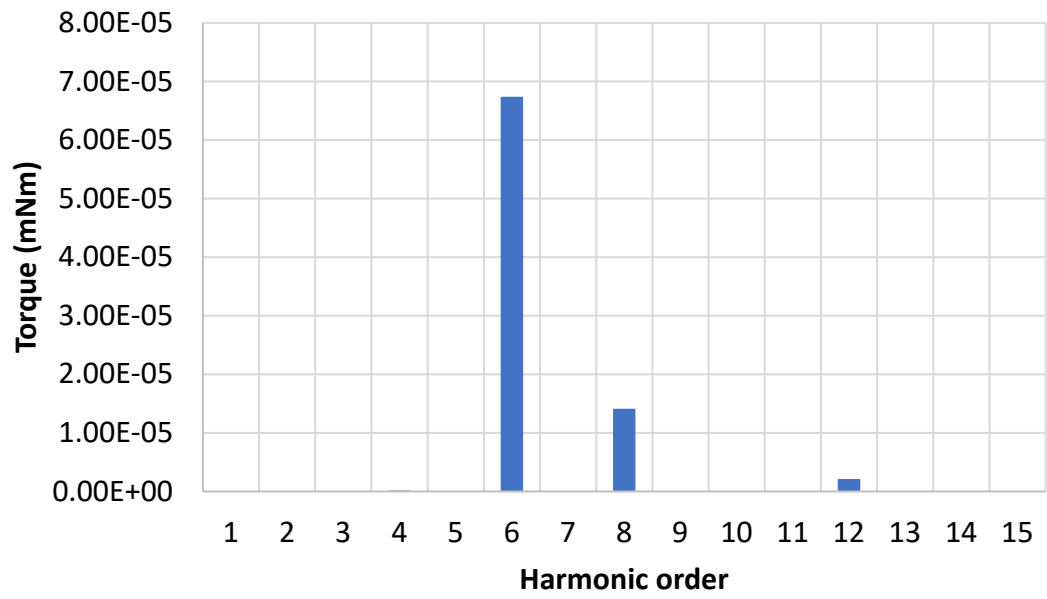
Figure 4.36: FFT of the torque of the slotless motor with the new current value
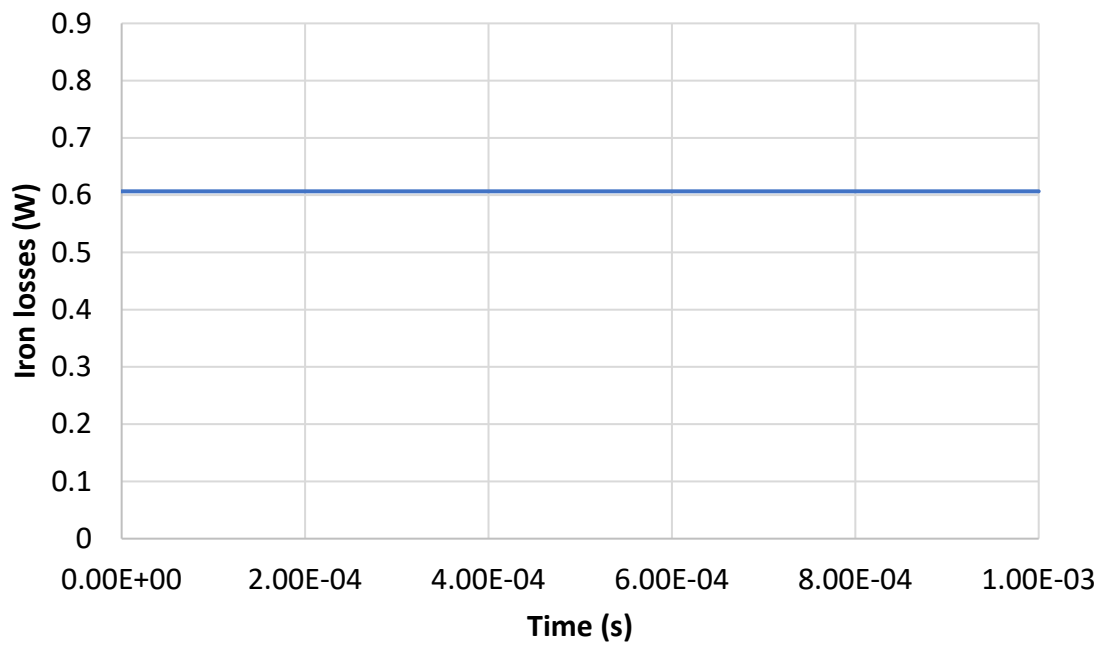
Figure 4.37: Iron losses using Bertotti for the slotless motor with the new current value
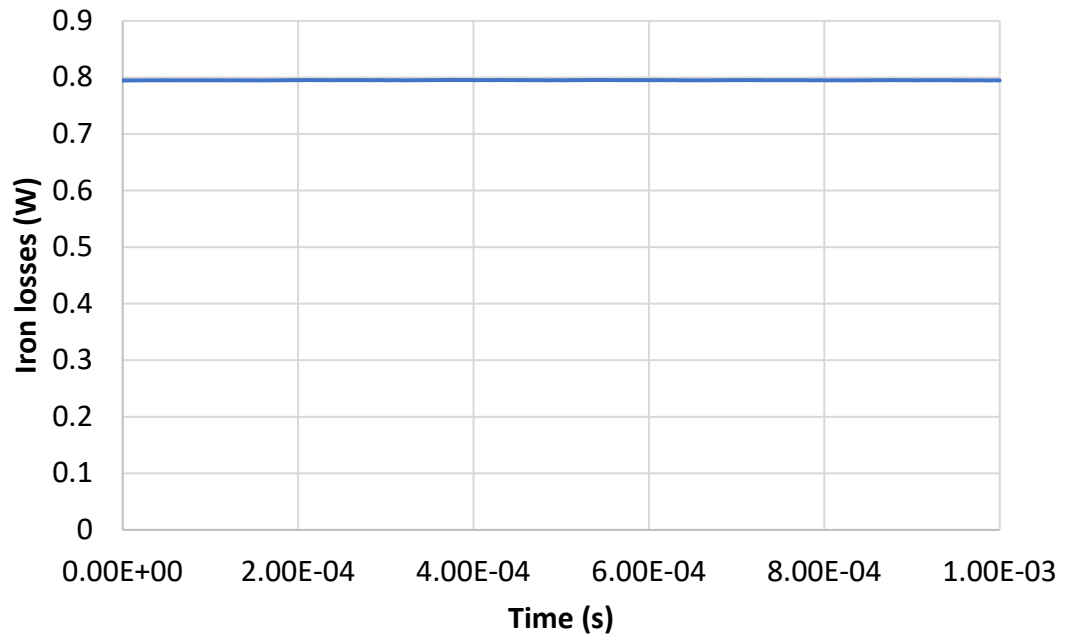
Figure 4.38: Iron losses using LS Method for the slotless motor with the new current value

Figure 4.39: Sleeve losses for the slotless motor with the new current value

Figure 4.40: Permanent magnets losses for the slotless motor with the new current value

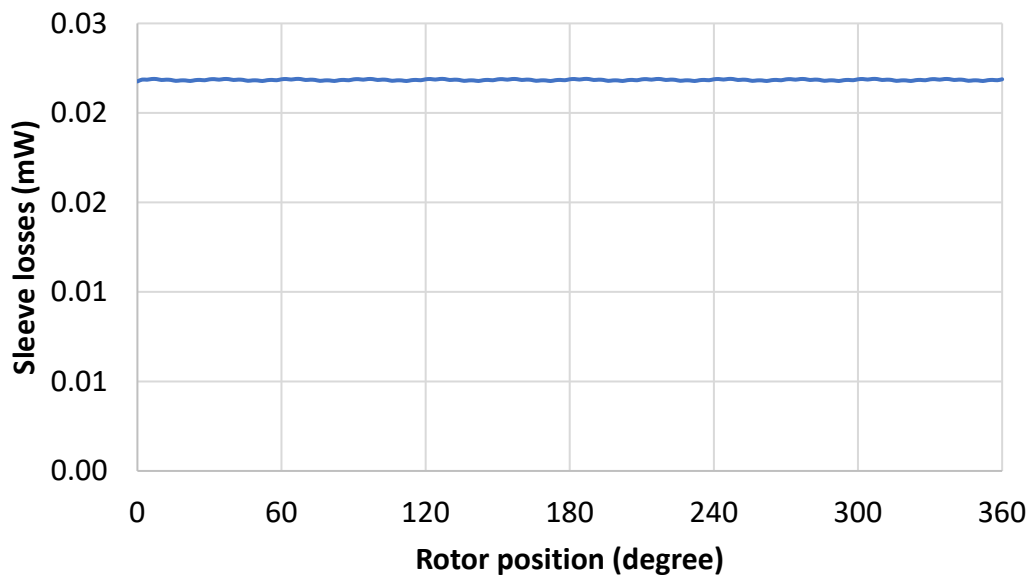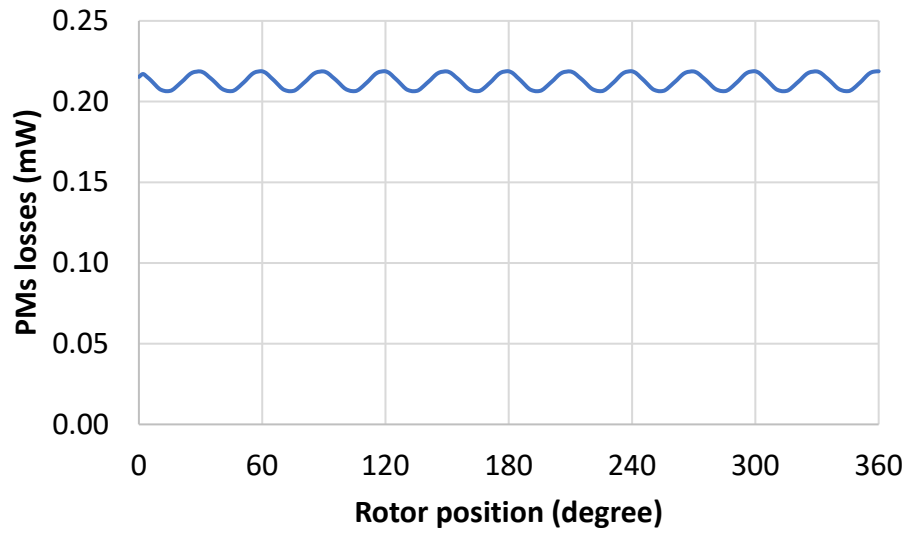The iron losses in load conditions are lower than the iron losses in no-load condition, but it is due to the lower magnetic flux density in load conditions (Figure 4.41 and 4.42).
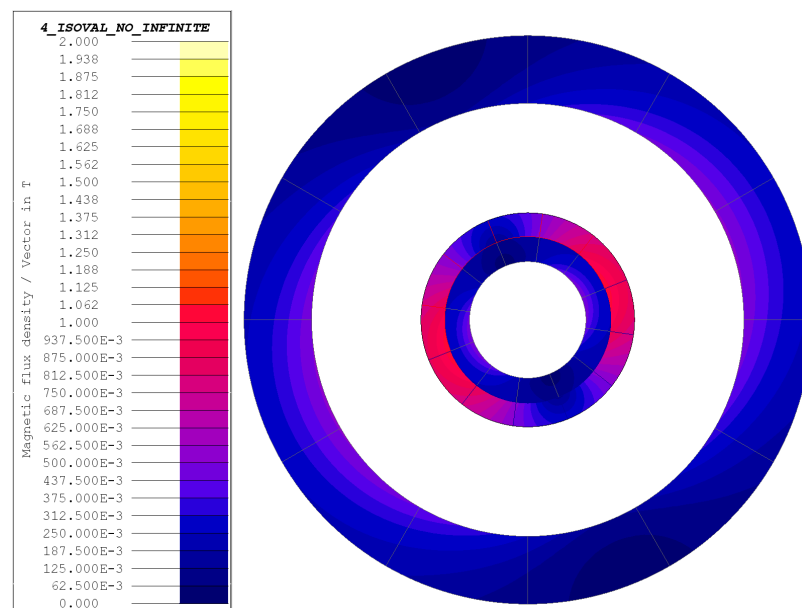
Figure 4.41: Magnetic flux density in no-load conditions in the slotless motor
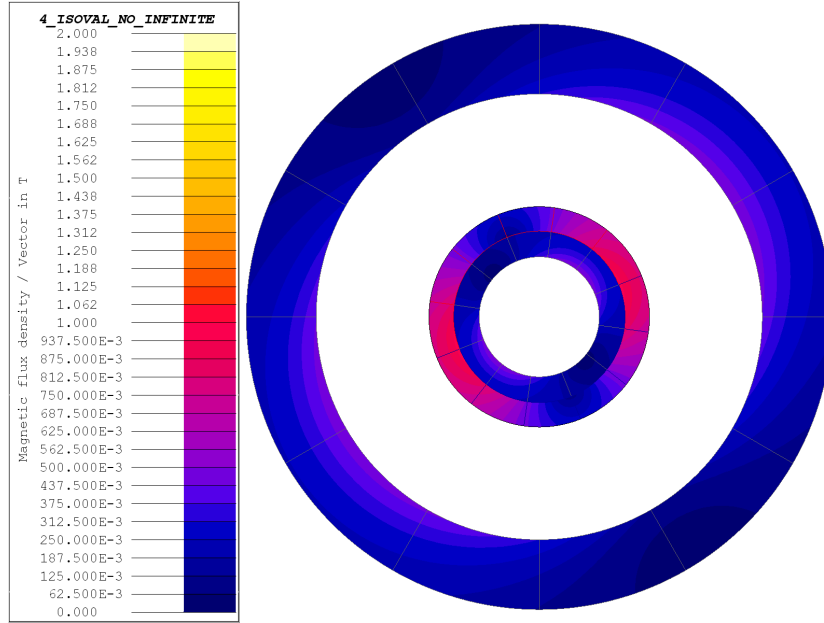
Figure 4.42: Magnetic flux density in load conditions in the slotless motor

4.3.5 Inductance computation

In the slotless motor the magnetization inductance will be lower than the one in the slotted motor, because there is no slot-leakage inductance.

The end-winding leakage inductance is the same of the old motor, the computation is reported in chapter 2, and its value is $6.7 \cdot 10^{-5}$ H.

4.3.6 Computation of the inductance by FEM

To compute the inductances by FEM, two different simulation have been performed. It is not necessary to use two different simulations, because the motor is isotropic, but in this way, it is checked that $L_d = L_q = L_m$.

The B_r of the magnets is setted equal to 0. In a simulation the current is supplied in the d axis, in the other one in the q axis. The current is controlled via scenario, changing the value from 0 A to 9.1 A, with a step value of 1 A. For each value of current it is computed the fundamental magnetic flux density in the airgap.

The inductances in d and q axis for each current are computed using the Equation 4.10, the fundamental magnetic flux density is reported in Table 4.8.

Table 4.8: Values of the different magnetic flux density in the airgap for different stator current for the slotless motor

I	B_d	B_q	L_d	L_q
0	0	0	0	0
1	3.56E-03	3.56E-03	3.54E-05	3.54E-05
2	7.12E-03	7.12E-03	3.54E-05	3.54E-05
3	1.07E-02	1.07E-02	3.54E-05	3.54E-05
4	1.42E-02	1.42E-02	3.54E-05	3.54E-05
5	1.78E-02	1.78E-02	3.54E-05	3.54E-05
6	2.14E-02	2.14E-02	3.54E-05	3.54E-05
7	2.49E-02	2.49E-02	3.54E-05	3.54E-05
8	2.85E-02	2.85E-02	3.54E-05	3.54E-05
9.1	3.24E-02	3.24E-02	3.54E-05	3.54E-05

Making the average of the different inductance values obtained for each current, the value of the magnetization inductance is:

$$L_m = 3.54 \cdot 10^{-5} + 6.7 \cdot 10^{-5} = 10^{-4} H$$

It is reported a summary table, to compare the main computed quantities for the slotted and slotless motor, to do some considerations.

Table 4.9: Comparative table of the main computed quantities for the slotted and slottless motor in load conditions

Quantities	Slotless $(i_q=6.4A_{rms})$	Slotted $(i_q=5.2A_{rms})$
EMF (V)	9.114	21
Torque (mNm)	18	34
Iron losses (W)	0.8	6.41
Sleeve losses (mW)	0.218	6.9
PMs losses (mW)	0.213	18.8
Magnetization inductance (H)	10^{-4}	$1.5 \cdot 10^{-4}$

From the summary table, it follows that the slotless motor is a good solution because the losses are really low compared to the ones of the slotted motor.

Chapter 5

Conclusions and Future Work

5.1 Conclusions

In this thesis are investigated different design solutions of a brushless motor for high speed applications starting from a given machine.

The first proposed solution adopts a stator from an existing induction motor, for economic advantages and cheaper magnets in ferrite. To obtain comparable performances with the existing SPM motor, different magnet thicknesses have been investigated. This motor has lower performances than the existing one: the average torque is lower and the losses in the sleeve and in the permanent magnets are higher.

The second solution is a slotless machine, starting from the existing Agilent motor. This solution may provide some advantages in high speed machine, thanks to the absence of cogging torque and to the low losses. The comparative analysis between the slotted and the slotless machine, accomplished by analytical and 2D FEM simulations, shows that the slotless motor is a good alternative. In the slotless motor the winding must be properly designed to limit the proximity losses in the copper which in this case have been assumed negligible. The losses resulted lower compared to those of the original machine. The average torque of the slotless motor (18 mNm) is smaller than the one of the slotted machine (34 mNm), but not so far from the required target (20-22mNm). Moreover, a bigger average torque can be found with further improvements; for istance it is possible to choose a higher current if it is acceptable from the thermal point of view or, in alternative, it is possible to redesign the slotless motor using different length and diameters.

5.2 Future work

In Chapter 3 it is highlighted the difference between the iron losses computed using sinusoidal supply and PWM supply.

The computation of the iron losses using a PWM supply will be approached and solved in future. It is possible also to do a comparative analysis between the iron losses obtained using PWM and PAM supply.

Biobliography

[1] D. Gerada, A. Mebarki, N. L. Brown, C. Gerada, A. Cavagnino and A. Boglietti, *High speed electrical machines: Technologies, Trends, and Developments,* in IEEE Transactions of Industrial Electronics, vol. 61, no. 6, pp. 2946-2952

[2] A. Boglietti, R. Bojoi, A. Cavagnino, P. Guglielmi and A. Miotto, *Analysis and Modeling of Rotor Slot Enclosure Effects in High Speed Induction Motors,* Politecnico di Torino, Dipartimento di Ingegneria Elettrica, Corso Duca degli Abruzzi 24, 10129 Torino, ITALY

[3] A. Borisavljevic, H. Polinder, J. A. Ferrera, *On the speed limits of permanent magnet machines,* in IEEE Transactions of Industrial Electronics, vol. 57, p 223

[4] Vaschetto et al., *Sizing Procedure of Surface Mounted PM Machines for Fast Analytical Evaluations*

[5] J. F. Gieras, B. C. Woo, D. H. Kang, *Selected Aspects of Design of High Speed Permanent Magnet Brushless Machines,*2018 21th International Conference on Electrical Machines and Systems (ICEMS) October 7-10,2018, Jeju, Korea

[6] A. Cavagnino, G. Pellegrino, S. Vaschetto, E. B. Agamloh, *Contribution to Offline Measurements of PMSM and SyRM Inductances*, in IEEE Transactions on Industry Applications, vol. 55, no. 1, January/February 2019

[7] A. Krings, S. Nategh, A. Stening, H. Grop, O. Wallmark, J. Soulard, *Measurament and Modeling of Iron Losses in Electrical Machines*, Laboratory of Electrical Energy Conversion (E2C), Royal Institute of Technology (KTH) Teknikringen 33, SE-100 44 Stockholm, Sweden, pp. 1-5

[8] Z. Gmyrek, A. Boglietti and A. Cavagnino, *Iron Loss Prediction With PWM Supply Using Low- and High Frequency Measurements: Analysis and Results Comparison*, in IEEE Transactions on Industrial Electronics, vol. 55, no. 4, April 2008 pp 1722-1728

[9] L. Schwager, a. Tuysuz, C. Zwyssig, J. W. Kolar, *Modeling and Comparison of Machine and Converter Losses for PWM and PAM in High-Speed Drives,* in IEEE Transactions on Industry Applications, vol. 50, no. 2, pp 995-1006, March/April 2014

[10] L. Li, A. Kedous-Lebouc, A. Foggia, J.C. Mipo, *An Iron Loss Model (Loss Surface) for FeCo Sheet and Its Application in Machine Design*, XIX International Conference on Electrical Machines, ICEM 2010, Rome, pp. 1-2

[11] H. Tahanian, M. Aliahmadi, J. Faiz, *Ferrite Permanent Magnets in Electrical Machines: Opportunities and Challenges of a Non-Rare-Earth Alternative*, in IEEE Transatcions of Magnetics, vol. 56, no. 3, 3 March 2020

[12] A. Shanshal, K. Hoang and Kais, *High-Performance Ferrite Permanent Magnet Brushless Machines,* in IEEE Transactions on Magnetics, vol. 55, no. 7, July 2019

[13] J. Shen, X. Qin, Y. Wang, *High-Speed Permanent Magnet Electrical Machines - Applications, Key Issues and Challenges*, CES Transactions of Electrical Machines and Systems, vol. 2, no. 1, March 2018

[14] A. Yu, G. W. Jewell, *Systematic design study into the influence of rotational speed on the torque density of surface-mounted permanent magnet machines*, The Journal of Engineering, The 9th International Conference on Power Electronics, Machines and Drives (PEMD 2018)

[15] B. Borisavljevi´c, *Limits, Modeling and Design of High-Speed Permanent Magnet Machines*

[16] J. Phirhonen, T. Jokinen, V. Hrabovcovà, *Design of Rotating Electrical Machines*, Second Edition, pp. 230-263